Several Aspects of Polycrystalline Ice Behavior Based On Micromechanical Modeling

by

Alex A. Elvin

BSc Eng., University of the Witwatersrand,
Johannesburg, South Africa, (1989)
S.M., Massachusetts Institute of Technology (1991)

Submitted to the Department of Civil and
Environmental Engineering
in partial fulfillment of the requirements for the degree of

Doctor of Philosophy

at the

MASSACHUSETTS INSTITUTE OF TECHNOLOGY

June 1996

Author .....
Department of Civil and
Environmental Engineering
February 8, 1996

Certified by .....
Jerome J. Connor
Professor of Civil and Environmental Engineering
Thesis Supervisor

Accepted by .....
Joseph Sussman
Chairman, Departmental Committee on Graduate Students

SEVERAL ASPECTS OF POLYCRYSTALLINE ICE BEHAVIOR BASED ON MICROMECHANICAL MODELING

by

Alex A. Elvin

Submitted to the Department of Civil & Environmental Engineering
on February 8, 1996, in partial fulfillment of the
requirements for the degree of Doctor of Philosophy

ABSTRACT

This thesis focuses on three aspects of polycrystalline ice behavior. In particular, the following questions are addressed: (1) What causes microcracking in polycrystalline ice loaded in compression at high strain rates? (2) How many grains are required to homogenize the elastic properties of ice?, and (3) Is there a thickness effect on the transverse shear modulus of ice plates?

Previously it was believed that the elastic mismatch between neighboring ice grains was the cause of microcracking in polycrystalline ice loaded in compression at high strain rates. However, analyses show that if only the elastic anisotropy mechanism operates, the stresses required for microcracking are unrealisticly high; also the longest possible microcracks are orders of magnitude shorter than observed experimentally. Much more realistic stresses, and facet length microcracks are possible if there is grain boundary deformation. Simulations of uniaxial and biaxial compression show that with grain boundary deformation, a defect originating at a triple point grows stably, reaches a critical length and then propagates unstably to the neighboring triple point.

The number of grains required to homogenize the elastic behavior of polycrystalline ice determines the representative area element. Two extreme cases of (i) no grain boundary slip and (ii) free grain boundary sliding are examined. Detailed finite element simulations of uniaxial loading of specimens containing polygonal grains are performed. The results show that at least 230 grains are required to homogenize the elastic properties. The average computed Young's modulus and Poisson ratio at $-16°C$ are: 9.58 GPa and 0.33- with no grain boundary sliding; 7.83 GPa and 0.45- with free grain boundary sliding.

If there is grain boundary deformation and grain coarsening with plate depth, the transverse shear modulus, G, increases with plate thickness. Simulations show that G can increase five times as the ice plate increases from 0.05 to 1.2 m. There are two important implications. First, the energy due to shear deformation, which has been largely ignored, has to be included when performing fracture analyses. Second, when calculating in-plane static Young's modulus E, both bending and shear deformations have to be considered. Based on bending theory alone, $E = 45\ MPa$ was calculated previously for thin model ice plates; a much higher $E = 3.2\ GPa$ is calculated if shear deformation is included.

Thesis Committee: Prof J. J. Connor (Chairman, Civ. & Env. Eng.)
Prof. L. Anand (Mech. Eng.)
Prof. K.J. Bathe (Mech. Eng.)
Prof. M. Kachanov (Tufts Univ.)
Prof. C.K. Leung (Civ. & Env. Eng.)
Dr. S. Shyam Sunder (NIST)

To My Father
To My Mother, and
To My Brother
For Their Support
and Encouragement

The scientist must put things in order; science is made of facts as a house is made of stones, but science is no more an accumulation of facts than a house is a pile of stones.

H. Poincaré

Practice is best served by a good theory.

L. Boltzmann

PREFACE

My work in the field of ice mechanics began in early 1991 when Dr. Shyam Sunder approached me to work with him. The first thing that I worked on was developing a numerical algorithm for the transient creep constitutive equations developed in the thesis of Mao Wu (*PhD Thesis, MIT* (1990)). This work resulted in a publication entitled: *Numerical Modeling of Transient Creep in Polycrystalline Ice, J. Engineering Mechanics, Vol. 119.*

In 1992 Dr. Shyam Sunder received a major grant from the Office of Naval Research to develop physically based constitutive models for ice. In the proposal, I was to develop numerical models for creep and compressive damage in polycrystalline ice. My research was to be based on Mao Wu's thesis. After developing a damage descriptor for polycrystalline ice (Elvin and Shyam Sunder (1993), *Micromechanical damage descriptor for polycrystalline ice, in: Ice mechanics- '93*) and extending the damage model of Wu (Elvin and Shyam Sunder (1994), *Compliance of polycrystalline ice with evolving microcrack population, in: Proceedings of the Europe-US Workshop on Fracture of Quasibrittle Materials: Experiments, Theory and Computation*) serious doubt was cast on whether microcrack damage can cause softening in polycrystalline ice. Results from finite element simulations of indentation of an ice sheet which damaged according to the above mentioned models, differed very little from simulations run with undamaged ice sheets! This is due to the fact that under fast compressive loading, the stiffness component in the direction of the most compressive principal stress changes insignificantly with damage accumulation.

Further, the damage models were based on pre- existing precursor cracks. Such precursor cracks are observed experimentally. Theoretically, these precursors were assumed to be caused by elastic anisotropy mismatch between neighboring grains. However, upon careful analysis, it was discovered that the elastic anisotropy mechanism was not strong enough to produce these precursors. The work presented in this thesis starts off by examining what causes microcracks in polycrystalline ice loaded at fast strain rates in compression.

I would like to thank several people who influenced the research presented in this thesis. First I acknowledge the influence of my thesis committee: Professors Jerome Connor (Committee Chairman), L. Ananad (Mechanical Engineering), K.J. Bathe (Mechanical Engineering), M. Kachanov (Tufts University), C.K. Leung (Civil Engineering) and Dr. S. Shyam Sunder (NIST). Special thanks go to Professor Connor who agreed to become my supervisor in late 1994 when Dr. Shyam Sunder left for NIST. I appreciate the help and useful comments made by my brother, Neill Elvin. I acknowledge several people in the ice mechanics community with whom I had useful discussions especially at conferences: Prof. Schulson, Dr. Cole, Prof. Dempsey, Prof. Gupta, Dr. Gow, Dr. Meese, Dr. Shapiro, Prof. Bazant, among many others. The comments made by Prof. Nemat-Nasser on Chapter 3 (which he reviewed for the journal *Mechanics of Materials*) are noted.

A.E. 1996

Contents

Chapter 1

INTRODUCTION

The field of ice mechanics spans over multiple scales and encompasses many material behaviors. In a recent state of the art workshop on ice mechanics (Ref. [6]) five length scales were identified. These include:

1. 100 kilometer scale– this resolution sees pack ice.
2. 10 kilometer scale– this resolution sees floe clusters.
3. 1 kilometer scale– this resolution sees single floes, ridges, leads.
4. 1- 100 meter scale– this resolution sees macro cracks.
5. 0.1- 1 meter scale– this resolution sees microcracks and single crystals.

The understanding and results produced from each scale can be used as input assumptions into the next larger scale.

Research on the various scales in ice mechanics can be classified into the following major problem areas.

1. Ice loads on structures (*e.g.* offshore oil platforms, ships, bridge pears).
2. Design of ice structures (*e.g.* ice islands and drilling platforms, ice roads for vehicles and railways, parking lots, runways for aeroplanes).
3. Ice failure (*e.g.* penetration of ice plates by submarines, in-plane indentation of ice sheets by oil platforms, bearing capacity of ice plates).
4. Ice adhesion on surfaces.
5. Geophysics of ice movement (*e.g.* glacier flow, iceberg dynamics, opening up of holes in the arctic ice pack).

These areas can also be grouped together in various combinations, with results from one area effecting the other problems in the group. The book by Sanderson (1988) addresses all these problem areas, except the ice adhesion problem, and provides a comprehensive reference list on these topics.

The research conducted in this thesis focuses on the multiple ice grain scale– the smallest scale considered in Ref. [6]. The resolution in the modeling is such that the grain structure is visible. Each grain, however, is assumed to be homogeneous. The results from this research will impact the scales associated with the problems of ice failure, and designing ice structures.

The first problem that is addressed in this thesis deals with the precursors of failure. It can be stated as: What causes microcracking in polycrystalline ice loaded at high strain rates? The second task seeks to determine: How many grains are required to homogenize the elastic properties of polycrystalline ice? This identifies the representative volume (or area) element which defines the smallest control area that has to be considered in micromechanical analyses. The results from these two tasks then prompts the question: Is there a thickness effect on the transverse shear modulus of ice plates? Finally, if the transverse shear modulus is effected either by plate thickness, or by temperature, then what effect does this have on floating ice plate deformation?

In answering these questions it will be shown how the micromechanical scale (multiple grain or polycrystal scale) controls the behavior at larger, or ice plate scales. The latter scale is of engineering interest.

1.1 Material Behavior

Polycrystalline ice is a high temperature material. Naturally occurring terrestrial ice is usually found in $-40°C$ to $0°C$ temperature range, this corresponds to homologous temperatures greater than 0.85. The deformation of ice is highly non-linear and depends on loading rate, temperature as well as on the granular microstructure.

At slow loading rates (strain rates $< 10^{-5}s^{-1}$) ice shows purely ductile, viscoplastic behavior. At fast loading rates (strain rates $> 10^{-3}s^{-1}$) and/ or colder temperatures, ice behavior is predominantly linear and brittle. The maximum stresses in ice occur at strain rates associated with the ductile to brittle transition.[1] Under compression, accumulation of microcracks is observed in the ductile-to-brittle, and brittle regimes. These microcracks coalesce leading to failure in the brittle regime. In tension, on the other hand, only a few microcracks form before one of the microcracks grows unstably. For more detailed discussions of polycrystalline ice behavior, both in the ductile and in the brittle regimes, see the work of Schulson and co- workers, Sinha and co- workers, Cole, and Gold, among many others. Several of these references are given at the end of this chapter.

The research in this thesis concentrates only on the brittle regime where the loading rate and

[1]This is a currently held view, although stresses in the brittle regime have approximately the same magnitude as those in the ductile to brittle zone (see *e.g.* Schulson (1991)). Note that the failure stresses in the brittle regime exhibit considerable scatter.

temperature is such that the polycrystalline behavior is approximately linear.

1.2 Single Crystal Properties

To avoid repetition in each chapter, the single crystal elastic stiffness used in this thesis are presented only once here.

The values for the dynamic elastic moduli of ice single crystals are reported in the literature. The data of Dantl (1969) and Gammon *et al.* (1983) are the most comprehensive and accurate available to date. The maximum difference between the elastic stiffness components of these two data sets is 5.45 % at $-16°C$. The reported uncertainty in the stiffness data of Gammon *et al.* (1983) is less than in Dantl (1969): the maximum uncertainty is $\pm 0.46\%$ in the data of Gammon *et al.* (1983) and $\pm 7\%$ in the data of Dantl (1969). Further, as pointed out by Nanthikesan and Shyam Sunder (1994) the stiffness and compliance data of Gammon *et al.* (1983) satisfies the inverse relationship, while the data of Dantl (1969) does not. Although using the stiffness data from either reference will have little effect on the results in this thesis, in view of the above, the data of Gammon *et al.* (1983) are used in all simulations.

The dynamic elastic stiffness of a single ice crystal, measured using Brillouin spectroscopy at $-16°C$ is reported in Gammon *et al.* (1983):

$$\mathbf{C}_g^{3D}(\zeta = 0°) = \begin{pmatrix} 15.010 & 5.765 & 5.765 & & & \\ & 13.929 & 7.082 & & 0 & \\ & & 13.929 & & & \\ & & & 3.4235 & & \\ & \textit{sym.} & & & 3.014 & \\ & & & & & 3.014 \end{pmatrix} \; GPa \tag{1.1}$$

where in the grain's axes system $x_2 - x_3$ is the isotropy plane in the transversely isotropic crystal; the c-axis of the crystal lies in the x_1 direction ($\zeta = 0°$). The $3D$ superscript refers to the three dimensional nature of the elastic stiffness tensor. Where it is permitted, this superscript is dropped. The reduction of the single grain's elasticity tensor to planar conditions is performed in each chapter as needed.

The above elastic constants are mildly temperature dependent. The following empirical relationship for the stiffness at temperature T is presented in Gammon *et al.* (1983):

$$\mathbf{C}_g^{3D}(T) = \mathbf{C}_g^{3D}(T_{ref}) \, \frac{(1 - 1.418 \times 10^{-3} T)}{(1 - 1.418 \times 10^{-3} T_{ref})} \tag{1.2}$$

where T_{ref} is the temperature at which $\mathbf{C}_g^{3D}$ is known ($T_{ref} = -16°\mathrm{C}$), and all temperatures are measured in degrees Celsius. Equation (1.2) shows that between $0°C$ and $-20°C$ the variation in dynamic stiffness of a single crystal is practically negligible.

1.3 Organization of Thesis

This thesis is based on six journal articles written in the course of research. In Chapter 2 the cause of microcracking in polycrystalline ice is investigated. First uniaxial loading and then biaxial compressive loading is considered. Serious doubt is cast on the grain anisotropy mechanism which was thought to be responsible for microcracking in ice at high strain rates. A new mechanism of grain boundary deformation gives more realistic and plausible results. The effects of material microstructure and loading conditions are investigated. Under microstructure, the grains' elastic anisotropy, size and shape as well as free and retarded grain boundary deformation are investigated. The effects of direction of uniaxial compression, and biaxial confinement, are simulated.

In Chapter 3 the number of grains required to homogenize the elastic properties of polycrystalline ice is determined. Polycrystalline ensembles with grains of random shapes but approximately equal areas are generated by Voronoi tessellation. The limiting cases of no grain boundary deformation and free grain boundary slip are considered. The distributions of the stress components at grains' centers are investigated.

Chapters 2 and 3 investigate the grain structure in the horizontal plane, *i.e.* the plane of the ice sheet. But what about the vertical plane? Chapter 4 studies the effects grain microstructure and grain boundary deformation have on the transverse shear modulus of ice plates of various thickness. Since there are relatively few grains through the thickness of ice plates, the microstructural geometry of the entire thickness can be modeled, albeit in an idealized way.

The deformation of floating ice plates under point loading is investigated in Chapter 5. Following the results from Chapter 4, both shear and bending deformation are accounted for in calculating deflections of ice plate. The horizontal plane Young's modulus, and the transverse shear modulus of ice plates of various thickness are calculated from deflection data. The inclusion of shear deformation might provide an explanation for two major concerns raised about the previously calculated Young's modulus of thin model ice sheets.

The thesis is concluded by a summary of salient results, the implication of these results, and possible future research based upon the work presented.

References

[1] Cole, D.M., (1987), Strain-Rate and Grain-Size Effects in Ice, *Journal of Glaciology*, Vol. 33, pp. 274-280.

[2] Dantl, G., (1969). Elastic Moduli of Ice, In Ed. Rielhl, N., Bullemer, B., and Engelhardt, H., *Physics of Ice*, Plenum Press, New York, pp. 223-230.

[3] Gammon, P.H., Kiefte, H., Clouter, M.J., and Denner, W.W. (1983). Elastic Constants of Artificial and Natural Ice Samples by Brillouin Spectroscopy, *Journal of Glaciology*, Vol. 29, pp. 433-460.

[4] Gold, L.W., (1972), The Process of Failure of Columnar- Grained Ice, *Philosophical Magazine*

A, Vol. 26, pp. 311-328.

[5] Nanthikesan, S., and Shyam Sunder, S. (1994). Anisotropic Elasticity of Polycrystalline Ice I_h, *Cold Regions Science and Technology*, Vol. 22, pp. 149- 169.

[6] *Proceedings of the Sea Ice Mechanics and Arctic Modeling Workshop*, April 25- 28 1995, Anchorage, Alaska, Organized by Northwest Research Associates, Inc., Bellevue, WA.

[7] Sanderson, T.J.O., (1988), *Ice Mechanics, Risk to Offshore Structures*, Graham and Trotman, London.

[8] Schulson, E.M., (1991), The Tensile and Compressive Fracture of Ice, *Ice- Structure Interaction*, eds S. Jones, R. McKenna, J. Tillostson, and I. Jordaan, Springer- Verlag, Berlin.

[9] Sinha, N.K., (1988), Crack-enhanced Creep in Polycrystalline Material: Strain-rate Sensitive Strength and Deformation of Ice, *Journal of Material Science*, Vol. 23, pp. 4415- 4428.

[10] Smith, T.R., and Schulson, E.M., (1993), The Brittle Compressive Failure of Fresh-Water Columnar Ice Under Biaxial Loading, *Acta Metallurgica et Materialia*, Vol. 41, pp. 153-163.

Chapter 2

MICROCRACKING DUE TO GRAIN BOUNDARY SLIDING IN POLYCRYSTALLINE ICE UNDER COMPRESSION

ABSTRACT

This paper examines grain boundary sliding as a mechanism for nucleation and growth of microcracks in polycrystalline $S2$ ice, under uniaxial and biaxial compression. The effects of (a) planar confinement, (b) retarding grain boundary slip, and (c) microstructural parameters are studied. The loading rate is fast enough so that the polycrystal response is almost linear. An unit cell model is set up and the resulting boundary value problem solved using the finite element method.

Simulations show that by allowing grain boundary sliding a defect originating at the triple point grows stably, reaches a critical length and then propagates unstably to the neighboring triple point. The influence of the elastic mismatch between neighboring grains on microcracking stress is not strong. The stress causing microcrack growth is found to be inversely proportional to the square root of the grain size.

Confinement increases the microcracking stress. For confinement ratios greater than 0.2, with free grain boundary sliding, facet length microcracks are not realizable. Retarding grain boundary sliding increases the microcracking stresses approximately exponentially. Simulations show that under uniaxial compression microcracking is only possible in a 25° range to either side of the loading axis. If no grain sliding takes place, and only the elastic anisotropy mechanism operates, the stresses required for microcrack nucleation and growth are unrealisticly high; the resulting microcracks are also too short.

2.1 INTRODUCTION

The deformation of polycrystalline ice is highly non-linear and depends on loading rate, temperature as well as on the granular microstructure. While at low loading rates (less than $\approx 10^{-3}\ s^{-1}$ in compression) ice is ductile, it fails brittlely at higher rates and lower temperatures. The maximum stresses occur in the ductile to brittle transition regime. Under compression, microcrack accumulation is observed in this regime. Experimental evidence in Gold (1972) suggest two independent families of microcracks which nucleate in polycrystalline ice. The first microcrack family is independent of creep strain while the second is dependent on it.

The nucleation of microcracks, which are dependent on creep strain, has been attributed to the dislocation pile up mechanism by Schulson (1979) and Cole (1988) and to grain boundary sliding (Sinha (1982), Sinha (1984)). Both these mechanisms were postulated for low strain rate loading where the polycrystal behaves in a ductile manner.

The elastic anisotropy mechanism has been postulated in Cole (1988) and Shyam Sunder and Wu (1990) to be responsible for the formation of the strain- independent microcracks. This mechanism was thought to be dominant during high strain rate loading. More recently however, the stress fields which arise in the grains due to the actual anisotropy found in ice was analyzed in Gupta *et al.* (1993). In this reference it was concluded that the mismatch in elastic moduli between neighboring grains in ice, under plane strain conditions, is not high enough to form precursor cracks.

This chapter conducts a theoretical investigation of microcrack nucleation and growth in fresh water polycrystalline $S2$ ice at the high end of the ductile-to-brittle transition where the response is almost linear. Since the elastic anisotropy mechanism acting alone is not strong enough to nucleate precursor cracks, grain boundary sliding is investigated as a possible cause of microcracking. Both uniaxial and biaxial compressive loading is considered. The aim is to predict at what stress microcracks nucleate and grow. The effects of (a) biaxial compression, (b) retarding free grain boundary slip, and (c) microstructural parameters, on microcracking are investigated. The microstructural parameters considered are (a) grain size, (b) random grain orientations, (c) grain shape, and (d) direction of loading with respect to the microcrack.

Polycrystalline ice, even that prepared in the laboratory, is a porous material. The bubble size and density is a function of freezing rate and the bubble shape can be approximated by cylinders or prolate spheroids (Carte (1961)). Currier and Schulson (1982) studies isotropic polycrystalline ice with equiaxed grains prepared in the laboratory, and reports average bubble diameters of 0.06 and 0.12 mm for grain sizes between 1 and 2 mm and 2 and 7.3 mm, respectively. The bubble density is 2000 and 350 bubbles/cm^3 respectively. The nucleation and growth of a microcrack from a circular hole in an isotropic material is modeled in Sammis and Ashby (1986). The minimum nucleation stress predicted by Sammis and Ashby (1986) under uniaxial compression using homogenized properties of ice is an order of magnitude larger than observed experimentally. At this stress level the microcrack length is of the order of 0.18 bubble diameters, viz. $0.018mm$, as compared with experimentally observed microcracks which are of the order of the grain size (Cannon *et al.* (1990)), viz.

of the order of millimeters. The effect of including the local inhomogeneity of the ice grains, as well as grain boundary sliding, on a microcrack originating from a bubble, is studied in this chapter.

The stresses arising in a polycrystal array are studied using a repetitive unit cell model. The concept of the unit cell is well known; the work reported in Tvergaard and Hutchinson (1988) on ceramics and in Gupta *et al.* (1993) on saline ice is closest to this study. The major difference between this work and these references is the modeling of grain boundary sliding. Of course differences in the size and physical details of the unit cell also exist; the present chapter models anisotropic grains and air bubbles located at the triple points.

The organization of this chapter is as follows. The unit cell model is developed in Section 2.2: the physical details of the unit cell are described and the motivation for the grain boundary sliding mechanism is given. Section 2.3 formulates the unit cell as a boundary value problem, describes the method of analysis of the boundary value problem, and states the criterion for microcrack nucleation and growth. The material parameters used in the simulations are given in Section 2.4. The discussion of the results from the simulations is presented in Section 2.5. The effects of preventing grain boundary sliding and the question of simultaneous coexistence of grain boundary sliding and elastic behavior of the polycrystal is addressed in Section 2.5.1. The effects of grain anisotropy, biaxial confinement, retarding grain boundary sliding, and microstructural parameters on the stresses required for microcrack nucleation and growth are discussed in Sections 2.5.2 to 2.5.5 respectively.

2.2 The Unit Cell Model

The whole domain is subdivided into repetitive unit cells (see Fig. 2-1). The response of the entire domain to far field loading can be obtained by analyzing only the unit cell. In order to define the unit cell, an assumption has to be made on the size of the repetitive cell. This size fixes the number of grains and hence the number of grain orientations modeled.

2.2.1 Physical Details of Unit Cell

In this chapter the grain geometry is idealized by hexagons. The unit cell is made up of three grains with orientations ζ_A, ζ_B, and ζ_C; see Fig. 2-1 and for details Fig. 2-2b. The assumption of modeling only three grain orientations is not as restrictive as it first appears, since: (i) the individual ice crystals exhibit weak elastic anisotropy, and (ii) the effect of anisotropy on microcracking is not strong (see details in Sections 2.5.2 and 2.5.5).

The shape of the grains in this study are defined by the angle θ, see Fig. 2-2. This angle, together with grain boundary sliding, influences the strength of the singularity at the tip of the microcrack, *i.e.* the degree to which Grain A wedges apart Grains B and C. When $\theta = 120°$, the grain shapes are regular hexagons.

The unit cell is assumed to be under plane stress conditions. This is consistent with the

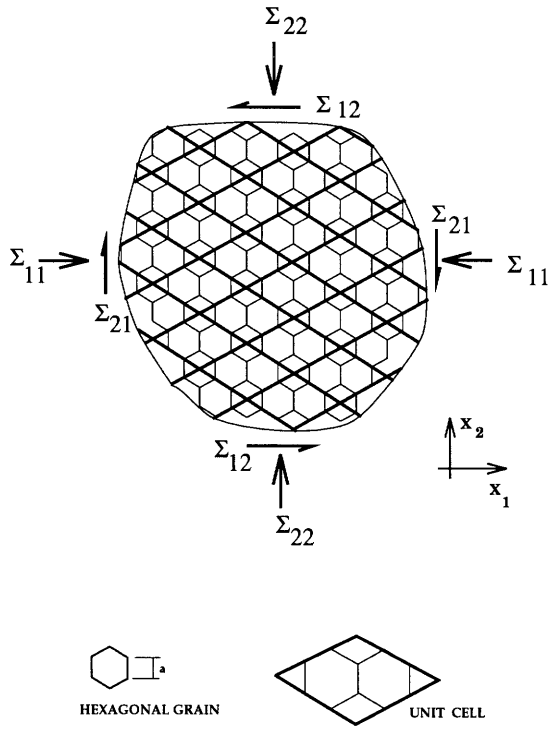

Figure 2-1: The polycrystalline domain of hexagonal grains showing the mosaic of repetitive unit cells.

microstructure of transversely isotropic $S2$ ice where the cell lies in the plane of polycrystal isotropy.

Observations show that bubbles have a tendency to concentrate on grain boundaries, especially at geometric discontinuities. Cylindrical air bubbles are located at triple points in the interior of the cell (at TP1 and TP2 in Fig. 2-3). These bubbles extend through the thickness of the cell.

The ice surface contains flaws in the form of steps, pits and ledges. The steps can have a depth ranging from 0.1 to 4 μm (Hobbs (1974)). Such flaws are likely to be present on the bubble surface and might nucleate into microcracks. The details of the triple point TP1 containing a bubble with a microcrack are shown in Fig. 2-2b. At the start of microcracking, the microcracks are far apart. Thus only a single microcrack emanating from TP1 is considered in this chapter.

2.2.2 Grain Boundary Sliding

Grain boundaries are zones of finite volume where the material is highly disordered when compared with the material inside the grains. The grain boundary thickness has been predicted in Chatterjee and Jellinek (1971) to be of the order of a fraction to a few microns in thickness and to be dependent on temperature and salinity. Due to the disorder, the entropy of the grain boundaries is higher than that of the grain. Decohesion pockets also form on the grain boundaries (Picu and Gupta (1994)). Thus the elastic stiffness moduli of the grain boundary zone are expected to be lower than those of the grain.

Naturally occurring polycrystalline ice is typically found in the temperature range $0° \; C \geq T \geq$

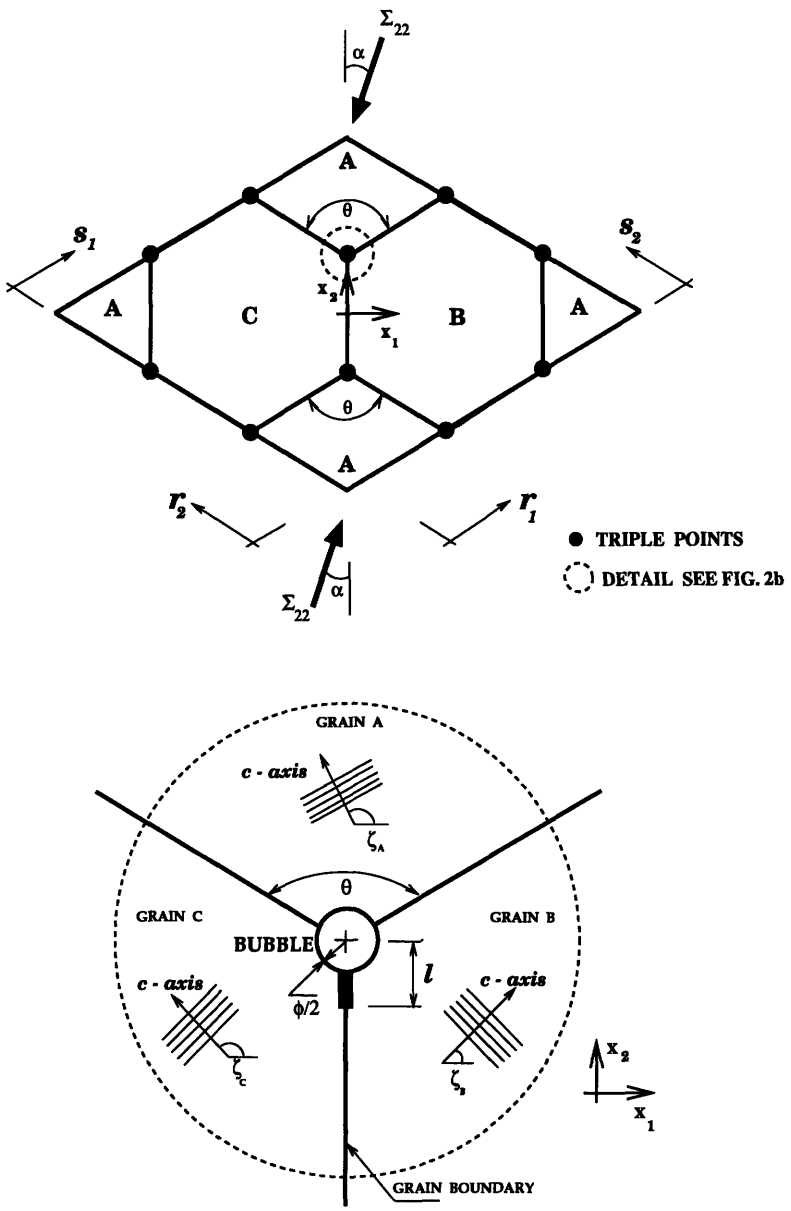

Figure 2-2: (a) The unit cell model. (b) Detail of a triple point junction located within the unit cell.

$-40°C$. This corresponds to a homologous temperature range of $1 \geq T_h \geq 0.85$. The behavior of the grain boundary zone in polycrystalline ice is very complex and its nature is not fully understood. The grain boundary zone is sensitive to temperature. There is experimental evidence of a liquid, or a quasi-liquid, layer on the grain boundaries at temperatures above $-10°C$ (see the references in the review article of Barnes *et al.* (1971)). Such a layer would promote grain boundary sliding.

From internal friction experiments on single- and polycrystalline ice, a relaxation phenomenon associated only with grain boundaries was deduced in Tatibouet *et al.* (1987). By measuring the Young's modulus, Gold and Traetteberg (1974) found two active relaxation processes both in columnar grained and in isotropic equiaxed polycrystalline ice. The first process has a relaxation

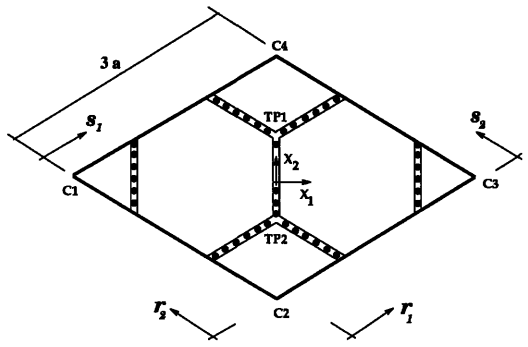

Figure 2-3: A schematic representation of the unit cell with rollers on the grain boundaries.

time of the order of $1s$, while the second is associated with a much longer time period. These authors observed that the time dependence of Young's modulus for times greater than $0.1s$ is dominated by the second, *i.e.*, slower, relaxation process.

The duration of high strain rate tests, where the response of the polycrystal is almost linear and the sample fails in a brittle manner, is typically less than a few seconds. Brittle behavior is observed when the applied strain rates are in the range $10^{-3}s^{-1} \leq \dot{\epsilon} \leq 10^{-1}\ s^{-1}$ (see for example the work of Schulson and co-workers). For these short durations, the first relaxation phenomenon observed in Tatibouet *et al.* (1987) must be active; this relaxation process might be associated with grain boundary sliding. During the progress of this work it has come to the author's attention that visco-elastic grain boundary sliding has been observed at $\dot{\epsilon} = 10^{-2}\ s^{-1}$ and $\dot{\epsilon} = 10^{-3}\ s^{-1}$ at $T = -10°C$ by Picu and Gupta (1994). [1] The seemingly contradictory simultaneous occurrence of grain boundary sliding and linear response of the polycrystal will be explored in Section 2.5.1 after the unit cell model has been fully described.

In the unit cell the grain boundary region can be modeled as a linear visco-elastic material. However, since the material parameters of the grain boundary are not known, and for simplicity, the grain boundaries are assumed to be either fully or partially relaxed. Thus in the model the grain boundaries can transfer only a portion of the total shear stresses they experience. The assumption of free grain boundary sliding forms the base case. This should under predict the stresses that cause microcrack nucleation and growth. Further, since the grain boundary thickness (order of micrometers) is much smaller than the dimensions of the grain (order of millimeters), the grain boundary thickness is ignored in the unit cell model.

2.3 Microcrack Nucleation and Growth

In order to determine the microcrack nucleation stress, the stresses required to extend the microcrack and the path of the microcrack, the spatial distributions of stress, strain and displacement, within the unit cell, are required. The geometry of the unit cell has already been defined. In this section the unit cell boundary value problem is first formulated and then solved using the finite

[1] These authors attribute *stable* microcrack *nucleation* to grain boundary sliding.

element method. The method of retarding grain boundary sliding is given. The criterion for crack nucleation and growth is then presented.

2.3.1 Formulation and Analysis of the Unit Cell Boundary Value Problem

The polycrystalline aggregate (see Fig. 2-1) is subjected to biaxial far field stress, Σ_{22}, $\Sigma_{11} = \lambda\Sigma_{22}$ and $\Sigma_{12} = 0$, where Σ_{22} is rotated by α to the x_2 axis (see Fig. 2-2a). Advantage can be taken of the repetitive nature within the aggregate; only a single unit cell needs to be considered.

Equilibrium within the cell is automatically met by satisfying the principle of virtual work:

$$\int_A \delta\epsilon \bullet \boldsymbol{\sigma} \, \mathrm{d}A = \int_S \delta\mathbf{u} \bullet \mathbf{T} \, \mathrm{d}S \tag{2.1}$$

where $\delta\epsilon$ and $\boldsymbol{\sigma}$ are the virtual strain and stress tensors at a point, $\delta\mathbf{u}$ is the virtual displacement and $\mathbf{T}$ is the surface traction. Integration is performed over the entire unit cell area, A, and over the entire boundary length S. The elastic stress- strain relation for a grain is:

$$\boldsymbol{\sigma} = \mathbf{C_G}(\zeta)\epsilon \tag{2.2}$$

where $\mathbf{C_G}(\zeta)$ is the elastic stiffness tensor of a single grain in the global reference frame and it depends on the basal plane orientation, ζ (see Fig. 2-2b). Under planar conditions, the stiffness tensor in the global axes system $\mathbf{C_G}(\zeta)$, is related to the grain's stiffness in the grain's coordinate system, $\mathbf{C}_g$ by:

$$\mathbf{C_G}(\zeta) = \mathbf{R}^T\mathbf{C}_g\mathbf{R} \tag{2.3}$$

where T is the transpose operation, and the transformation tensor $\mathbf{R}$ is given by:

$$\mathbf{R} = \begin{pmatrix} \cos^2(\zeta) & \sin^2(\zeta) & 1/2\sin(2\zeta) \\ \sin^2(\zeta) & \cos^2(\zeta) & -1/2\sin(2\zeta) \\ -\sin(2\zeta) & \sin(2\zeta) & \cos(2\zeta) \end{pmatrix} \tag{2.4}$$

Substituting Eq. (2.2) into Eq. (2.1), the principle of virtual work to be satisfied, is:

$$\int_A \delta\epsilon \bullet (\mathbf{C_G}(\zeta)\epsilon) \, \mathrm{d}A = \int_S \delta\mathbf{u} \bullet \mathbf{T} \, \mathrm{d}S \tag{2.5}$$

Traction boundary conditions corresponding to far field loading are applied to the sides of the unit cell. Labels of the unit cells sides are shown in Fig. 2-3. The normal T_n and tangential T_t traction boundary conditions applied to the perimeter of the unit cell are given by:
Along side r_1:

$$T_n = -\frac{\Sigma_{22}}{4}[(3+\lambda)\cos^2\alpha + (1+3\lambda)\sin^2\alpha - \sqrt{3}(1-\lambda)\sin(2\alpha)]$$

$$T_t = -\frac{\Sigma_{22}}{4}[\sqrt{3}(1-\lambda)\cos(2\alpha) + (1-\lambda)\sin(2\alpha)]$$

Along side r_2:

$$T_n = -\frac{\Sigma_{22}}{4}[(3+\lambda)\cos^2\alpha + (1+3\lambda)\sin^2\alpha + \sqrt{3}(1-\lambda)\sin(2\alpha)]$$

$$T_t = -\frac{\Sigma_{22}}{4}[-\sqrt{3}(1-\lambda)\cos(2\alpha) + (1-\lambda)\sin(2\alpha)]$$

Along side s_1:

$$T_n = -\frac{\Sigma_{22}}{4}[(3+\lambda)\cos^2\alpha + (1+3\lambda)\sin^2\alpha - \sqrt{3}(1-\lambda)\sin(2\alpha)]$$

$$T_t = -\frac{\Sigma_{22}}{4}[\sqrt{3}(1-\lambda)\cos(2\alpha) + (1-\lambda)\sin(2\alpha)]$$

Along side s_2:

$$T_n = -\frac{\Sigma_{22}}{4}[(3+\lambda)\cos^2\alpha + (1+3\lambda)\sin^2\alpha + \sqrt{3}(1-\lambda)\sin(2\alpha)]$$

$$T_t = -\frac{\Sigma_{22}}{4}[-\sqrt{3}(1-\lambda)\cos(2\alpha) + (1-\lambda)\sin(2\alpha)] \tag{2.6}$$

Note that the normal traction, T_n is positive into the unit cell, and the tangential traction, T_t is positive counter clockwise around the unit cell. The confinement ratio λ is kept constant in each simulation. In this study, two loading conditions are considered. Namely, biaxial compression with $\alpha = 0$, and uniaxial compression with various α. The special case of no confinement ($\lambda = 0$) and aligned uniaxial compression ($\alpha = 0$) forms the base uniaxial case.

In addition the following displacements are prescribed:
Point C1, the center of grain A, is pinned:

$$u_1 = u_2 = 0 \tag{2.7}$$

Displacement of Point C3:

$$u_2 = 0 \tag{2.8}$$

Free grain boundary sliding is allowed by specifying rollers on the grain boundaries (see Fig. 2-3). These rollers cannot transfer shear tractions but can transfer both tensile and compressive normal tractions. When the free sliding is retarded , the rollers are augmented with springs lying on the grain boundary (see the next section). Note that Fig. 2-3 is schematic; the grain boundary thickness is assumed to be zero. The free sliding conditions on the grain boundaries located on the perimeter of the cell are specified below.

The boundaries of the unit cell have to be constrained to maintain compatibility with neighboring cells. To this end, length measures along the perimeter of the cell are defined (see Fig. 2-3): r_1 and r_2 from Point C2, and s_1 and s_2 from Points C1 and C3, respectively. Compatibility is

maintained within grain A if:
In the ranges $0 \leq r_1 \leq a$ and $2a \leq r_1 \leq 3a$

$$\begin{aligned} u_1(r_1) - u_1(C2) &= u_1(s_1) - u_1(C1) \\ u_2(r_1) - u_2(C2) &= u_2(s_1) - u_2(C1) \end{aligned} \tag{2.9}$$

In the ranges $0 \leq r_2 \leq a$ and $2a \leq r_2 \leq 3a$

$$\begin{aligned} u_1(r_2) - u_1(C2) &= u_1(s_2) - u_1(C3) \\ u_2(r_2) - u_2(C2) &= u_2(s_2) - u_2(C3) \end{aligned} \tag{2.10}$$

To allow slip on grain boundaries found on the perimeter of the cell, and to maintain compatibility with neighbors, the following constraints on deformations are required.
In the range $a \leq r_1 \leq 2a$

$$u_2(r_1) - u_2(C2) - u_2(s_1) + u_2(C1) = \frac{1}{\sqrt{3}}(u_1(r_1) - u_1(C2) - u_1(s_1) + u_1(C1)) \tag{2.11}$$

In the range $a \leq r_2 \leq 2a$

$$u_2(r_2) - u_2(C2) - u_2(s_2) + u_2(C3) = \frac{1}{\sqrt{3}}(u_1(r_2) - u_1(C2) - u_1(s_2) + u_1(C3)) \tag{2.12}$$

The average axial strain, $\bar{\epsilon}_{22}$, experienced by the unit cell is defined as:

$$\bar{\epsilon}_{22} = \frac{1}{6a}\int_0^{3a} \frac{u_2(3a - s_2) - u_2(r_1)}{3a - r_1}\, \mathrm{d}r_1 + \frac{1}{6a}\int_0^{3a} \frac{u_2(3a - s_1) - u_2(r_2)}{3a - r_2}\, \mathrm{d}r_2 \tag{2.13}$$

where $(\bullet)$ is the argument of the function u_2. The displacement component, u_2 is defined on the cell perimeter and the length measures r and s can be interchanged. The integration is performed numerically and Points C1 and C3 are excluded.

The finite element method is used to solve the boundary value problem defined by Eq. (2.5) subjected to boundary conditions given in Eq. (2.6) to Eq. (2.12). A typical mesh containing 388 elements is shown in Fig. 2-4a. Figure 2-4b shows the refined mesh around the bubble containing the microcrack. The discretization is conducted so that the elements do not intersect the grain boundaries. The mesh contains standard eight node isoparametric elements. At the crack tip eight, singular, quarter- point elements are used. Full 3×3 Gauss integration is performed. The discretization ensures that a node found at a distance r_1 from C2 will have a counterpart at the same distance s_1 from C1; the same applies to r_2 and s_2.

The level of discretization, and the imposition of the boundary conditions on the unit cell have been checked as follows. First, the finite element solution with no grain boundary sliding and isotropic homogeneous grains compares well with the known analytical solution of the stress distribution around a circular hole. In the numerical solution, although the domain contains multiple

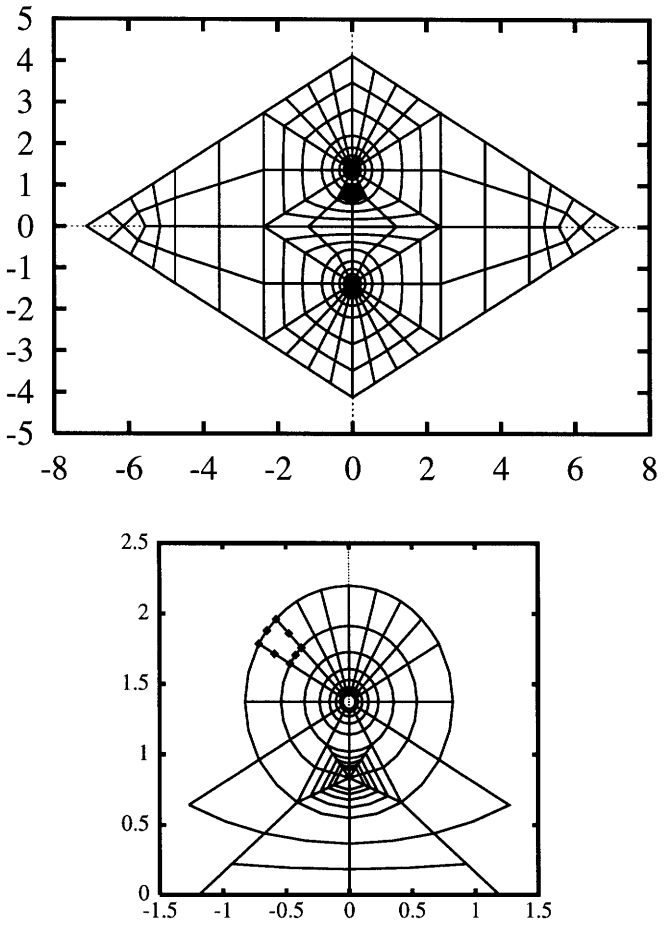

Figure 2-4: (a) Finite element discretiziation of the unit cell. (b) Detail of finite element discretiziation around the bubble and the microcrack.

holes, their diameter is small compared to the distance between them and hence their effect on each other is negligible. Second, when grain boundary sliding is allowed, the compatibility of deformations on the boundary of neighboring unit cells has been checked. Finally, for a symmetric distribution of grain orientations about the line $C2 - C4$, and for a symmetric far field loading, the symmetry of the solution has been verified.

2.3.2 Retarded Grain Boundary Sliding

The effect of retarding the free grain boundary sliding is studied by allowing some shear stress transfer between the grains. This is achieved by introducing an elastic layer on the grain boundary having a stiffness s per unit area (or per length if unit thickness is considered) of boundary. This layer is modeled by springs lying on, and aligned with the grain boundary; the springs connect

points on either side of the boundary. [2] If Δ is the relative slip between these two points, and S is the shear force transfered per unit length of the grain boundary then:

$$S = s\Delta \tag{2.14}$$

The average amount of shear force transfered along the grain boundary can be defined as:

$$\overline{S} = \frac{1}{a}\int_0^a s\Delta \, dx = k\overline{\Delta} \tag{2.15}$$

where a is the grain facet length and $\overline{\Delta}$ is the average relative slip between grains. If $s = 0$ then *free* grain boundary sliding is allowed, *i.e.* no shear transfer. If $s = \infty$ then the springs are rigid and there is *no* grain boundary sliding, *i.e.* full shear transfer and $\overline{\Delta} = 0$. Note that the latter case corresponds to the penalty method in finite elements; when implementing numerically, ks is set to a large number and care must be taken to ensure that round off and chop off errors do not effect the solution.

Two notes on implementing the grain boundary springs in the unit cell model should be made. First, since the distances between the nodes on the grain boundary are not the same, the discrete stiffnesses of the springs cannot be the same if the grain boundary elastic layer is to have a constant s. Second, for simplicity, free slip on the grain boundaries found on the perimeter of the unit cell is allowed. This should have little effect, since the sliding of grain A controls the microcracking in the unit cell.

At present the grain boundary zone in ice is not well understood and all its mechanical properties are unavailable. For this reason, the effect of a range of shear stress transfer on microcracking is analyzed. Defining χ to be the fraction of shear stress transfer:

$$\chi = \frac{\overline{S}}{S^*} \tag{2.16}$$

where S^* is the shear force transfered when no grain boundary slip occurs ($s = \infty$); S^* is determined from the distribution of shear stresses on the grain boundary. The fraction χ lies in the range $0 \leq \chi \leq 1$. The two limiting cases of $\chi = 0$ and $\chi = 1$ correspond to free grain boundary slip (no shear stress transfer), and no slip (full shear stress transfer). The base case considers $\chi = 0$.

2.3.3 Criterion for Microcracking

The nucleation of the flaw located at the triple point and the propagation of the resulting microcrack occurs when the energy released in forming the crack is greater than the surface energy of the material. Even though the far field stress is uniform, locally the stress state is not homogeneous. This is due to grain anisotropy and discontinuities such as grain boundaries. Further the material resistance to cracking is not homogeneous; the fracture surface energy of the grain boundary is less

[2] The grain boundary thickness is *assumed* to be zero here, and hence the spring length is also zero. Thus the spring stiffness has to be specified, since s is inversely proportional to the length of the spring.

than that of the grain. Thus, in general, the flaw and the microcrack are under mixed Mode I and Mode II loading, and microcrack extension is not necessarily collinear with the original crack.

Path independent integrals can provide a measure of the amount of energy released in extending a crack. Such an energy release criterion can be stated as (Hussain *et al.* (1974), Parton and Morozon (1988)): the crack will grow in the direction in which the components of the energy release vector equals the fracture surface energy. It has been shown in Budiansky and Rice (1973) that the energy release rate per unit crack tip extension in two mutually perpendicular directions x, and y is given by:

$$\begin{aligned} J_x &= \oint_\Gamma U \, \mathrm{d}y - \boldsymbol{\sigma}\mathbf{n} \bullet \frac{\partial \mathbf{u}}{\partial x} \, \mathrm{d}\Gamma \\ J_y &= -\oint_\Gamma U \, \mathrm{d}x + \boldsymbol{\sigma}\mathbf{n} \bullet \frac{\partial \mathbf{u}}{\partial y} \, \mathrm{d}\Gamma \end{aligned} \tag{2.17}$$

where U is the strain energy density, $\mathbf{n}$ is the outward unit normal to the counter clockwise integration path, Γ, and $\mathrm{d}\Gamma$ is the arc length along Γ. Note that J_x is the conventional J integral of Rice (1968).

The components of the $\mathbf{J}$ vector can be combined to give the energy released in a direction β (from Fig. 24.3 in Parton and Morozov (1988), Hussain *et al.* (1974)):

$$\mathcal{G}(\beta) = J_x \cos(\beta) + J_y \sin(\beta) \tag{2.18}$$

where β is measured from the x-axis. The crack will extend in a direction β when:

$$2\gamma(\beta) = \mathcal{G}(\beta) \tag{2.19}$$

where $\gamma(\beta)$ is the fracture surface energy; it depends on whether the crack is extending along the grain boundary or into the grain.

The components of the path independent $\mathbf{J}$ vector, Eq. (2.17), are calculated numerically from the finite element analysis. Three different paths are considered in computing the $\mathbf{J}$ components. All paths are taken through the Gauss points and pass through the centers of the elements.

In the subsequent analyses only proportional loading is considered. In each simulation the ratio of the biaxial compressive stresses Σ_{11}/Σ_{22}, *i.e.* the confinement ratio λ, is kept constant. The calculation proceeds as follows. The far field compressive stresses are kept constant while the microcrack is extended and the corresponding $\mathbf{J}$ computed. This results in $\mathcal{G}(\beta)$ as a function of crack length, l. The actual stresses required for microcrack nucleation and propagation, Σ^*_{22} and Σ^*_{11}, are obtained by scaling the applied far field stresses as follows:

$$\begin{aligned} \Sigma^*_{22} &= \Sigma_{22}\sqrt{\frac{2\gamma(\beta)}{\mathcal{G}(\beta)}} \\ \Sigma^*_{11} &= \lambda \Sigma^*_{22} \end{aligned} \tag{2.20}$$

Note that the far field loading is fully specified by Σ^*_{22} and the confinement ratio, λ.[3] The above analysis predicts the stresses, Σ^* and $\lambda\ \Sigma^*$, required to realize a microcrack of length, l, as well as providing information on the stability and trajectory of the microcrack.

2.4 Material Parameters

The material parameters used in the subsequent numerical simulations are identified here. Two groups of material parameters are required: (i) the elastic stiffness, and (ii) fracture surface energies.

The dynamic elastic stiffness tensor of a single ice crystal is presented in the introduction, Eq. (1.1). Reducing the single crystal stiffness to plane stress conditions ($\sigma_{33} = 0$) with $x_1 - x_2$ being the plane of interest, the following dynamic single crystal plane stress stiffness is obtained:

$$\mathbf{C}_g(\zeta = 0°) = \begin{pmatrix} 12.624 & 2.832 & 0 \\ 2.832 & 10.328 & 0 \\ 0 & 0 & 3.014 \end{pmatrix} \ GPa \tag{2.21}$$

The surface energies for ice at temperatures close to 0°C was determined from experimental measurements in Ketcham and Hobbs (1969). The following surface energies are reported:
Grain boundary $\gamma_{gb} = 0.065 J/m^2$
Solid vapor, or crystal $\gamma_{sv} = 0.107 J/m^2$

Experiments reported in Parameswaran and Jones (1975) on single crystals of ice at -196°C show that microcracks do not have any preferred orientation and do not follow any particular crystallographic plane. From this observation, the variation of the surface energy with orientation within the crystal will be ignored in the simulations. Further, the surface energies reported in Ketcham and Hobbs (1969) might be temperature sensitive; currently no data is available on this sensitivity. Since surface energy is proportional to stiffness, and the variation in stiffness in the range 0°C to -20°C is negligible (Eq. 1.2), the surface energies in this range are assumed to be constant. This is a strong assumption since the properties of the grain boundaries are expected to be effected by temperature.

2.5 Simulation of Microcracking– Results and Discussion

In this section, the fundamental behavior of the unit cell is first established by considering the effects of grain boundary sliding and grain anisotropy. Subsequently, the effects of (a) loading confinement, (b) retarding free grain boundary sliding and (c) microstructural parameters on microcrack nucleation and growth is investigated. The microstructural parameters considered are:

[3] In all subsequent references to Σ^*_{22} the 22 subscript is dropped for convenience.

(i) grain size, d, (ii) random orientations of the grains, ζ, (iii) grain shape, specified by θ, and (iv) direction of loading with respect to the microcrack, α. The applied loading rate is assumed to be fast enough so as to correspond to the brittle end of the ductile-to-brittle regime.

The base case for all simulations below consists of: uniaxial compression ($\lambda = 0$) with free grain boundary sliding ($\chi = 0$), a symmetric distribution of grain orientations ($\zeta_A = 0$, and $\zeta_B = -\zeta_C$), regular hexagonal grains $\theta = 120°$ and $\alpha = 0$. Further the grain size is kept constant at $d = 5\ mm$.[4] The air bubble diameter is set to $\phi = 0.1mm$, consistent with observations in Currier and Schulson (1982) on fresh water equiaxed granular ice. Unless otherwise specified, these parameters are used in all subsequent simulations. Compressive stresses are assigned positive values.

2.5.1 Effect of Grain Boundary Sliding

The assumption of fully relaxed grain boundaries allows free slip to occur between grains. Thus no shear stress can be transfered from grain to grain and this effects the Young's modulus of the polycrystal. Zener (1941) idealized the isotropic grains by spheres, and obtained an analytical solution for the relaxed Young's modulus. The results in Zener (1941) show that the ratio of relaxed to unrelaxed Young's modulus, E_R/E, is a function of Poisson ratio only; for a Poisson ratio of 0.33, $E_R/E = 0.64$. The effect on Young's modulus, of fully relaxed grain boundaries, in a *hexagonal* array of grains can be determined using the base case unit cell model.

The Young's modulus of the polycrystal is calculated from the average quantities:

$$E = \frac{\Sigma_{22}}{\bar{\epsilon}_{22}} \tag{2.22}$$

where the average strain, $\bar{\epsilon}_{22}$, is given by Eq. (2.13). The relaxed Young's modulus is determined by leaving the constraint boundaries of the unit cell unchanged. To determine the unrelaxed Young's modulus all the rollers on the grain boundaries within the unit cell are removed. Also, on the perimeter of the unit cell the sliding constraint conditions given by Eqs (2.11) and (2.12) are replaced by no sliding constraints Eqs (2.9) and (2.10).

Simulations show that $E_R/E = 0.93$ for isotropic hexagonal grains with a Poisson ratio of 0.33. Analyzing an anisotropic, non homogeneous polycrystal with $\zeta_B = -\zeta_C$ and $\zeta_A = 0$, also shows that the difference between relaxed and unrelaxed modulus is less than 10%. The amount of relaxation is less than in Zener (1941) because in a hexagonal array, with assumed zero grain boundary thickness, there is no relative motion between the grains at each triple point. In reality the grain boundary layer has a finite volume which is much smaller than the volume of the crystal. Hence a compliant grain boundary zone will have only a small effect on the volumetric average of the overall elastic moduli. Further, the unit cell model with fully relaxed grain boundaries, prior to microcrack nucleation, shows *linear* behavior. These results of a small reduction in Young's

[4]The grain size is defined such that the area of the hexagonal grain is equal to the area of a circle with a grain size diameter.

modulus and linear behavior (*i.e.* creep strains insignificant) are consistent with experimental observations of ice loaded at high strain rates.

The possibility of a microcrack nucleating from a bubble located at a triple point surrounded by randomly oriented anisotropic grains with *no grain boundary sliding* has been studied. As already mentioned, the work in Sammis and Ashby (1986) on a circular hole in an isotropic homogeneous material predicts the *minimum* nucleation stress to be $11.8MPa$.[5] The *maximum possible* microcrack length is approximately three bubble diameters, which is an order of magnitude shorter than typical lengths observed in ice. By including the bubble and random grain orientations in the unit cell, a much larger local tensile field develops around the microcrack under far field uniaxial compression. In general the microcrack is under mixed mode loading. The stresses required to propagate the microcrack so determined, are lower than those predicted using the expression in Sammis and Ashby (1986), but they are still approximately an order of magnitude higher (depending on the orientations of the grains) than experimental observations. The maximum possible length of the microcrack is also longer than in the isotropic homogeneous case, but is still much shorter than the grain facet.

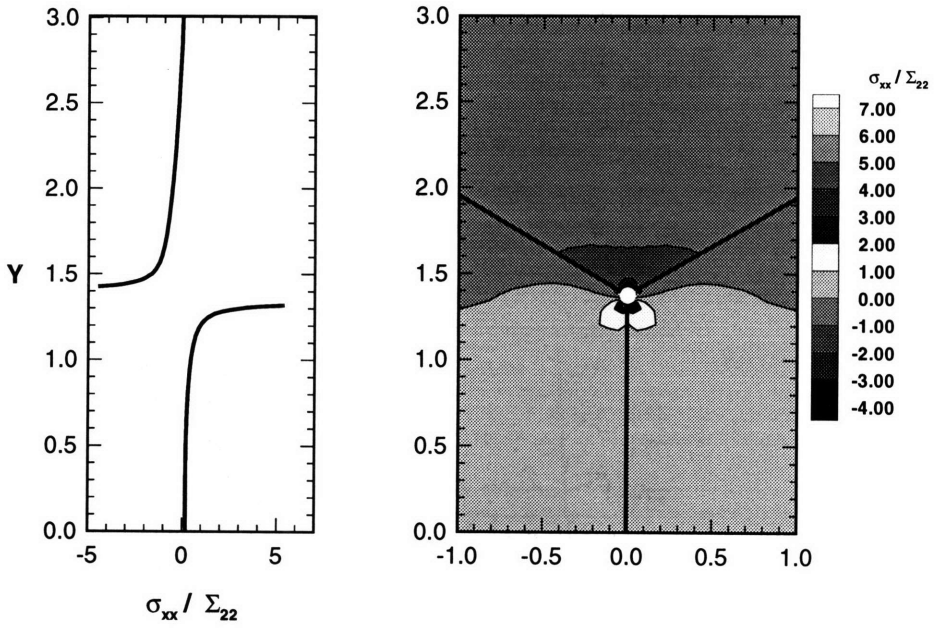

Fig. 2-5a

The above discussion is reinforced by considering the distribution of the stress component σ_{11} in the vicinity of the triple point. The stress component σ_{11} is considered because it provides Mode I loading on a grain boundary crack. This stress component is normalized by the far field loading, Σ_{22}. The grain orientations $\zeta_B = -\zeta_C = 150°$ and $\zeta_A = 0°$ are considered. Contour plots of

[5]The isotropic micro fracture toughness for ice is taken as $K_{ic} = 40kPa\sqrt{m}$ based on the surface energy reported in Ketcham and Hobbs (1969) and a homogenized Young's modulus of $E = 9.5GPa$; the bubble diameter, $\phi = 0.1mm$ consistent with observations in Currier and Schulson (1982).

the normalized σ_{11}/Σ_{22} are shown in Fig. 2-5. The variations of σ_{11}/Σ_{22} along the line $x = 0$ are also shown. In Fig. 2-5a and 2-5c free grain boundary sliding is permitted ($\chi = 0$). In Fig. 2-5b and 2-5d no grain boundary sliding is permitted ($\chi = 1$). In Fig. 2-5c and 2-5d a microcrack emanates from the hole; the microcrack length normalized by the facet length is $l/a = 0.196$.

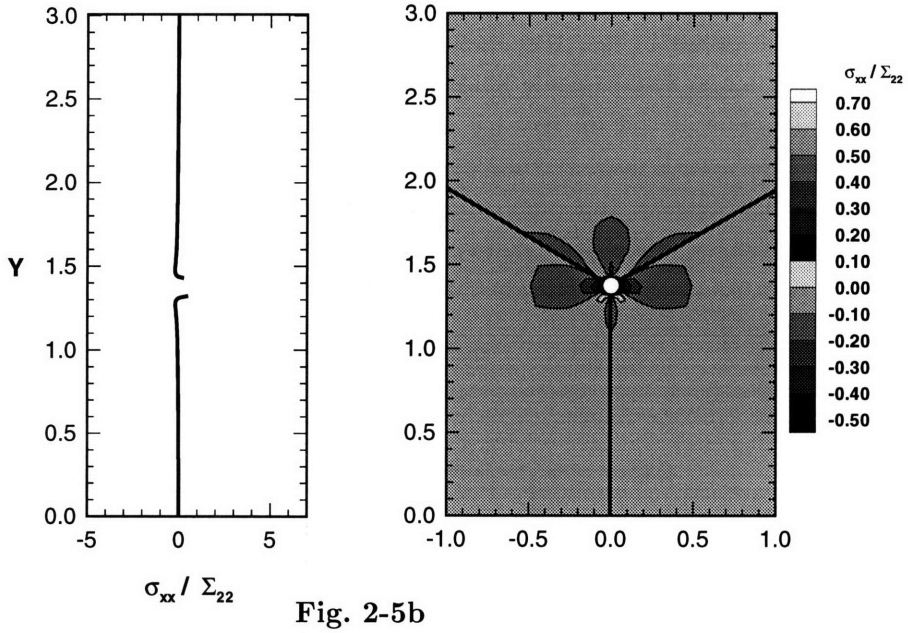

Fig. 2-5b

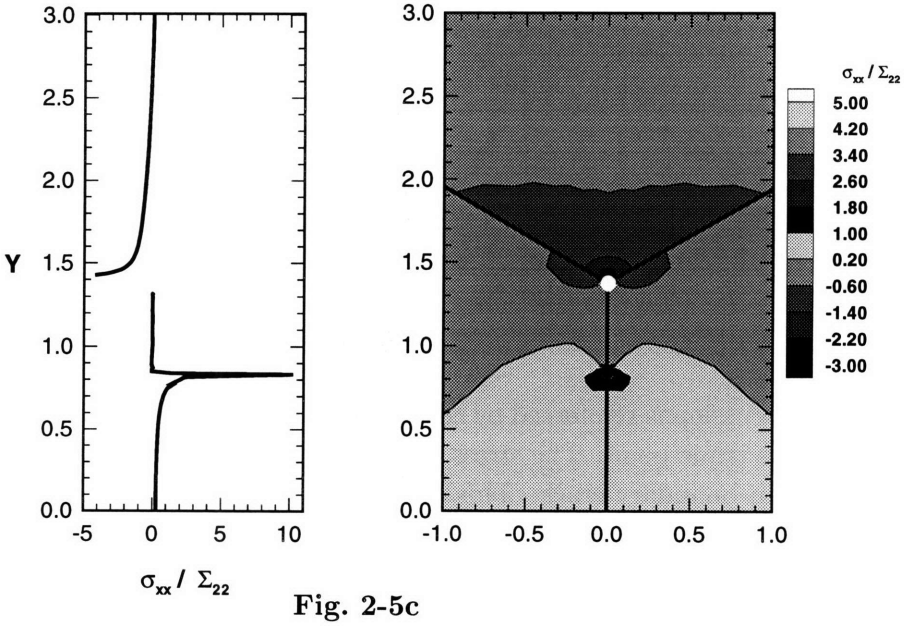

Fig. 2-5c

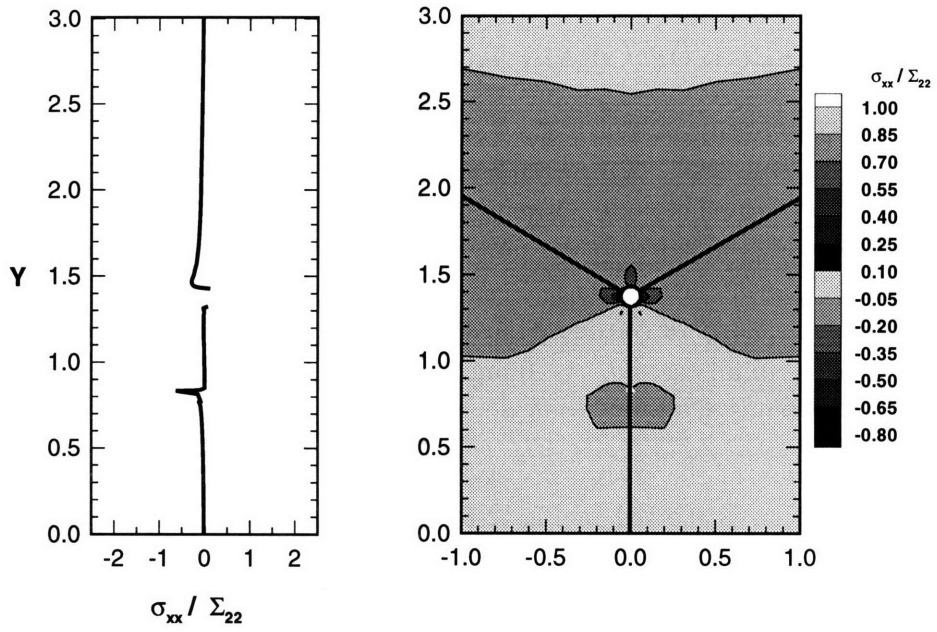

Fig. 2-5d

Figure 2-5: Variation of σ_{11}/Σ_{22} in the vicinity of a triple point, $d = 5mm$, $\zeta = 150°$:
(a) Grain boundary sliding permitted and no microcrack present;
(b) No grain boundary sliding permitted and no microcrack present;
(c) Grain boundary sliding permitted and a microcrack is present;
(d) No grain boundary sliding permitted and a microcrack is present.

Figure 2-5 shows that by allowing grain boundary sliding, the stress is concentrated by the hole to a much greater extent than when no sliding is allowed. The grain boundary sliding mechanism causes a wedging action; at a triple point, one grain is in compression, while the other two are wedged apart and hence are in tension. This tension persists over the entire grain boundary when sliding is allowed. On the other hand, with no grain boundary sliding, σ_{11} soon falls to zero.

It is important to note that the effect of the hole is local. If a microcrack is present when grain boundary sliding is allowed (Fig. 2-5c), the tensile stress along the grain boundary ensures that the crack is *open*. Hence the singularity at the crack tip is positive. In the no sliding case, a small but compressive local σ_{11} stress retards microcrack extension to a point where no crack growth is possible. The crack in Fig. 2-5d is longer than that physically possible for the grain orientations considered. Hence there is a *negative* stress raiser at the crack tip. From Fig. 2-5c and 2-5d it can be concluded that: (1) microcrack formation and growth does not relieve the tensile stresses within the grains ahead of the crack tip when grain boundary sliding is allowed; and (2) when no grain boundary sliding is permitted, the effect of a local stress concentrator is relieved by formation of a *short* microcrack. The length of the microcrack is dependent on the grain anisotropy.

These simulations are further proof (confer Gupta *et al.* (1993)) that the elastic anisotropy mechanism acting alone is not strong enough to cause realistic microcracks in polycrystalline ice.

Hence in all subsequent simulations, gain boundary sliding is allowed.

2.5.2 Effect of Grain Anisotropy

The effect of grain anisotropy on microcracking is studied by varying the orientation of the grain's orthotropic axis, ζ, with respect to a fixed global reference frame, and with respect to neighboring grains. The unit cell model described above allows arbitrary variation in orientation of all three grains making up the unit cell. In this section, attention is focused on a symmetric distribution of grain orientations: $\zeta_A = 0$ and $\zeta_B = -\zeta_C = \zeta$. The influence of random grain orientations, $\zeta_A, \zeta_B, \zeta_C$ is considered in a subsequent section. Due to the symmetry of the boundary value problem, in all cases $J_y = 0$ and $J_x \neq 0$. Thus from Eq. (2.18) $\beta = 0$, $\mathcal{G} = J_x$ and the microcrack extends along the grain boundary.

The variation of the energy released J_x, as the microcrack grows under constant uniaxial far field compression is plotted in Fig. 2-6a. The whole range of grain orientations is considered: $0° \leq \zeta \leq 180°$. The microcrack length, l, is normalized by the facet length, a. The detail of Fig. 2-6a, when the microcracks are short compared with the bubble radius, is plotted in Fig. 2-6b. Figures 2-6a and 2-6b show that there are regions of stable and unstable crack growth; a positive slope implies unstable crack growth while a negative slope corresponds to stable crack extension.

The defects located on the bubble surface release very little energy as they extend. This implies that they require a large far field compressive stress to nucleate. Once the nucleation stress is reached however, the defects grow unstably past the energy release peak into the stable regions, *i.e.* the region with a negative slope in Fig. 2-6b. This is the 'pop-in' length, also present in isotropic homogeneous materials as discussed in Sammis and Ashby (1986). The microcrack length increases with applied far field compression in a stable manner until the energy well is reached at approximately $l/a = 0.5$ (see Fig. 2-6a). At this point the microcrack becomes unstable once again (the slope is positive), and grows to the neighboring triple point. Beyond this point, the direction in which the microcrack extends is dictated by the energy release criterion, Eq. (2.18), and is beyond the scope of this chapter.

A different way to represent the stable and unstable crack growth is to plot the far field compressive stress required to propagate the microcrack, versus the normalized crack length, as done in Fig. 2-7. Equation (2.20) gives the nucleation stress corresponding to the released energy J_x. Figure 2-7 shows that a minimum of $1.4 - 1.7MPa$ has to be applied for the microcrack to extend unstably to the full facet length. Kalifa *et al.* (1989) reports tests at $-10°C$ on isotropic equiaxed granular ice with $d = 5mm$ [6] and reports the occurrence of the first microcrack at an uniaxial compressive stress range of $2.36 - 2.99MPa$. The stress range predicted is lower than observed experimentally due to the difference in the type of ice modeled and tested and due to the assumption of no shear stress transfer across grain boundaries. A more realistic assumption would be a

[6] The grain size computed in Kalifa *et al.* (1989) is based on a uniform sphere assumption and not on an equivalent area of a circle as in this chapter. If the grain size used in the simulations, is computed in the same manner as in the experiment, the new stress range is: $1.55 - 1.9MPa$.

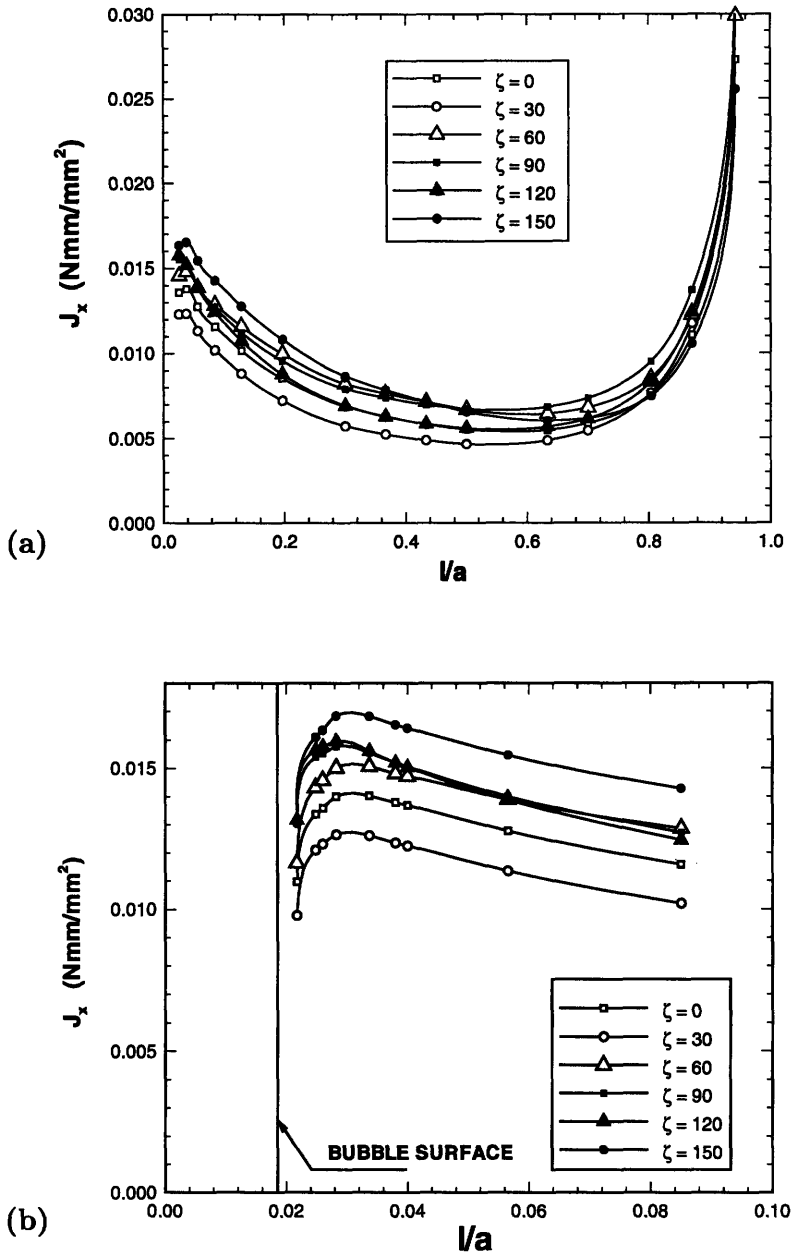

Figure 2-6: (a) Variation of energy released, J_x, with normalized microcrack length for various grain orientations. (b) Variation of energy released, J_x, for short normalized microcrack lengths and for various grain orientations.

visco-elastic response of the grain boundary.

Since the minimum stress occurs at approximately $l/a \approx 0.5$ and shorter cracks are stable, [7] the origin of the defect is not critical. Here the original defect is assumed to be a surface flaw on the bubble, but can equally well be a decohered region on the grain boundary observed experimentally in Picu and Gupta (1994).

[7]Provided the microcrack is longer than the 'pop-in' length.

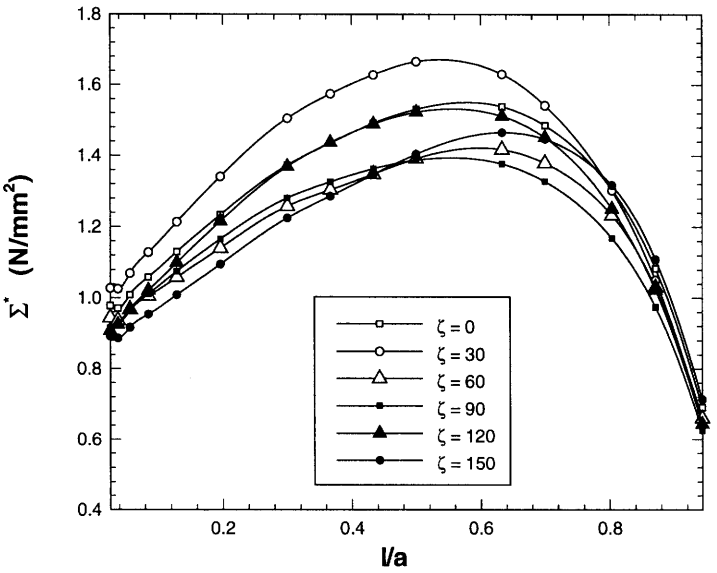

Figure 2-7: Variation of applied compressive stress, Σ^* with normalized microcrack lengths for various grain orientations.

Figures 2-6a, 2-6b, and 2-7 show the effect of grain orientation on microcracking. In addition the variation of J_x with ζ is plotted in Fig. 2-8 for three different crack lengths. From these figures it is evident that grain anisotropy does not alter the nature of microcrack growth. The anisotropy does effect the length at which the microcrack becomes unstable, *i.e.* the position of the minimum in the energy J_x, and creates a band of stresses (or a band of J_x) which can cause microcrack growth. The maximum band width is 41% of the mean J_x and 21% of the mean stress required for microcrack growth. The mean values are taken at the point where the bands are maximum. It can be concluded that for a symmetric distribution of grain orientations within the unit cell, the anisotropy of the grains does not have a strong effect on the applied uniaxial compressive stress required to nucleate and propagate the microcrack. The effect of choosing the three grains' orientation randomly is considered below.

2.5.3 Biaxial Compression

It has been established experimentally that in polycrystalline ice the stresses causing microcracking, and subsequent failure, increase with increasing confinement (see for *e.g.* Kalifa *et al.* (1989), Smith and Schulson (1993)). The effect of applying a biaxial compressive far field stress on microcracking is investigated by varying the confinement ratio, $\lambda = \Sigma_{11}/\Sigma_{22}$. The corresponding traction boundary conditions are given by Eq. (2.6) with $\alpha = 0$. The influence of elastic anisotropy is also investigated. To limit the number of cases, only symmetric grain orientations are considered.

The energy released, J_x is plotted against the normalized crack length, l/a for different amounts of confinement ratio, λ, in Fig. 2-9a. The far field compressive stress is kept constant at $10MPa$. To convert to the microcracking stress, Σ^*, Eq. (2.20) is employed. Figure 2-9b shows the corresponding average far field compressive stress, Σ^*. Varying the grain orientations produces a band of possible

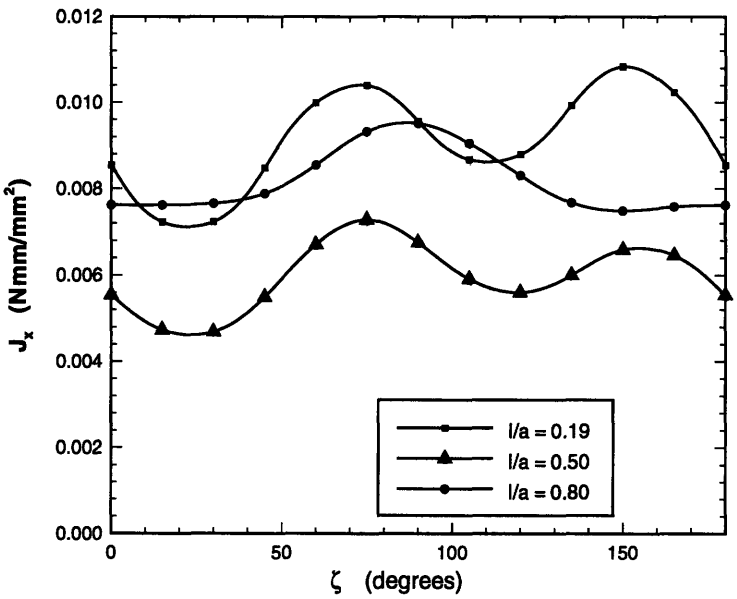

Figure 2-8: Variation of energy released, J_x, with grain orientation, ζ, for various normalized microcrack lengths.

values. These bands are demarcated by error bars; to avoid confusion, only the bands for $\lambda = 0$ and 0.2 are shown in Fig. 2-9. The results for biaxial compression are qualitatively similar to the uniaxial case ($\lambda = 0$). All the curves exhibit a peak, or a critical stress beyond which the microcrack propagates unstably to the neighboring triple point. The effect of grain orientation is much more pronounced for the higher confinement cases where larger stresses are required to grow the microcrack. For example, when $\lambda = 0.2$ the maximum band width is 115% of the average stress.

Simulations indicate that when the confinement ratio is greater than $\lambda = 0.2$, facet length microcracks do not form. As an example, Fig. 2-9 shows that for confinement ratio $\lambda = 0.3$, the maximum normalized microcrack length that can be realized is $l/a = 0.3$. This point is marked with X in Fig. 2-9. Increasing the far field load will not increases the microcrack length. If the crack is artificially lengthened the finite element solution predicts that the crack faces interpenetrate–something which is impossible in reality. Increasing the confinement further, shortens the maximum possible microcrack length. Smith and Schulson (1993) observed that above approximately $\lambda \approx 0.2$ the failure mode of $S2$ ice at $-10°C$ changes from in plane to being fully three dimensional. Further Smith and Schulson (1993) note that the microcracks above and below the transitional confinement had different characteristics. The simulated results are in accord with these observations for low confinement ratios; due to the assumption of planar conditions, however, the present model cannot capture the microcrack behavior at the higher confinement ratios.

2.5.4 Effect of Retarded Grain Boundary Sliding

Thus far the idealized case of free grain boundary sliding was assumed. This section investigates the effect of retarding grain boundary slip by considering the boundary as an elastic layer. This

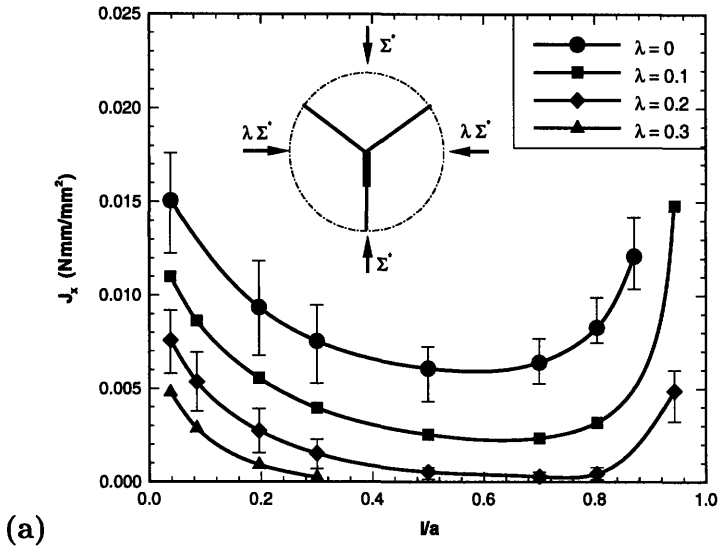

(a)

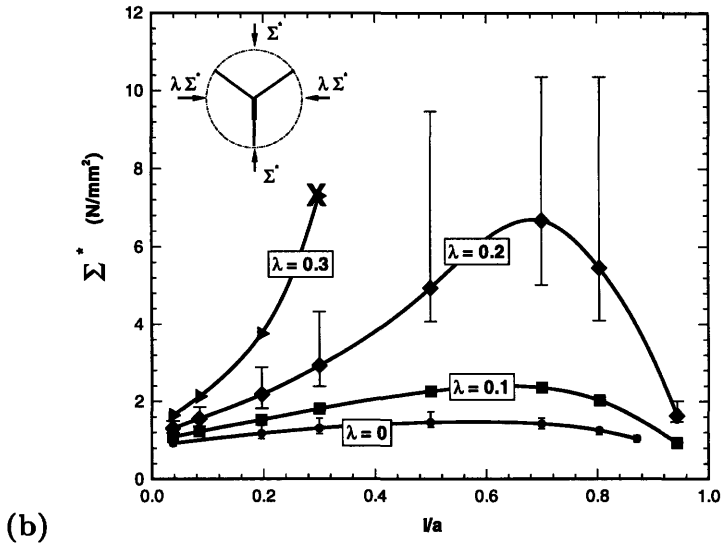

(b)

Figure 2-9: (a) Variation of energy released J_x, with normalized microcrack length l/a, and increasing confinement ratios, $\lambda = \Sigma_{11}/\Sigma_{22}$. (b) Far field compressive stress, Σ^*, versus normalized microcrack length l/a, for increasing confinement ratios, λ.

layer is modeled by discrete shear springs as described in Section 2.3.2. As the grain boundary is assigned greater stiffness (higher s in Eq. (2.14)) so grain sliding is retarded, and hence the grain boundary can transfer greater amounts of shear stress. Temperature is expected to have a strong effect on the stiffness of the grain boundary zone; simulations run with stiffer boundaries correspond to experiments conducted at lower temperatures. Unfortunately, there is no *direct* experimental data on the relationship between grain boundary stiffness and temperature. For this reason, a range of stiffnesses are considered here.

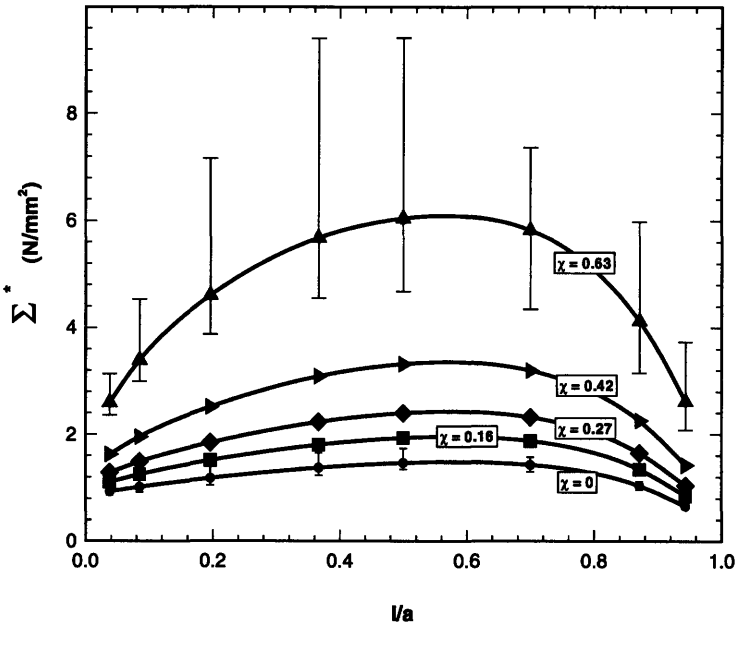

(a)

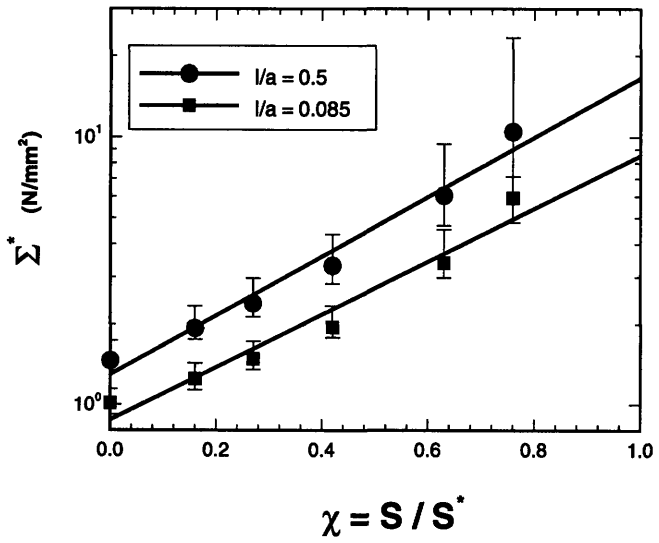

(b)

Figure 2-10: (a) Far field compressive stress, Σ^*, versus normalized microcrack length l/a, for increasing fraction of shear transfer, χ. (b) Far field compressive stress, Σ^*, versus the fraction of shear transfer, χ, for two normalized microcrack lengths l/a.

Figure 2-10a shows the variation of microcracking stress with the normalized crack length and with various fractions of shear transfer, χ. Bands due to the effect of grain anisotropy on Σ^* are also shown for the free slip case, $\chi = 0$ and for $\chi = 0.63$. Only symmetric distributions of grain orientations are considered. The curves for the different fractions of shear transfer all have the

same shape; microcracking is stable at first and when the crack reaches a critical length, unstable propagation to the neighboring triple point ensues. As expected, the microcracking stress increases as χ increases. In Fig. 2-10b, Σ^* versus χ is plotted as points on semi-log axes for crack lengths of $l/a = 0.085$ and 0.5. In addition, linear least square fits of the data are also plotted; the coefficients of correlation are 0.98 and 0.99 for $l/a = 0.085$ and 0.5 curves, respectively. Thus, the rate at which Σ^* increases with the fraction of shear transfer, χ, for a given microcrack length is approximately exponential.

The above results suggest that if the grain boundary shear stiffness is linearly related to temperature, and if the boundary fracture surface energy remains approximately constant with temperature (as assumed here), then the microcracking stress increases approximately exponentially with decreasing temperature. There is some experimental evidence of the former condition. Gold (1958) measured the Young's modulus of single and polycrystal $S2$ ice under static, but short duration, loading in the $-3° \geq T \geq -40°$C range. The experimental data shows that single crystal Young's modulus is independent of temperature in this range (consistent with the empirical Eq. (1.2)). For polycrystal $S2$ ice, however, an approximately linear relationship between Young's modulus and temperature was observed in the same temperature range. Gold (1958) ascribed this temperature dependence to grain boundary slip.

When grain boundary slip is retarded to such an extent that $\chi \geq 0.93$, facet length microcracks are not realizable, no matter what far field compressive stress is applied. This observation is consistent with the no grain boundary slip condition ($\chi = 1$). It has already been shown that when $\chi = 1$ the elastic mismatch between neighboring ice grains is not strong enough to cause facet length cracks.

2.5.5 Effect of Microstructural Parameters

Effect of Random Grain Anisotropy

The grain anisotropy in the global axes system depends on the orientation of the grain, ζ, and is given by Eqs (2.3) and (2.4). The three grains in the unit cell model can have any orientations. Here, the grain orientations are assigned randomly in the range $0° \leq \zeta \leq 180°$, using a random number generator with different starting seeds. Sixty microcracking simulations were performed, all with different and random sets of ζ. The orientations of grains A, B, and C in the simulations are shown in Fig. 2-11a. Note that the symmetric distributions are also included. These simulations are by no means exhaustive, however, they provide a good indication of the effect of random grain orientations on microcracking.

Due to a lack of symmetry of the grain orientations in the unit cell, $J_x \neq 0$ and $J_y \neq 0$. This however, does not automatically imply that trans-granular cracking will occur. The grain boundary surface fracture energy γ_{gb} is less than the grain's surface energy γ_{sv}. The condition for

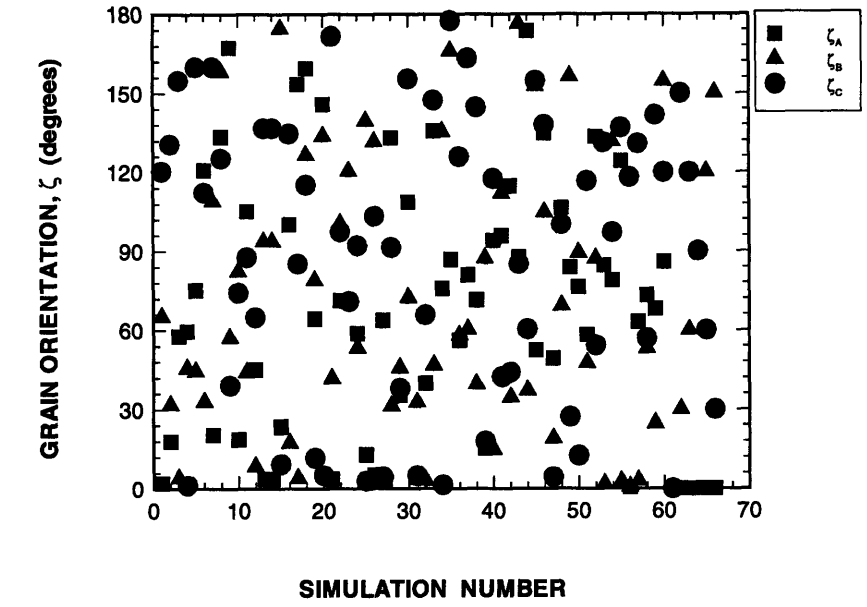

(a)

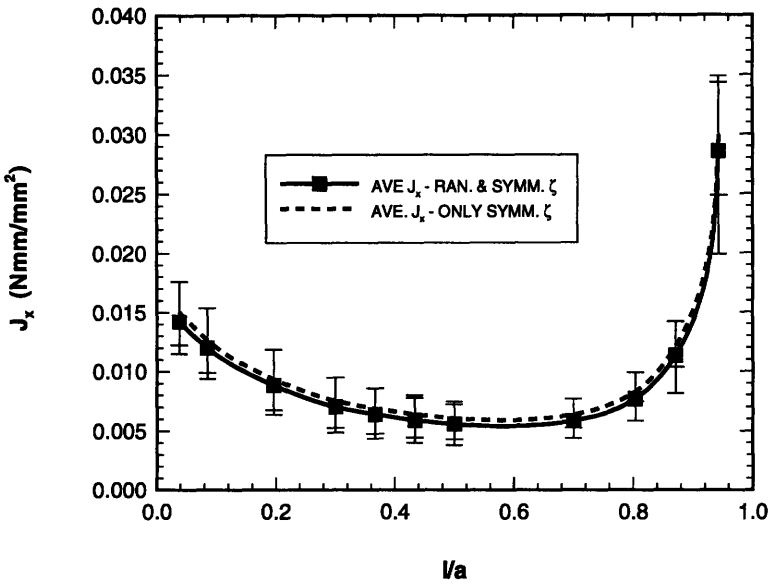

(b)

Figure 2-11: (a) Distribution of grain orientations, ζ, used in the simulations. (b) Variation of energy released J_x, with normalized microcrack length l/a, for random and symmetric ζ distributions, and only symmetric ζ distributions.

the microcrack to leave the grain boundary is:

$$\frac{\mathcal{G}_{max}}{J_x} > \frac{\gamma_{sv}}{\gamma_{gb}} \tag{2.23}$$

where $\mathcal{G}_{max}$ is determined from Eq. (2.18) with $\beta = \tan^{-1}(J_y/J_x)$. For all the simulations conducted in this section, the elastic anisotropy in the ice crystals was not strong enough to satisfy the inequality in Eq. (2.23). Hence the microcracks remained on the grain boundary.

The variation of the energy released J_x or $\mathcal{G}(\beta = 0)$, under constant far field compression ($\Sigma_{22} = 10MPa$), versus the normalized microcrack length is plotted in Fig. 2-11b. The solid line corresponds to the average energy released for all grain orientations considered, *i.e.* both random and symmetric ζ; the dashed line is the average energy when the orientations are symmetric. The error bars indicate the width of the band produced by varying the grain orientations. From Fig. 2-11b it can be seen that the effect of varying the grain orientations randomly is to decrease the average energy released slightly from the symmetric orientations case; the maximum difference between the two average J_x is 9%. The same conclusion can be reached for random ζ as for symmetric ζ. Namely, the microcrack grows stably at first (decreasing $\mathcal{G}$ under constant far field loading), reaches a critical length, and then propagates unstably (increasing $\mathcal{G}$ under constant load). Also, random anisotropy of the grains does not have a strong effect on the applied uniaxial compressive stresses required to nucleate and propagate the microcrack. Since the random and symmetric ζ bands are similar in width, a measure of the effect of grain anisotropy is given by a symmetric ζ distribution.

Effect of Grain Size

The influence of grain size on the compressive stress required to nucleate and propagate a microcrack is studied in this section. The grain size, d, is varied in the range typically observed in polycrystalline $S2$ ice: $1mm \leq d \leq 10mm$. In addition, the effect of the grain orientation, ζ, is also considered. The bubble diameter, ϕ, is scaled linearly with grain size, from $\phi = 0.1mm$ for $d = 5mm$.

The variation of the energy released, J_x, with microcrack length is plotted in Fig. 2-12 for three different grain sizes. The curve is drawn through the mean values of J_x; error bars indicate the width of the band produced by varying the grain orientations, ζ. From Fig. 2-12 it can be seen that the trends in J_x remain the same for different grain sizes. Although Fig. 2-12 shows that for fine grained samples, J_x varies very little with crack length, the applied compressive stress is inversely related to J_x (Eq. 2.20). Hence the variation in stress with microcrack length is not negligible, for all grain sizes. Also, as the grain size decreases so the amount of energy released, J_x, also decreases. Thus, the compressive stress required to propagate the crack increases as the grain size decreases.

Figure 2-13 shows the stress required to lengthen the microcrack as a function of grain size for different crack lengths. The microcracking stress is proportional to $d^{-0.5}$.

The effect of grain anisotropy remains the same for polycrystalline ice of different grain sizes. The maximum band width is 41% of the mean J_x irrespective of d. Although this percentage is fixed, the magnitude of the variation in the far field stress is much larger for smaller grain sizes where the microcracking stress is large (see Fig. 2-13). Hence the grain anisotropy should produce more measurable scatter in microcracking stress as the polycrystal becomes fine grained.

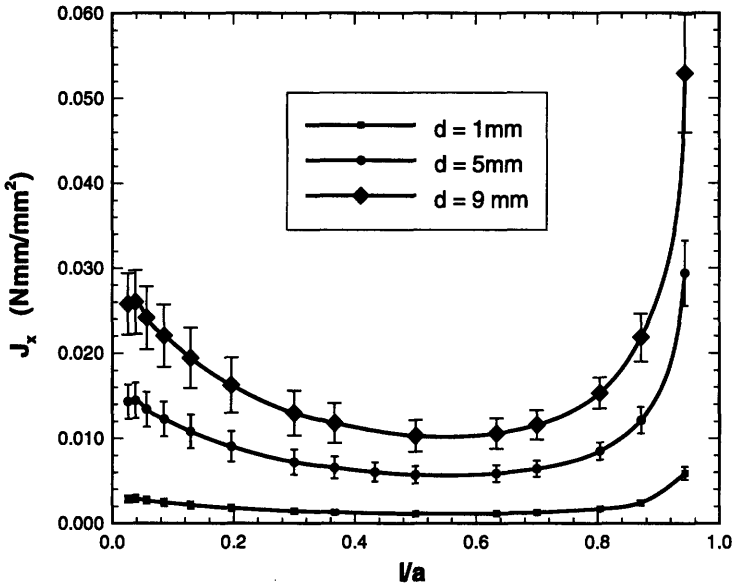

Figure 2-12: Variation of energy released, J_x, with normalized microcrack length, l/a, for various grain sizes.

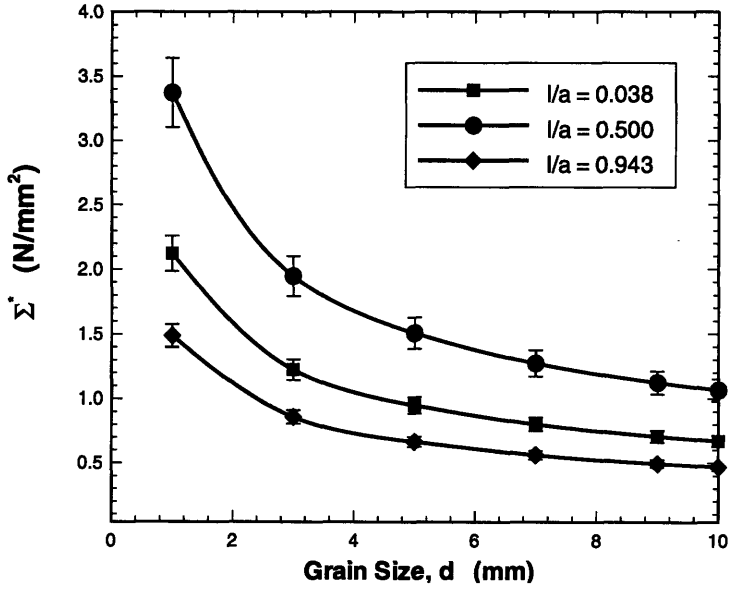

Figure 2-13: Far field compressive stress, Σ^* required to extend a microcrack of varying length versus grain size, d.

The above discussion suggests that in real polycrystal samples, loaded at sufficiently fast rates to ensure linear stress- strain response, there should exist two population of microcracks. The first group of microcracks have lengths in the range $0.1 \leq l/a \leq 0.5$. The second group have lengths equal to, or longer than the grain facet lengths. Cannon *et al.* (1990) and Schulson *et al.* (1991) report experimental evidence of stable microcrack extension until a critical length is reached, at

which point the microcrack growth becomes unstable. Although a normalized microcrack length is reported, the normalizing length is not the facet length. Further, due to the relative coarseness of the grains compared to the specimen size, no conclusion can be reached as to the fraction of the facet length at which the microcracks became unstable.

Effect of Grain Shape

The angles between grain boundaries meeting at a triple point in naturally occurring ice are seldom the same. This section considers the effect of varying θ, the angle of the wedging grain A (see Fig. 2-2) on microcracking, when uniaxial far field loading is applied. In addition, the grain orientations are symmetric.

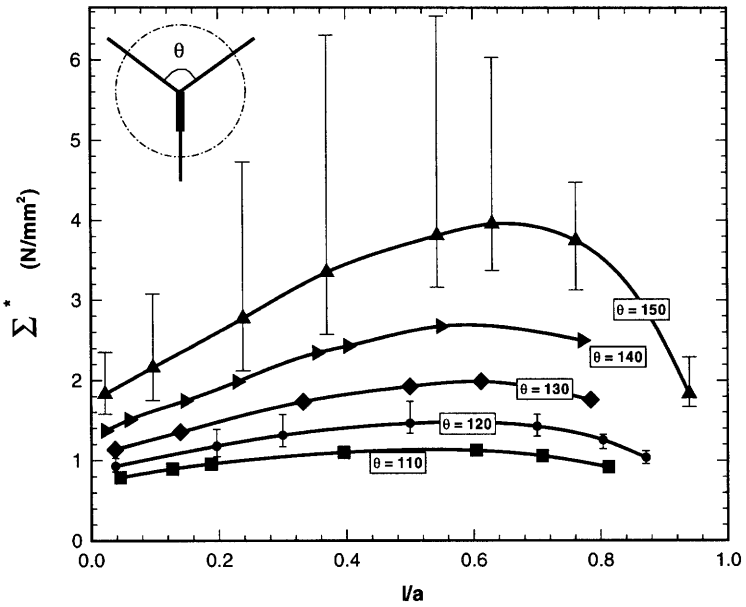

Figure 2-14: Far field compressive stress, Σ^*, versus normalized microcrack length l/a, for different grain shapes, θ.

Figure 2-14 shows the compressive stress required to nucleate and lengthen the grain boundary crack for five grain shapes. The microcrack length is normalized by the facet containing the microcrack; this facet length is a function of θ. The average stresses are plotted, together with the bands resulting from varying the grain orientations for $\theta = 150°$ and $\theta = 110°$. From Fig. 2-14 it can be seen that all the curves show similar behavior: the microcrack grows stably at first requiring an increasing far field compression, reaches a critical length and then propagates unstably. As the wedging grain becomes "blunter" (increasing θ) so the required far field compression increases. The average stress required for unstable crack propagation has to increase 3.5 times if the grain's θ increases from 110° to 150°. Note also that for grains with large θ, much larger increments in applied stress are required to extend the microcrack.

The effect of grain anisotropy becomes significant as the grain angle θ increases. For "sharp" grains ($\theta = 110°$) Fig. 2-14 shows that grain anisotropy plays a minor role; for the "blunt" grains ($\theta = 150°$) however, the grain anisotropy can raise the average microcracking stress almost 90%.

This discussion suggests that if grain boundary sliding is indeed a mechanism that operates at the higher strain rates, then in a polycrystalline ice sample the "sharpest" grains (those with the smallest θ) will nucleate and propagate microcracks first. As the loading increases, "blunter" grains will begin to wedge their neighbors apart. Sufficiently "blunt" grains will produce either no cracks or only partly cracked facets.

Effect of Loading Direction

In a polycrystalline ice specimen, the loading axis does not always coincide with the microcrack. The effect of rotating the uniaxial far field compressive stress with respect to the axis of the microcrack by α, is investigated in this section. The corresponding traction boundary conditions are given by Eq. (2.6) with $\lambda = 0$. Once again, only symmetrical distributions of grain orientations are considered. Thus rotating the far field stress by α or $-\alpha$ produces identical results.

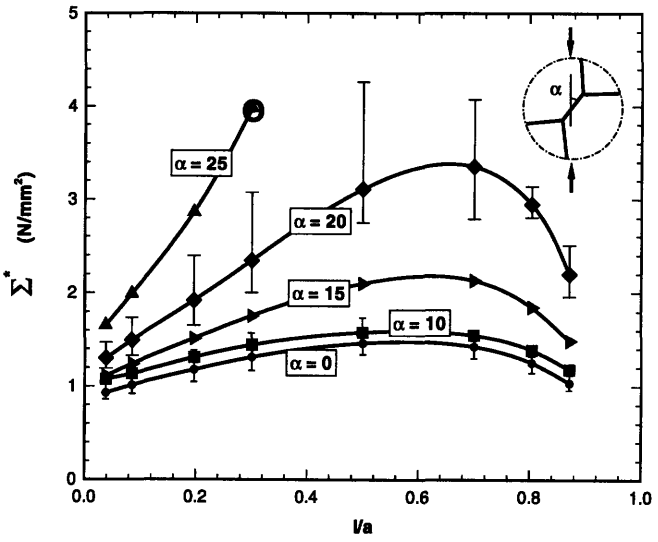

Figure 2-15: Far field compressive stress, Σ^*, versus normalized microcrack length l/a, for different orientations of microcrack with respect to loading axis, α.

Figure 2-15 shows the variation of the average stress required to nucleate and grow the microcrack with normalized crack length and with the angle between the load and the microcrack, α. The bands produced by considering the grain orientations are shown for $\alpha = 0°$ and $\alpha = 20°$. The curves shown in Fig. 2-15 are characteristic of microcracking due to grain boundary sliding. As the uniaxial loading is rotated away from the microcrack (increasing α), the stress required to propagate the microcrack increases. The rate at which the applied stress increases in order to maintain crack growth increases with α.

The boundary value problem is non symmetric for all $\alpha \neq 0$. Hence the microcrack can extend into the crystal if Eq. (2.23) is satisfied. The simulations show that as α increase so the tendency for the microcrack to leave the grain boundary also increases. Finally, at $\alpha = 25°$ the microcrack leaves the grain boundary, and the simulation is stopped; this point is marked by O in Fig. 2-15. These simulations predict that microcracking is possible in the range $-25° \leq \alpha \leq 25°$ to the loading axis; if the grain boundary lies in this range, then the microcrack will extend along the boundary, if outside this range then the microcracking will be trans-granular.

It is well known that microcracks tend to align with the axis of loading under far field compression (see *e.g.* Smith and Schulson (1993), Hallam *et al.* (1987) and Kalifa *et al.* (1989)). Hallam *et al.* (1987) reports the angular distribution of the microcracks to be approximately normal with mean $-3.5°$ and a standard deviation of $23.3°$. This reference also reports that the proportion of inter- and trans- granular microcracks was about the same. Although the simulation results agree with these experimental observations, it is important to make two notes. First Hallam *et al.* experimented on isotropic equiaxed polycrystalline ice. Second, although the loading was applied statically and time was allowed to elapse between loading increments, Hallam *et al.* (1987) reports that almost all the cracking activity occurred in the first few loading increments where creep effects were small.

2.6 Conclusion

This chapter examines the grain boundary sliding mechanism, as a possible cause of microcracking at moderately high rate of quasi- static uniaxial compression where the response of the polycrystal is almost linear. Results show that without allowing relative motion of the grains along the grain boundary, unrealisticly high stresses are required to nucleate and propagate a microcrack; in addition the resulting microcracks are much shorter than those observed experimentally. If grain boundary sliding is allowed, the stresses required to nucleate and propagate a grain boundary microcrack become more realistic. If free grain boundary slip is assumed, the stresses are under predicted.

The following salient conclusions have been drawn from the simulations:

1. After an initial 'pop- in', microcrack growth is stable, requiring an increase in the far field compression to extend the crack. When the microcrack reaches a critical length, (approximately half the facet length) it propagates unstably to the neighboring triple point.
2. Increasing the confinement ratio, increases the required microcracking stress. For confinement ratio greater than 0.2, and under plane stress conditions with free grain boundary slip, full facet length cracks cannot occur, no matter what far field compression is applied.
3. As the grain boundary sliding is retarded, so the microcracking stress increases approximately exponentially. It is expected that sliding would be retarded by lowering the temperature. Facet length microcracks will not nucleate for shear transfer ratios of 0.93 and greater.
4. Varying the grain orientations produces a band of possible microcracking stresses. The effect of grain anisotropy is most pronounced when microcracking is inhibited, *i.e.* the required

microcracking stresses are high.

5. The bands of energy released, J_x, produced by symmetric and by random distributions of grain orientations within the unit cell, are similar in width. The maximum band width is approximately 21% of the mean stress.
6. The stress required to extend the microcrack a fixed fraction of the facet length is inversely proportional to the square root of the grain size.
7. In a polycrystal sample, "sharper" wedging grains nucleate microcracks at lower stresses than "blunt" grains.
8. Microcracking is possible only in a 25° range to either side of the compressive axis.

The analyses imply that two populations of microcrack lengths should exist: (i) microcracks which are shorter than a fraction of the facet length, and (ii) microcracks which extend at least over the entire facet length. Modeling the grain boundary as a visco-elastic region warrants further investigation.

REFERENCES

[1] Barnes, P., Tabor, D. and Walker, J.C.F., (1971), The Friction and Creep of Polycrystalline Ice, *Proceedings of the Royal Society of London A*, Vol. 324, pp. 127- 155.

[2] Budiansky, B., and Rice, J.R., (1973), Conservation Laws and Energy-Release Rates, *Journal of Applied Mechanics*, Vol. 40, pp. 201-203.

[3] Cannon, N.P., Schulson, E.M., Smith, T.R. and Frost, H.J., (1990), Wing Cracks and Brittle Compressive Fracture, *Acta Metallurgica et Materialia*, Vol. 38, pp. 1955- 1962.

[4] Carte,A.E., (1961), Air Bubbles in Ice, *Proc. Phys. Soc.*, Vol. 77, pp. 757- 768.

[5] Chatterjee, A.K. and Jellinek, H.H.G. , (1971), Calculation of Grain Boundary Thickness in Polycrystalline Ice of Low Salinity, *Journal of Glaciology*, Vol. 10, pp. 293- 297.

[6] Currier, J.H. and Schulson, E.M., (1982), The Tensile Strength of Ice As a Function of Grain Size, *Acta Metallurgica*, Vol. 30, pp. 1511- 1514.

[7] Cole, D.M., (1988), Crack Nucleation in Polycrystalline Ice, *Cold Regions Science and Technology*, Vol. 15, pp. 79- 87.

[8] Gold, L.W., (1972), The Process of Failure of Columnar- Grained Ice, *Philosophical Magazine A*, Vol. 26, pp. 311-328.

[9] Gold, L.W. and Traetteberg, A. , (1974), Young's Modulus of Ice and Ice Engineering Problems, *Proc., 2nd Symp. on Application of Solid Mechanics*, Dep. Mech. Eng., McMaster Univ., Hamilton, pp. 1- 15.

[10] Gupta, V., Picu, R.C. and Frost, H.J., (1993), Crack Nucleation Mechanism in Saline Ice, *Ice Mechanics*, ASME, AMD, Vol. 163, pp. 199-216.

[11] Hallam, S.D., Duval, P., and Ashby, M.F., (1987), A Study in Polycrystalline Ice Under Uniaxial Compression, *Journal de Physique*, Vol. 48, pp. C1-303- C1-311.

[12] Hobbs, P.V., (1974), *Ice Physics*, Claredon Press, Oxford.

[13] Hussain, M.A., Pu, S.L. and Underwood, J., (1974). *Fracture Analysis, ASTM STP 560*, American Society for Testing and Materials, pp. 2-28.

[14] Kalifa, P., Duval, P. and Ricard, M., (1989), Crack Nucleation in Polycrystalline Ice Under Compressive Stress States, 8th Int. Conf. Offshore Mech. and Arctic Engineering, The Hague, pp. 19-23.

[15] Ketcham, W.M., and Hobbs, P.V., (1969), 'An experimental determination of the surface energies of ice, *Philosophical Magazine A*, Vol. 19, pp. 1161-1173.

[16] Parameswaran, V.R. and Jones, S.J., (1975), Brittle Fracture of Ice at 77K, *Journal of Glaciology*, Vol. 14, pp. 305-315.

[17] V.Z. Parton and E.M. Morozov, (1989), *Mechanics of Elastic- Plastic Fracture*, Second Edition, Hemisphere Publishing Co., Washington.

[18] Picu, R.C. and Gupta, V. , (1994), Observation of Crack Nucleation in Columnar Ice Due to Grain Boundary Sliding, *Submitted for Publication.*

[19] Rice, J.R., (1968), A Path Independent Integral and the Approximate Analysis of Strain Concentration by Notches and Cracks, *Journal of Applied Mechanics*, Vol. 35, pp. 379-386.

[20] Sammis, C.G. and Ashby, M.F., (1986), The Failure of Brittle Porous Solids Under Compressive Stress States, *Acat Metallurgica*, Vol. 34, pp. 511- 526.

[21] Schulson, E.M., (1979), An Analysis of the Brittle to Ductile Transition in Polycrystalline Ice Under Tension, *Cold Regions Science and Technology*, Vol. 1, pp. 87-91.

[22] Schulson, E.M., Kuehn, G.A., Jones, D.E. and Fifolt, D.A., (1991), The Growth of Wing Cracks and the Brittle Compressive Failure of Ice, *Acta Metallurgica et Materialia*, Vol. 39, pp. 2651- 2655.

[23] Shyam Sunder, S. and Wu, M.S., (1990), Crack Nucleation Due to Elastic Anisotropy in Polycrystalline Ice, *Cold Regions Science and Technology*, Vol. 18, pp. 29.

[24] Sinha, N.K., (1982), Delayed Elastic Strain Criterion for First Cracks in Ice, *Proceedings IUTAM Conference, Deformation and Failure of Granular Materials*, ed A.Balkema, pp. 323-330.

[25] Sinha, N.K., (1984), Intercrystalline Cracking, Grain- Boundary Sliding, and Delayed Elasticity At High Temperatures, *Journal of Material Science*, Vol. 19, pp. 359- 376.

[26] Smith, T.R., and Schulson, E.M., (1993), The Brittle Compressive Failure of Fresh-Water Columnar Ice Under Biaxial Loading, *Acta Metallurgica et Materialia*, Vol. 41, pp. 153-163.

[27] Tatibouet, J. , Perez, J. and Vassoille, R., (1987), Study of Grain Boundaries in Ice by Internal Friction Measurement, *Journal de Physique*, Vol. 48, pp. C1-197- C1-203.

[28] Tvergaard, V. and Hutchinson, J.W., (1988), Microcracking in Ceramics Induced by Thermal Expansion or Elastic Anisotropy, *Journal of the American Ceramic Sociecy*, Vol. 71, pp. 157-166.

[29] Zener, C., (1941), Theory of the Elasticity of Polycrystals with Viscous Grain Boundaries, *Physical Review*, Vol. 60, pp. 906- 908.

Chapter 3

NUMBER OF GRAINS REQUIRED TO HOMOGENIZE ELASTIC PROPERTIES OF POLYCRYSTALLINE ICE

ABSTRACT

The number of grains required for homogeneous elastic behavior of polycrystalline $S2$ ice is determined in this chapter. The two extreme cases of (i) no grain boundary slip and (ii) free grain boundary sliding are examined. Detailed finite element simulations of uniaxial loading of specimens containing polygonal grains are performed. The results show that at least 230 grains are required to homogenize the elastic properties. The effect of the grain's elastic anisotropy on the homogenized properties is more important when no grain boundary sliding is allowed; grain shape is more important when grain boundary sliding is permitted. The stress components at the grain centers approximately follow the Gaussian distribution. The average computed homogenized Young's modulus and Poisson ratio at $-16°C$ are: 9.58 GPa and 0.33- with no grain boundary sliding; 7.83 GPa and 0.45- with free grain boundary sliding.

3.1 INTRODUCTION

The homogeneous elastic properties of materials form an integral part of most constitutive theories, and are required in the solution of boundary value problems. In polycrystalline aggregates, crystallographic axes of neighboring grains are seldom aligned in the same direction. Hence there is

a mismatch in elastic properties between neighboring grains in the global axes frame. Theoretical estimates of the elastic constants for polycrystals may be derived from the elastic properties of the constituent monocrystals. The theoretical elastic moduli for polycrystalline ice have been calculated by Michel (1978), Sinha (1989a), and Nanthikesan and Shyam Sunder (1994). These authors used one or more averaging assumptions of Voigt (1910) and Reuss (1929).

The method of Voigt (1910) assumes that all the grains undergo an uniform strain and thus an uniform stress. Thus on the scale of the grain, equilibrium is violated. The method of Reuss (1929), on the other hand, assumes a constant state of stress in all the grains. Thus, although equilibrium is preserved, adjacent grains may have different deformations leading to local violation of compatibility. Hill (1952) showed that the Voigt and Reuss (V-R) methods provide the upper and lower bounds of the elastic stiffness moduli. Other homogenization methods exist to calculate the effective moduli of polycrystals. Among these, for example, are the self consistent and differential methods and the Hashin- Shtrikman bounds; the references for, and details of these and other methods are presented in Nemat- Nasser and Hori (1993). However, the work of Nanthikesan and Shyam Sunder (1994) shows that the *maximum* discrepancy between the V-R bounds on the elastic moduli of columnar grained polycrystalline ice is only 4.2%. These authors conclude that the V-R bounds for polycrystalline ice are so close to each other and to experimental values, that either bound, or an average, can be used as the homogenized elastic moduli.

The fundamental assumptions behind the spatial averaging V-R methods is that the polycrystal contains a sufficient number of grains such that a *continuous* distribution of grain orientations exists. In reality, the number of grains in a polycrystal is finite. The aim of this chapter is to quantify how many grains are required to ensure an elastically homogeneous response of polycrystalline ice. This number of grains specifies the size of the representative element. Two extreme idealized cases are considered: (i) neighboring grains are perfectly bonded to each other, *i.e.*, no relative slip between the grains, and (ii) no shear stress transfer between neighboring grains, *i.e.*, free grain boundary slip. Relative displacement between grains might be due to viscous effects, and/ or due to a compliant grain boundary zone. The idealized case of no grain boundary slip approximates short duration, high loading rate, or high frequency tests. In both cases the grains are assumed to remain elastic.

In this chapter fresh water, columnar grained ice is considered. The $c-axes$ of the individual crystals lie in the horizontal plane (the plane of the ice cover) and are randomly distributed. Hence the ice cover is transversely isotropic. This type of ice is found on lakes, and rivers with low flow velocities. Michel and Ramsier (1971) classified this ice type as $S2$. The nature of $S2$ ice allows for planar modeling of the polycrystalline aggregate. The behavior of ice can be ductile or brittle depending on the loading rate and temperature. The polycrystal deformation in the brittle regime, as well as the peak stresses at the high end of the ductile regime occurs at small strain ($< 1\%$).

In the present study, detailed finite element simulations of uniaxial loading of polycrystalline samples of various sizes are conducted. The grain geometry is modeled by modified Voronoi polygons (see Section 3.2.1). The grain's elastic anisotropy is specified in Section 3.2.2. The finite element model for the ensemble of grains is set up, and the homogenized elastic properties are

defined in Sections 3.2.3 and 3.2.4 respectively. The ice single crystal stiffness moduli, used in the simulations, is reported in Section 3.3. The results from the simulations of: (i) variation of homogenized elastic properties with number of grains, and (ii) the statistical distribution of residual stresses within the grains, are presented and discussed in Section 3.4.

3.2 The Numerical Model

The polycrystalline sample is idealized as an heterogeneous ensemble of randomly oriented, elastically anisotropic grains of random shape but approximately equal area. The two limits of (i) no grain boundary sliding and (ii) free grain boundary sliding are investigated. The primary aim in this study is to determine how many grains are required to ensure that the entire sample behaves isotropically. To this end, simulations of uniaxial loading of samples containing various numbers of grains are performed, and homogenized elastic properties are computed. This section describes how the grain geometry and elastic properties are set up, the computational model, and the method of homogenization.

3.2.1 Modeling The Grain Geometry

A cross section taken through columnar grained $S2$ ice perpendicular to the column axes, reveals grains that are approximately polygonal in shape and equal in area (see Sinha, 1989b for a typical section). The polygons are not regular and the number of facets varies from grain to grain. In the past, the grain geometry has been modeled effectively by Voronoi tessellation (sometimes refered to as Theissen or Dirichlet polygons), see for example Frost and Thompson (1987) who considered different conditions of grain nucleation and growth. In this chapter the grains are represented by modified Voronoi polygons. The details and the motivation for the method by which grain geometry is constructed follows.

Standard Voronoi tessellation begins from a set of nucleation points, p. Next an unique triangulation grid involving the p points is constructed by Delaunay triangulation. Perpendicular bisectors of each side of the triangles are found. The intersections of the perpendicular bisectors form the vertices of the Voronoi polygons. One property of Voronoi polygons is that a point lying anywhere within polygon P_i is closer to the its nucleation point p_i then to any other nucleation point.

Since the grains in a section of $S2$ ice all have approximately the same area (see *e.g.*, Sinha (1989b)) the nucleation points, p, cannot be distributed completely randomly on the pplain. Instead, the points have to be constrained to lie a minimum distance apart, say $2r$; this requirement is met by placing rigid disks of diameter $2r$ *randomly* on the plain with no overlap, until no more will fit. This results in the polygons/ grains having approximately the same area. This process still leads to facet lengths, l_i which are very short compared to the distance from the nucleation point to the polygon vertex, Ve_i, *i.e.*, $Ve_i \gg l_i$. These short facets result in numerical inaccuracies when solving for the stresses and strains within the grains. To obviate these difficulties the facets

with $l_i/Ve_i < 0.3$ are lengthened. The vertices on either end of the short facet are shifted to:

$$\mathbf{V}_j^{NEW} = \mathbf{V}_j^{OLD} \frac{l_i}{Ve_i} \frac{1}{0.3} + \mathbf{c}_j(1 - \frac{l_i}{Ve_i} \frac{1}{0.3}) \tag{3.1}$$

where $\mathbf{V}_j$ is the coordinate of vertex j ($j = 1, 2$), and $\mathbf{c}_j$ is the centroid coordinate of the corresponding triangle.

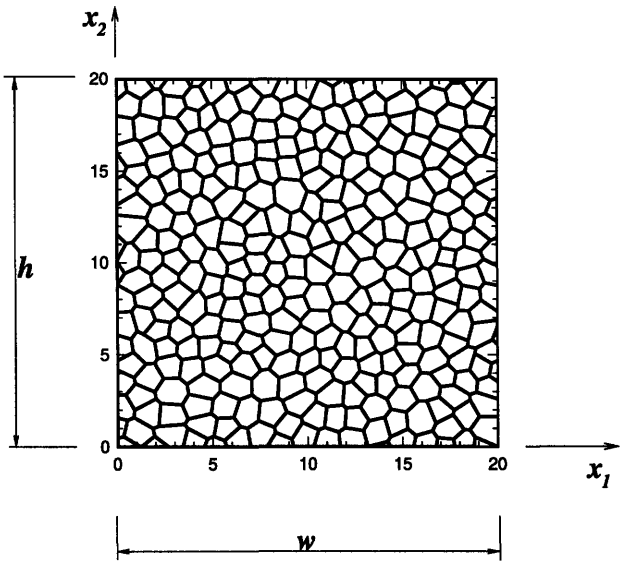

(a)

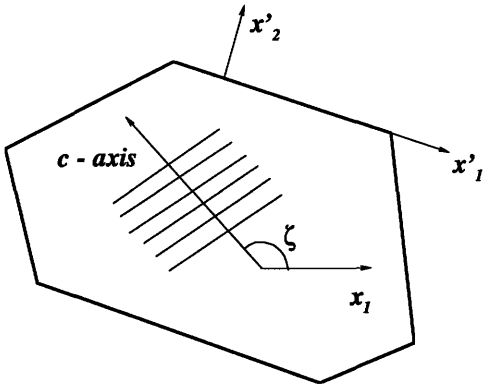

TYPICAL GRAIN

(b)

Figure 3-1: (a) Typical grain geometry of a 20×20 mm^2 sample with 305 grains; (b) Typical grain with orientation ζ.

The specification of a sample size creates grain slivers on the boundaries as well as facets with $l_i/Ve_i < 0.3$; both lead to numerical difficulties. The short facets are removed by shifting the

polygon vertices perpendicularly to the boundary. The grain slivers with nucleation points lying outside a strip of width $2r/2.5$, which surrounds the sample, are removed; the vertices of the neighboring polygons are moved perpendicularly to the boundary. Finally, the nucleation points of the polygons lying on the boundary are shifted to the polygons' geometric centers.

In all subsequent simulations $2r$ is set to 1 mm; thus approximately defining the average grain size. The area is defined only approximately due to the randomness in creating the grain geometry. Figures 3-1a shows a 20×20 mm^2 sample with a typical grain geometry generated by the above process. The corresponding histogram of the grain areas is shown in Fig. 3-2a. The average grain area is 1.31 mm^2. As to be expected most grain areas cluster around the mean. The few grains which are slightly larger and slightly smaller are those found on the boundary. Their area differs from the mean due to the treatment of border grains described above.

3.2.2 The Grain Elastic Properties

Each grain in the polycrystalline aggregate is defined by its crystal orientation, here specified by the $c-axis$. The distribution of the $c-axes$ in a macroscopically homogeneous and isotropic material is random. In the case of transversely isotropic $S2$ ice, the $c-axes$ are randomly distributed in the plane of isotropy. The dynamic elastic stiffness tensor $\mathbf{C}_g^{3D}$ can be taken as constant for all the grains.

Since the overall macro- response of polycrystalline $S2$ ice is transversely isotropic with the plane of isotropy being the plane of interest, the three dimensional $\mathbf{C}_g^{3D}$ can be reduced to plane conditions. Plane stress conditions are assumed since the ice plate thickness is much smaller than the in plane $x_1 - x_2$ dimensions. This assumption modifies the single grain orthotropic stiffness tensor components ${C_g^{3D}}_{ij}$ as follows:

$$
\begin{aligned}
{C_g}_{11} &= {C_g^{3D}}_{11} - \frac{{C_g^{3D}}_{13}\ {C_g^{3D}}_{31}}{{C_g^{3D}}_{33}} & {C_g}_{12} &= {C_g^{3D}}_{12} - \frac{{C_g^{3D}}_{13}\ {C_g^{3D}}_{32}}{{C_g^{3D}}_{33}} \\
{C_g}_{21} &= {C_g^{3D}}_{21} - \frac{{C_g^{3D}}_{23}\ {C_g^{3D}}_{31}}{{C_g^{3D}}_{33}} & {C_g}_{22} &= {C_g^{3D}}_{22} - \frac{{C_g^{3D}}_{23}\ {C_g^{3D}}_{32}}{{C_g^{3D}}_{33}} \\
{C_g}_{33} &= {C_g^{3D}}_{33}
\end{aligned}
\tag{3.2}
$$

In order to obtain the macroscopic behavior of the polycrystal, the components of $\mathbf{C}_g$ have to be determined in the global axes system. The components of $\mathbf{C}_g$ are usually specified in the axes system associated with the crystal lattice. The stiffness components in the global axes system are given by the standard fourth rank tensor transformation. In two dimensions this transformation can be expressed as:

$$\mathbf{C_G} = \mathbf{R}^T \mathbf{C}_g \mathbf{R} \tag{3.3}$$

where $\mathbf{C_G}$ contains the components of the the grain stiffness in the global axes system, T is the

transpose operation, and the transformation tensor $\mathbf{R}$ is given by:

$$\mathbf{R} = \begin{pmatrix} \cos^2(\zeta) & \sin^2(\zeta) & 1/2\sin(2\zeta) \\ \sin^2(\zeta) & \cos^2(\zeta) & -1/2\sin(2\zeta) \\ -\sin(2\zeta) & \sin(2\zeta) & \cos(2\zeta) \end{pmatrix} \tag{3.4}$$

The orientation of the grain is defined solely by ζ, the angle between the $c-axis$ and the global x_1 direction (see Fig. 3-1b).

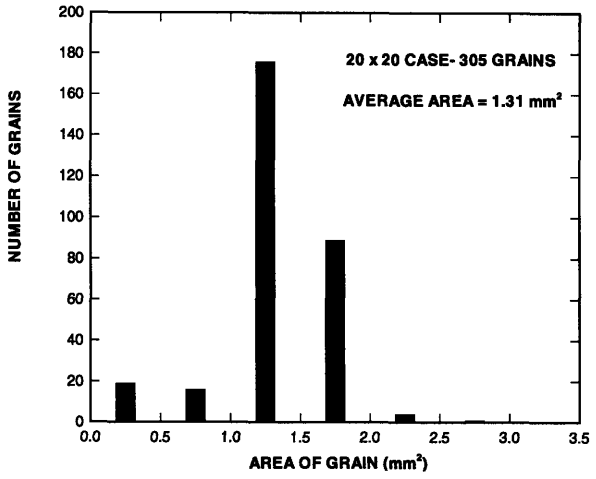

(a)

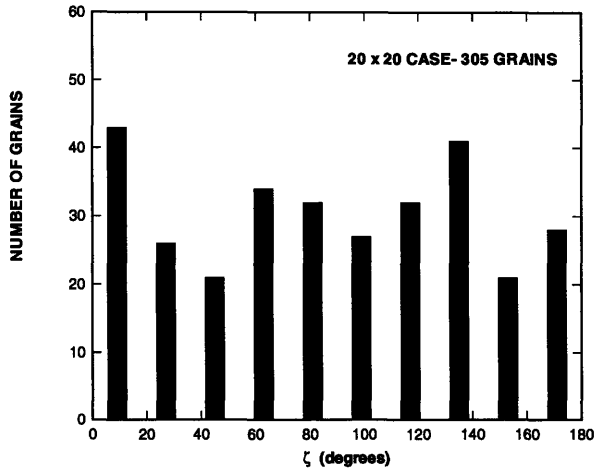

(b)

Figure 3-2: Typical histograms for a 20×20 mm^2 sample of: (a) Grain area; (b) Grain orientation.

As indicated above, the $c-axes$ are distributed uniformly in the $x_1 - x_2$ plane. Hence, in the numerical simulations each grain in the aggregate is associated with an orientation ζ which is chosen randomly from the range $0° \leq \zeta \leq 180°$. A typical histogram of uniformly distributed

ζ is shown in Fig. 3-2b; this figure corresponds to the 20×20 mm^2 sample shown in Fig. 3-1a. Figure 3-3 shows the grain geometries as well as the spatial distribution of ζ for various specimen sizes; notice the close resemblance with experimental observation of grain geometry reported in Sinha (1989b).

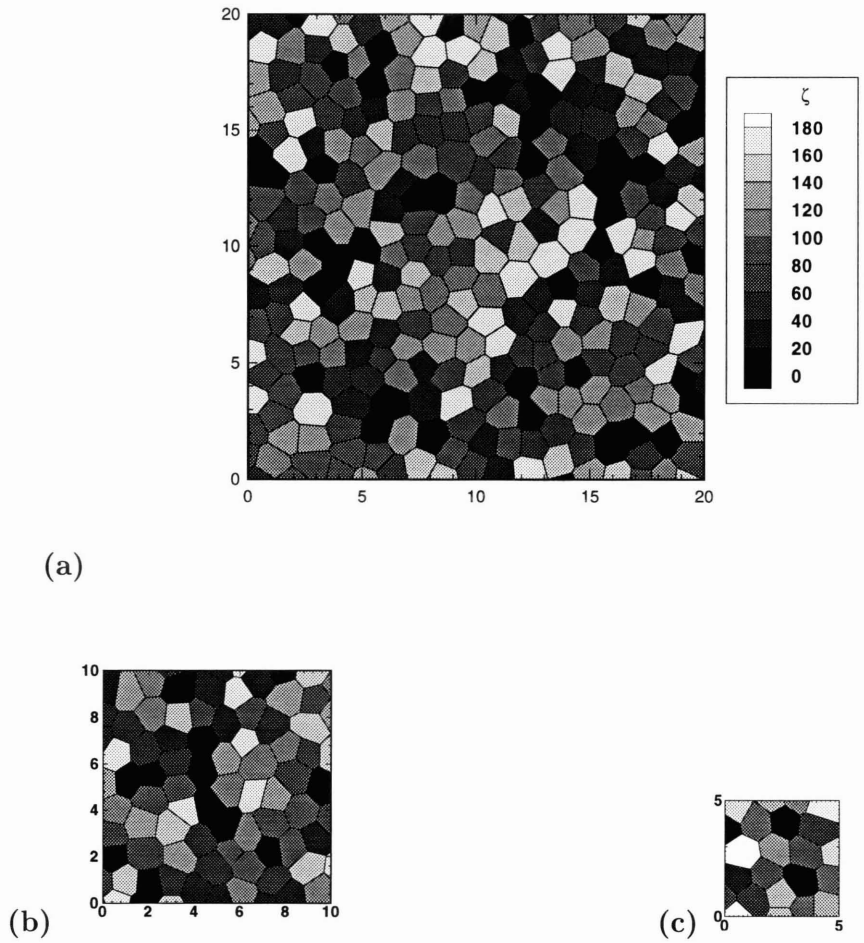

Figure 3-3: Typical grain geometries and spatial distributions of grain orientation, ζ, for specimens of size: (a) 20×20 mm^2, (b) 10×10 mm^2, and (c) 5×5 mm^2.

3.2.3 Computational Model

The stress, strain and displacement fields in the heterogeneous assembly of grains are solved using the finite element method. Each grain is discretized into as many six-noded plane stress elements as there are facets in the grain. Figure 3-4a shows a grain assembly and the corresponding discretization; a typical discretized grain is shown separately in Figure 3-4b. Note that the elements do not straddle the grain boundaries. The anisotropic elastic material properties of each element

are assigned according to the grain orientation ζ and Eqs 3.3 and 3.4.

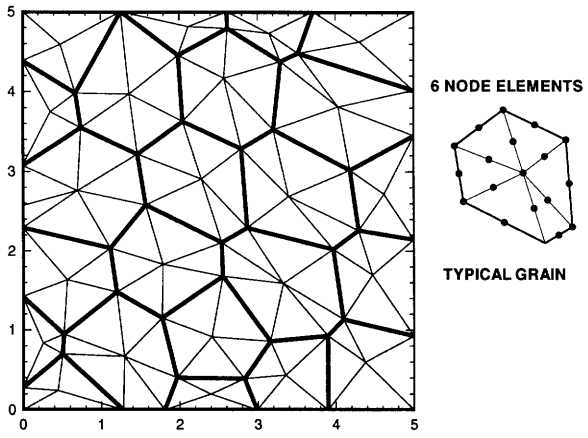

Figure 3-4: (a) Typical grain assembly and the finite element discretization; (b) Detail of discretization of a typical grain.

The two limits of (i) no grain boundary sliding, and (ii) free grain boundary sliding are modeled as follows. In the coordinate axes of the grain facet $x_1'-x_2'$ (see Fig. 3-1b) constrain the displacement components, u_i':
For no grain boundary sliding:

$$u_1'^{+} = u_1'^{-} \quad \text{and} \quad u_2'^{+} = u_2'^{-}$$

For free grain boundary sliding:

$$u_2'^{+} = u_2'^{-} \tag{3.5}$$

where the $+$ and $-$ refer to two points lying infinitesimally close to, but on either side of, the grain boundary. These constraints on the displacements are enforced by the penalty method.

To verify the fineness of the discretization the number of nodes is varied by changing the type and order of the elements: four and eight node quadrilateral elements, and three and six node triangular elements are considered. Discretizations of a typical grain with quadrilateral and triangular elements are shown in Fig. 3-5(a) and (b) respectively. The *global* convergence of the finite element discretization is quantified by the total strain energy, $\mathcal{E}$, of the aggregate:

$$\mathcal{E} = \frac{1}{2}\int_{\Omega} \boldsymbol{\sigma} \bullet \boldsymbol{\epsilon}\, \mathrm{d}\Omega = \int_{\Gamma} \mathbf{P} \bullet \mathbf{u}\, \mathrm{d}\Gamma \tag{3.6}$$

where $\boldsymbol{\sigma}$ and $\boldsymbol{\epsilon}$ are the stresses and strains, Ω is the total volume of the sample, $\mathbf{P}$ and $\mathbf{u}$ are tractions and displacements on the boundary Γ. In a typical case, with no grain boundary sliding, by increasing the number of nodes from 1167 (triangular three node elements) to 5131 (eight node

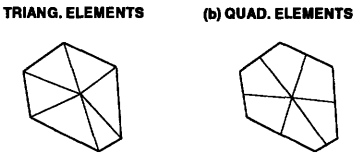

Figure 3-5: Discretization of a typical grain with: (a) Triangular elements; (b) Quadrilateral elements.

quadrilaterals) decreases $\mathcal{E}$ by only 0.4%. [1] When grain boundary sliding is allowed, $\mathcal{E}$ varies as follows: 67.3, 61.4, 57.8, and 55.6 for 1167, 2158, 3149, and 5131 nodes, respectively. The variation in $\mathcal{E}$ by discretizing with six versus eight node elements is 4%. Thus using six noded elements is more then acceptable when no grain boundary sliding is allowed and is satisfactory when grain boundary sliding is permitted. Note that the adopted discretization does not capture all the details in the stress field variation close to the grain triple points. However, since this chapter is concerned with *homogenized* polycrystal behavior and since the zones of high stress variation are small, they have little effect on the sought solution and will be ignored.

3.2.4 Homogenized Elastic Constants

The overall planar response of polycrystalline $S2$ ice with a sufficient number of grains is isotropic. This material symmetry is fully characterized by two homogenized elastic constants: the homogenized Young's modulus, $\bar{E}$ and the homogenized Poisson ratio, $\bar{\nu}$. These parameters are determined from numerical simulations of a polycrystal sample subjected to uniaxial loading as follows.

Consider a rectangular, multi grain sample of width w and height h (see Fig. 3-1). The sample boundary $x_2 = 0$ is prevented from displacing; $u_2 = 0$. To ensure numerical stability one node on this boundary is also pinned. This allows unconstrained expansion/ contraction in the x_1 direction on $x_2 = 0$. The sample is loaded uniaxially by applying an uniform displacement, u_2 all along the boundary $x_2 = h$.

The homogenized isotropic elastic constants are defined as:

$$\bar{E} = \frac{\bar{\Sigma}_2}{\bar{\epsilon}_2} \qquad \text{and} \qquad \bar{\nu} = -\frac{\bar{\epsilon}_1}{\bar{\epsilon}_2} \tag{3.7}$$

where the average quantities are:
Average normal strain components in x_1 and x_2 directions:

$$\bar{\epsilon}_1 = \frac{1}{w}\int_0^h \frac{u_1(x_1 = w, x_2) - u_1(x_1 = 0, x_2)}{h}\, \mathrm{d}x_2$$

[1] This particular specimen contains 176 grains; the sample size is 15 x 15 mm^2.

$$\bar{\epsilon}_2 = \frac{1}{h}\int_0^w \frac{u_2(x_1, x_2 = h) - u_2(x_1, x_2 = 0)}{w}\, \mathrm{d}x_1 \tag{3.8}$$

Average normal stress component in x_2 direction:

$$\bar{\Sigma}_2 = \int_0^w \frac{T_2}{w}\, \mathrm{d}x_1 = \sum \frac{R_2(x_2 = h)}{w\, t} \tag{3.9}$$

where T_2 is the traction component in the x_2 direction. Note that $\bar{\Sigma}_2$ is most easily obtained from the finite element solution by summing all the nodal reaction components $R_2(x_2 = h)$ on the boundary $x_2 = h$ and dividing by the sample width w and thickness t.

3.3 Material Properties

The values for the dynamic elastic moduli of ice single crystals are given in Eq. (1.1). Reducing the single crystal stiffness, Eq. (1.1), to plane stress conditions by using Eq. (3.2), with $\sigma_{33} = 0$ and $x_1 - x_2$ being the plane of interest, the following is obtained:

$$\mathbf{C}_g(\zeta = 0°) = \begin{pmatrix} 12.624 & 2.832 & 0 \\ 2.832 & 10.328 & 0 \\ 0 & 0 & 3.014 \end{pmatrix} \; GPa \tag{3.10}$$

In the simulations conducted in this chapter these stiffness moduli are used.

3.4 Results and Discussion of Numerical Simulations

3.4.1 Number of Grains Required to Homogenize Elastic Properties

This section presents and discusses the results from simulations of uniaxial loading of polycrystalline ice specimens. Both limits of (i) no grain boundary sliding, and (ii) free grain boundary sliding are investigated. Only square samples ($h = w$ in Fig. 3-1a) are analyzed. The following seven specimen sizes, $h \times h$, are considered: $5 \times 5\ mm^2$, $7.5 \times 7.5\ mm^2$, $10 \times 10\ mm^2$, $12.5 \times 12.5\ mm^2$, $15 \times 15\ mm^2$, $17.5 \times 17.5\ mm^2$, and $20 \times 20\ mm^2$. Three typical specimens, all different in size, are shown in Fig. 3-3.

By choosing different seeds for the random number generator, different grain geometries are created for the same sample size, $h \times h$. The orientations of the grains, ζ, which effects the grains elastic properties in the global axes frame, are also re- randomized. Simulations with at least 25 different grain geometries and orientations, for each of the first four sample sizes, are performed. For each of the remaining larger samples, simulations with at least 30 different random grain geometries are conducted. Note that due to the method of generating the grain geometry (see Section 3.2.1) the number of grains in a $h \times h$ size sample is not constant. The number of simulations conducted for each sample size is thought to provide a good indication of the variation in the homogenized

elastic properties.

The effect of elastic anisotropy in the $h \times h$ sample is studied by randomly varying only the grain orientations, ζ. The grain geometry is held constant for each $h \times h$ sample. The same number of simulations are performed for each sample size as reported above.

The results presented below are independent of grain size. This was verified by generating self similar samples, each composed of different mean grain size, *i.e.*, the grain tessellation for the different sized samples was identical. The computed homogenized elastic properties were the same for the different self similar specimens. This observation is not surprising. In the uniaxial loading simulations, the stress fields depend on the length scale only near the triple points where the solution is singular. For ice, the singularities at the triple points are relatively weak (see *e.g.*, Gupta *et al.* (1993)). Hence the region effected by the singularities are small compared with the grain area and have little influence on the homogenized parameters sought.

It is interesting to note that in the self consistent method averaging only a small number of crystals gives accurate overall moduli. For example, Iwakuma and Nemat-Nasser (1984) calculated the overall moduli of a polycrystal solid, subject to finite elasto- plastic deformation, and needed only 46, or fewer, grain orientations (this corresponds to a sample smaller than the $7.5 \times 7.5\ mm^2$). These authors add a cautionary note that at large strains (presumably where the mismatch between grains has developed substantially) the overall behavior depends on the number of grains considered. The following question arises: will the number of grains required in the self consistent method suffice to homogenize the elastic properties when the polycrystal is viewed as an assembly of individual grains? In the self consistent method, the following auxiliary problem is solved first: a homogeneous matrix which possess the average macroscopic moduli with an embedded single grain (usually circular or ellipsoidal in shape) is subjected to nominal macroscopic loading. Subsequently, the overall and single crystal moduli are related by averaging over all crystal orientations and shapes. The assumption in the self consistent method that each crystal is surrounded by an equivalent *homogeneous matrix* is valid only if a sufficient number of grains surround the given crystal. An indication of this number is provided by Laws and Lee (1989): these authors calculate that at least 200 grains are required for accurate residual stress fields when the polycrystal is subject to a temperature drop.[2] Thus the number of grains required to homogenize the elastic properties is expected to be greater than in the self consistent scheme.

Effect of Temperature

Changing the temperature has the same effect on all the components of the single crystal moduli, see Eq. (1.2). Since linear elastic behavior is considered, having the solution at a certain temperature, T_{ref}, the solution at a new temperature T can be scaled using Eq. (1.2). In particular,

[2]Laws and Lee (1989) considered regular hexagonal grains which were elastically isotropic but thermally anisotropic.

the homogenized Young's modulus at a temperature T, $\bar{E}(T)$, is given by:

$$\bar{E}(T) = \bar{E}(T_{ref}) \frac{(1 - 1.418 \times 10^{-3} T)}{(1 - 1.418 \times 10^{-3} T_{ref})} \tag{3.11}$$

The homogenized Poisson ratio should be unaffected by a temperature change, since:

$$\bar{\nu} = \frac{\bar{E}(T)}{2\bar{G}(T)} - 1 \tag{3.12}$$

where $\bar{G}$ is the homogenized shear modulus, and the thermal effects on $\bar{E}(T)$ and $\bar{G}(T)$ are the same and hence cancel each other. Some evidence of the Poisson ratio independence of temperature has been observed experimentally by Langleben and Pounder (1963), in the $-3.6°C$ to $-15°C$ range, albeit for sea ice. However, Sinha (1989b) observes that there is little discrepancy in the reported dynamic Poisson ratio of different ice types.

No Grain Boundary Sliding

The homogenized elastic properties can be calculated by the spatial averaging methods of Voigt (1910) and Reuss (1929) (as done by Nanthikesan and Shyam Sunder (1994); Sinha (1989a); and Michel (1978)). As mentioned in the introduction, Hill (1952) showed that the Voigt and Reuss (V- R) limits give the upper and lower bound solutions for the aggregate stiffness moduli. Nanthikesan and Shyam Sunder (1994) calculate the V- R limits for the elastic properties of $S2$ ice in the plane of isotropy and at $-16°C$ to be:

$$\begin{aligned} 9.726 \geq \bar{E} \geq 9.431 \\ 0.320 \leq \bar{\nu} \leq 0.334 \end{aligned} \tag{3.13}$$

Figures 3-6a and 3-6b plot the homogenized Young's modulus, $\bar{E}$, and Poisson ratio $\bar{\nu}$ versus the number of grains obtained from the simulations with no grain boundary sliding. In this figure both the grains geometry and orientations are varied. The V-R upper and lower bounds given in Eq. (3.13), are also plotted. Figures 3-6a and 3-6b show that as the number of grains increase so the band of simulated homogenized properties decreases, and then reaches approximately a constant width. For sample sizes larger than $17.5 \times 17.5\ mm^2$, the bands of homogenized properties produced by the simulations are very close to the V-R band.

The effect of grain anisotropy is studied in Figs 3-7a and 3-7b, by varying only the grain orientations and keeping the grain geometry fixed. No grain boundary sliding is allowed. The bands produced by varying only ζ are wider than varying both grain geometry and orientations. Thus when there is no grain boundary sliding, the effect of grain anisotropy is greater then the effect of grain shape.

The minimum, average and maximum values of the homogenized elastic properties from all the simulations are reported in Table 3.1. The percentage difference between the maximum and minimum values are also give. From Table 3.1 it can be seen that the homogenized Poisson ratio

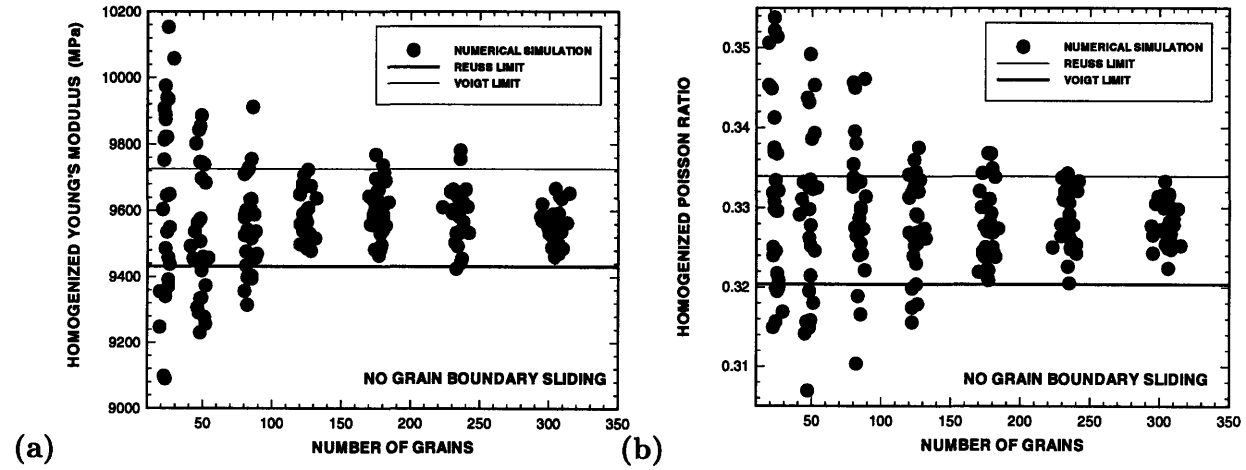

Figure 3-6: (a) Homogenized Young's modulus, $\bar{E}$, versus number of grains; (b) Homogenized Poisson ratio, $\bar{\nu}$, versus number of grains. No grain boundary sliding; both grain geometry and grain orientation varied.

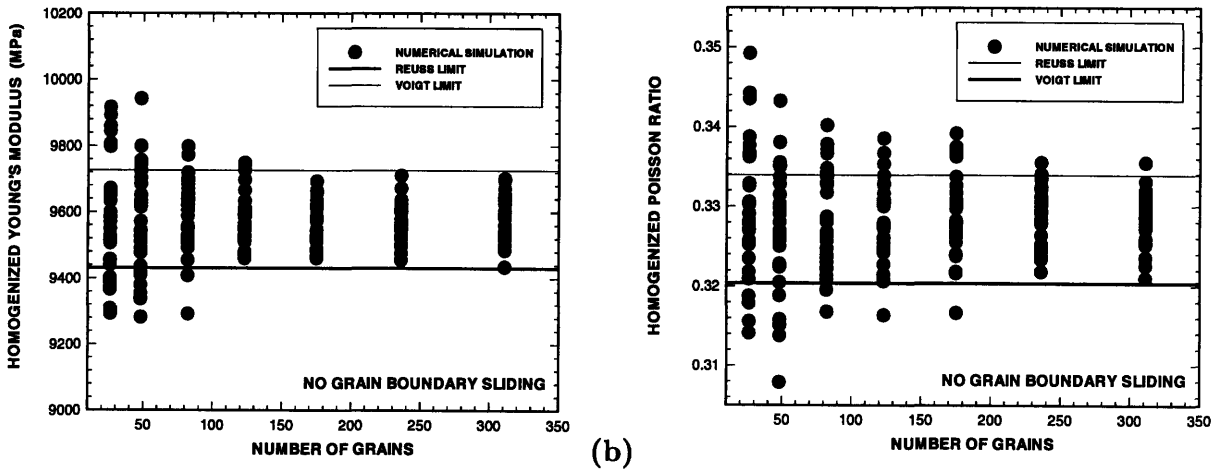

Figure 3-7: (a) Homogenized Young's modulus, $\bar{E}$, versus number of grains; (b) Homogenized Poisson ratio, $\bar{\nu}$, versus number of grains. No grain boundary sliding; only grain orientation varied.

converges slower than the Young's modulus. The averages of $\bar{E}$ and of $\bar{\nu}$ for different sample sizes are all approximately the same. This is due to the *random* variation of the grain geometry and grain shape. Table 3.1 shows that samples larger than 17.5 × 17.5 mm^2 produce bands narrower than 5% and which are very close to the V- R bounds. Note that the simulations conducted here are by no means exhaustive; however, the results indicate that a sample of 17.5 × 17.5 mm^2, or approximately 230 grains, serves as a representative area of the polycrystal.

Experimental data on the Young's modulus and Poisson ratio for polycrystalline ice are available

Sample Size (mm^2)	$\bar{E}$ (MPa)				$\bar{\nu}$			
	Min.	Ave.	Max.	% Diff.	Min.	Ave.	Max.	% Diff.
5×5	9090	9604	10153	11.7	0.291	0.329	0.354	21.72
7.5×7.5	9231	9549	9943	7.71	0.307	0.328	0.349	13.77
10×10	9293	9581	9912	6.67	0.310	0.329	0.346	11.52
12.5×12.5	9461	9582	9750	3.05	0.316	0.328	0.339	7.28
15×15	9462	9584	9769	3.24	0.317	0.328	0.339	7.12
17.5×17.5	9425	9576	9781	3.78	0.321	0.328	0.336	4.69
20×20	9436	9566	9702	2.83	0.321	0.328	0.336	4.52

Table 3.1: Statistics for homogenized Young's Modulus and Poisson ratio for various numbers of grains; no grain boundary sliding allowed; all simulations considered.

in the literature. Gold (1958) tabulates results of the sonic values of Young's modulus and Poisson ratio at $-5°C$. The reported values for the Young's modulus range from 8.95 GPa to 9.94 GPa; the Poisson ratio ranges from 0.31 to 0.365. Sinha (1978) measured the Young's modulus of polycrystalline $S2$ ice in the plane of isotropy, at temperatures between $-40°C$ and $-45°C$, and reports a range of $9.1 - 9.8$ GPa with an average of 9.3 GPa. More recently, the Poisson ratio was measured by Sinha (1989b) at $-20°C$ to be 0.31- 0.32. The numerical simulations on 17.5 × 17.5 mm^2 samples predict the Poisson ratio to lie in the range 0.32- 0.34. The average homogenized Young's modulus, corrected for temperature according to Eq. (3.11), are: at $-5°C$, $\bar{E} = 9.43$ GPa, and at $-40°C$, $\bar{E} = 9.89$ GPa. The simulated values are in agreement with experimental measurements.

Grain Boundary Sliding

The results presented in this section are from simulations with free grain boundary sliding. In Figs 3-8a and 3-8b the homogenized Young's modulus, $\bar{E}$, and Poisson ratio $\bar{\nu}$ are plotted versus the number of grains in the sample; both the grains geometry and orientations are varied. The effect of elastic anisotropy is studied in Figs 3-9a and 3-9b, where only the grain orientations are varied, for a single grain geometry. The results from all these simulations are presented in Table 3.2.

As to be expected, as the number of grains increases so the bands in the homogenized elastic properties decreases. For samples bigger than 17.5 × 17.5 mm^2, *i.e.* samples containing more than 230 grains, the bands' widths approximately stabilize. Note that the grains on the specimen border are relatively unconstrained, and due to *free* grain boundary slip, are almost unloaded. Hence in the smaller samples, where the number of grains on the border is a large fraction of the total number of grains, large variability is seen in the homogenized elastic properties.

The bands formed by varying only the grain orientations (Figs 3-9a and 3-9b) are much narrower than when both the grain geometry and the orientations are varied (Figs 3-8a and 3-8b). Thus grain shape is more important than elastic anisotropy when grain boundary sliding occurs. This conclusion is in contrast to the case of no grain boundary sliding, where elastic anisotropy is more

Sample Size (mm^2)	$\bar{E}$ (MPa)				$\bar{\nu}$			
	Min.	Ave.	Max.	% Diff.	Min.	Ave.	Max.	% Diff.
5×5	6687	7408	8306	24.22	0.412	0.475	0.503	22.11
7.5×7.5	6947	7815	8148	17.29	0.425	0.456	0.560	31.83
10×10	7246	7738	8182	12.91	0.417	0.463	0.526	26.06
12.5×12.5	7300	7738	8076	10.64	0.430	0.455	0.487	13.32
15×15	7337	7765	8184	11.54	0.425	0.453	0.479	12.86
17.5×17.5	7526	7828	8060	7.10	0.433	0.447	0.473	9.15
20×20	7620	7827	7997	4.95	0.430	0.450	0.466	8.63

Table 3.2: Statistics for homogenized Young's Modulus and Poisson ratio for various numbers of grains; free grain boundary sliding permitted; all simulations considered.

dominant in producing the variability in the polycrystal elastic constants.

Sinha (1989b) measured the effective Young's modulus and Poisson ratio of fresh water polycrystalline $S2$ ice at $-20°C$. His results show that the Poisson ratio decreases monotonically from about 0.7 to 0.3 as the strain rate varies from $10^{-7}\ s^{-1}$ to $10^{-2}\ s^{-1}$. The effective Young's modulus increased from 4 GPa to approximately 9.5 GPa. Gold (1958) also reports data from experiments conducted on the same type of ice, but under static loading conditions; his results indicate Poisson ratio values of 0.31- 0.54. In both these references the stress was restricted to low levels where the deformation was homogeneous and elastic; both references reason that grain boundary slip plays a role in the observed strains. The average elastic parameters obtained from the simulations when grain boundary sliding is allowed, are: $\bar{E} = 7.9\ GPa$ and $\bar{\nu} = 0.45$. These simulated values are in accord with the above experimental observations. The predicted elastic properties correspond to the strain range $10^{-4}s^{-1} - 10^{-3}s^{-1}$ in the data of Sinha (1989b). This strain range corresponds

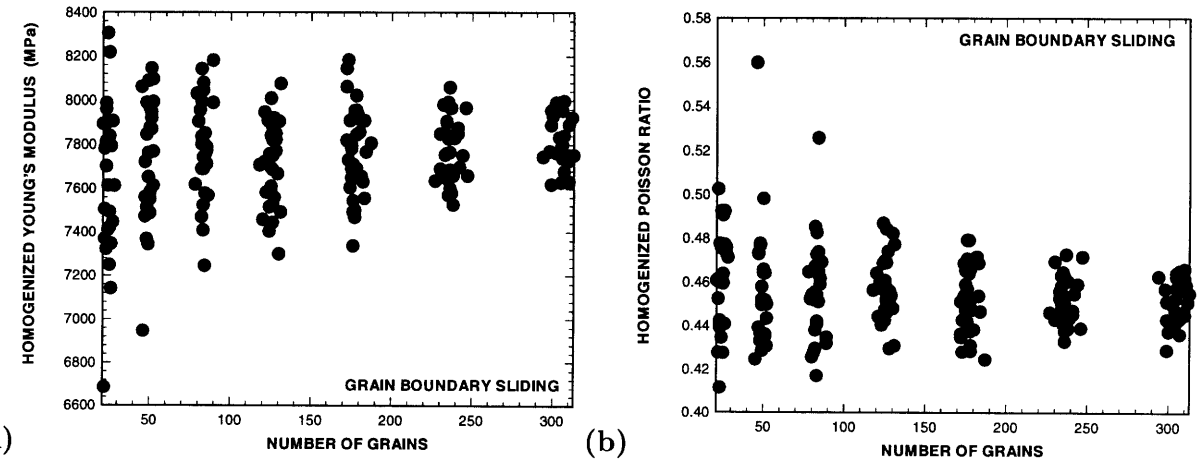

Figure 3-8: (a) Homogenized Young's modulus, $\bar{E}$, versus number of grains; (b) Homogenized Poisson ratio, $\bar{\nu}$, versus number of grains. Free grain boundary sliding; both grain geometry and grain orientation varied.

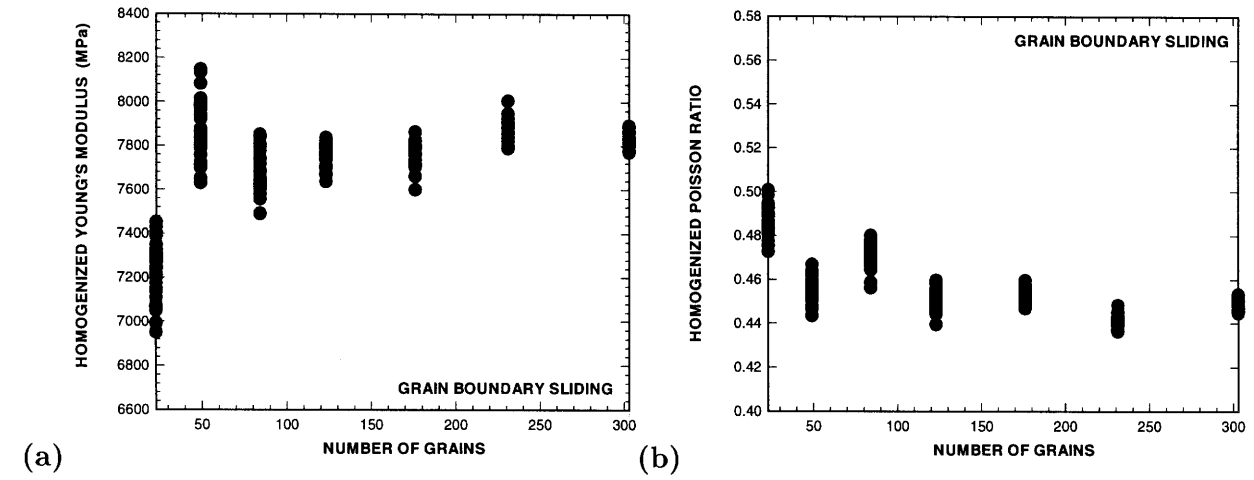

Figure 3-9: (a) Homogenized Young's modulus, $\bar{E}$, versus number of grains; (b) Homogenized Poisson ratio, $\bar{\nu}$, versus number of grains. Free grain boundary sliding; only grain orientation varied.

to the ductile to brittle transition in polycrystalline ice where maximum compressive stresses are observed.

3.4.2 Statistical Distribution of Stress at Grain Centers

Due to the elastic mismatch between neighboring crystals, residual stresses are set up within the grains when the polycrystal is loaded. Ortiz and Suresh (1993) have shown that the residual stresses within a polycrystal ceramic, subject to thermal cooling, follow the Gaussian distribution. They considered an array of regular hexagonally shaped grains, with elastic and thermal anisotropy, and no grain boundary slip. This section extends the work of Ortiz and Suresh (1993). The statistical distribution of stresses when a polycrystal of non- regular shaped grains subject to uniaxial loading is presented; both no grain boundary sliding and free grain boundary sliding are considered.

The probability distributions of the stress components for two typical 20×20 mm^2 samples, one without grain boundary sliding, and the other with free grain boundary sliding, are plotted in Figs 3-10 and 3-11 respectively. The stresses only at the grain centers are considered. The magnitude of the stress components are normalized by the applied uniaxial stress; since the specimen is loaded by a displacement, u_2 (see Section 3.2.4), the equivalent normalizing stress is given by $|\bar{E}u_2/h|$. In addition, Gaussian distributions, or normal curves are fitted to the simulated normalized stress components. The Gaussian curves require the mean stress component, $\bar{\sigma}_i$, and the standard deviation, s_i:

$$\bar{\sigma}_i = \frac{1}{N}\sum_{j=1}^{N}(\sigma_i^*)_j$$

$$s_i^2 = \frac{1}{N}\sum_{j=1}^{N}((\sigma_i^*)_j - \bar{\sigma}_i)^2 \tag{3.14}$$

where N is the number of grains in the specimen, and σ_i^* is the normalized stress component i.

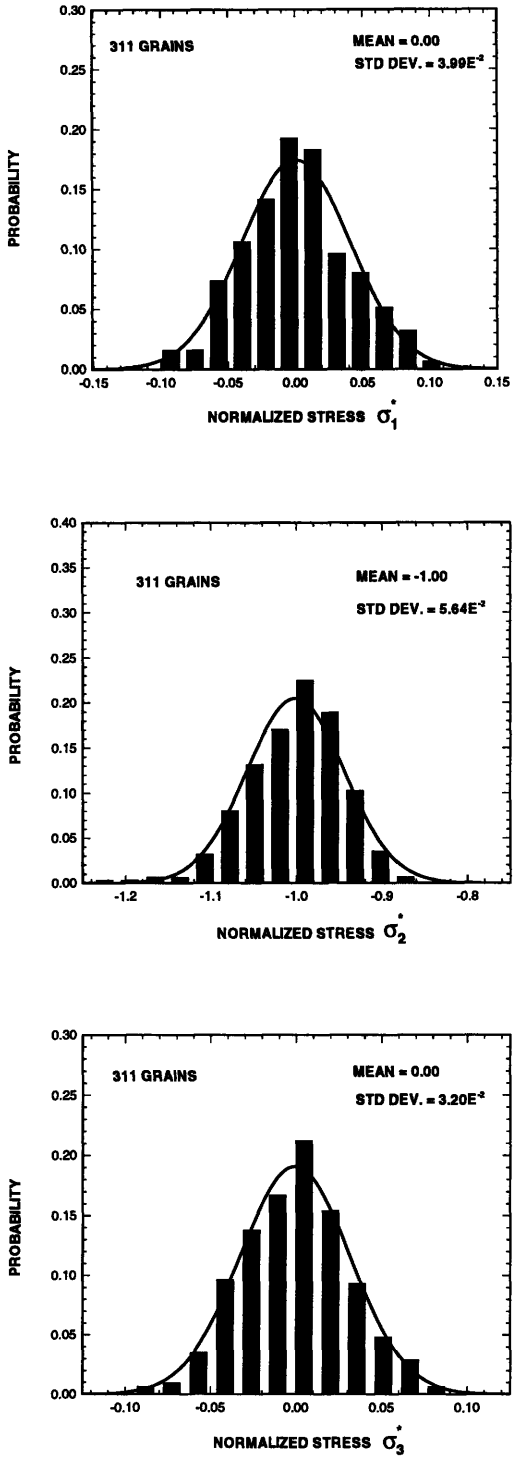

Figure 3-10: Statistical distribution of stress components at the grain centers; no grain boundary sliding. Solid lines represent Gaussian fits.

The stress components in a polycrystalline aggregate approximately follow the Gaussian distribution; as observed by Ortiz and Suresh (1993) in hexagonal grains. When no grain boundary

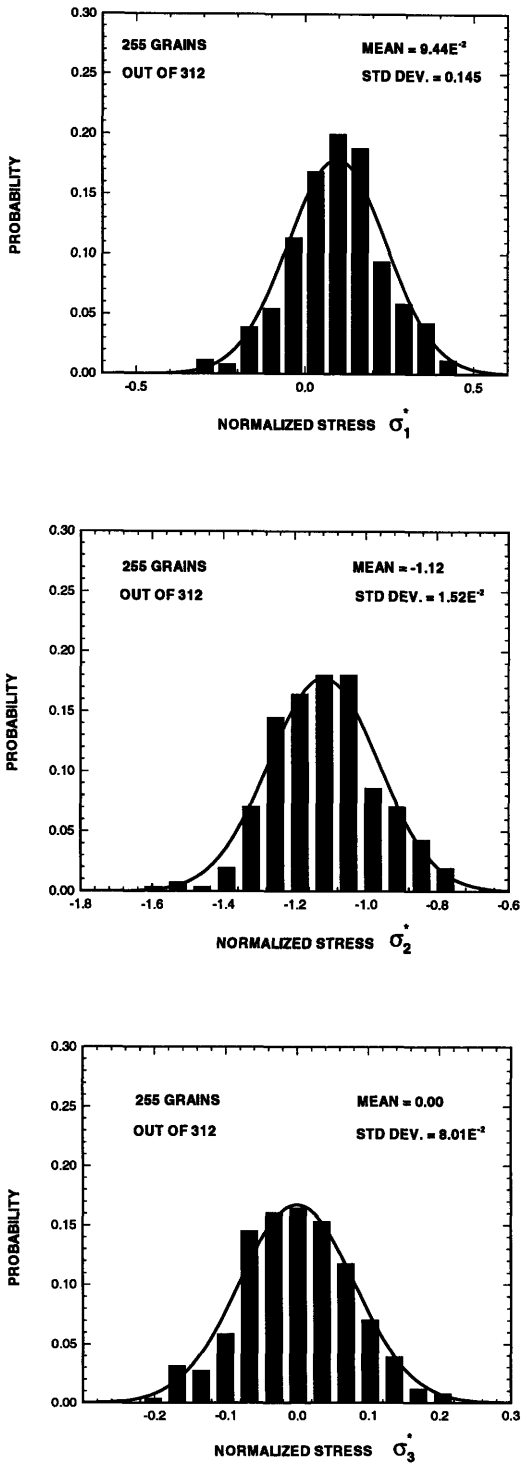

Figure 3-11: Statistical distribution of stress components at the grain centers; free grain boundary sliding. Solid lines represent Gaussian fits.

sliding is permitted (Fig. 3-10), the lateral $\bar{\sigma}_1$ and shear $\bar{\sigma}_3$ have zero mean stress components. In the uniaxial direction on the other hand, $\bar{\sigma}_2$, the mean normalized stress is -1; the negative sign

indicates that the applied displacement loading, u_2 caused uniaxial *compression*. These results are to be expected since equilibrium has to be maintained.

When free grain boundary sliding is allowed, the grains on the sample boundary are unconstrained, and hence unloaded relative to the grains within the sample. The specimen boundary grains bias the stress distributions, and hence these grains are excluded in Fig. 3-11. The distributions for the free grain boundary slip case are also approximately Gaussian. Note however, while the mean shear stress component $\bar{\sigma}_3$ is once again zero, the other mean components, $\bar{\sigma}_1 \neq 0$ and $\bar{\sigma}_2 \neq -1$. The mean stresses are not the same as in the no grain boundary sliding case because of two effects. First, due to the applied uniaxial compression and grain boundary slip, at each grain triple point, one grain wedges the other two grains apart. This results in: (i) the wedging grain having a locally high *compressive* σ_2 component, and (ii) the other two grains having locally high *tensile* σ_1 components. Second, since the stress components are sampled only at the grain centers, instead of taking a volume average, the wedging effect is not canceled out. Hence, the mean lateral normalized stress component is tensile, $\bar{\sigma}_1 > 0$ while the mean axial component $\bar{\sigma}_1 < -1$. The local grain wedging action, causing locally tensile σ_1 fields, has significant implications for microcracking in polycrystalline ice loaded in compression (see Elvin and Shyam Sunder (1994) for details).

3.5 CONCLUSION

This chapter examines how many grains are required to homogenize the elastic behavior of polycrystalline $S2$ ice. Two extreme limits are considered: (i) no grain boundary sliding, and (ii) free grain boundary slip. The grain geometry is modeled by modified Voronoi polygons. The elastic anisotropy of the grains is accounted for. Finite element simulations of uniaxial compression of various size specimens are conducted.

Results show that at least 230 grains are required in order for the polycrystal aggregate to exhibit homogenized elastic behavior. When no grain boundary sliding is allowed, numerically computed homogenized Young's modulus and Poisson ratio bands are very close to the Voigt and Reuss theoretical upper and lower bounds. The effect of grain anisotropy on the homogenized elastic constants is more important then grain shape when no grain boundary sliding is allowed. The effect of grain shape on the homogenized properties is dominant when free grain boundary sliding occurs. The average computed homogenized Young's modulus and Poisson ratio are: 9.58 GPa and 0.33- with no grain boundary sliding; 7.83 GPa and 0.45- with free grain boundary sliding. The stress components at the grain centers approximately follow a Gaussian distribution. The same distribution was calculated by Ortiz and Suresh (1993), but for an array of hexagonal grains subject to thermal loading and with no grain boundary sliding.

The 230 grains required to homogenize the elastic response of the polycrystal defines the representative area element. At least this number of grains has to be considered when conducting micromechanical studies on $S2$ ice. On the other hand, the resolution in large scale boundary value problems, with homogeneous constitutive laws (*e.g.*, in plane indentation of a floating ice sheet) especially in regions of high stress fluctuation, cannot be finer than this representative area element.

REFERENCES

[1] Elvin, A.A. and S. Shyam Sunder, (1994), Microcracking Due to Grain Boundary Sliding in Polycrystalline Ice Under Uniaxial Compression, *Acta Metall. et Mater.*, in Press.

[2] Frost, H. J. and C.V. Thompson, (1987), The Effect of Nucleation Conditions on the Topology and Geometry of Two- Dimensional Grain Structures, *Acta Metall.*, 35, 529.

[3] Gold, L.W., (1958), Some Observations on the Dependence of Strain on Stress for Ice, *Can. J. Phys.*, 36, 1265.

[4] Gupta, V., R.C. Picu and H.J. Frost, (1993), Crack Nucleation Mechanism in Saline Ice, *Ice Mechanics*, in: J.P. Dempsey, Z.P. Bazant, Y.D.S. Rajapakse and S.S. Sunder, eds., ASME, AMD, 163, p. 199.

[5] Hill, R., (1952), The Elastic Behavior of a Crystalline Aggregate, *Proc. Phys. Soc.*, A 65, 349.

[6] Iwakuma, T. and S. Nemat-Nasser, (1984), Finite Elastic- Plastic Deformation of Polycrystalline Metals, *Proc. R. Soc. Lond.*, A 394, 87.

[7] Langleben, M. P. and E.R. Pounder, (1963), Elastic Parameters of Sea Ice, in: W.D. Kingery, ed., *Ice and Snow*, MIT Press, Cambridge, MA, p. 69.

[8] Laws, N. and J.C. Lee, (1989), Microcracking in Polycrystalline Ceramics: Elastic Isotropy and Thermal Anisotropy, *J. Mech. Phys. Solids*, 37, 603.

[9] Michel, B. and R.O. Ramseier, (1971), Classification of River and Lake Ice, *Can. Geotech. J.*, 8, 36.

[10] Michel, B., (1978), The Strength of Polycrystalline Ice, *Can. J. Civil Eng.*, 5, 285.

[11] Nanthikesan, S. and S. Shyam Sunder, (1994), Anisotropic Elasticity of Polycrystalline Ice I_h, *Cold Reg. Sci. Technol.*, 22, 149.

[12] Nemat-Nasser, S. and M. Hori, (1993), *Micromechanics: Overall Properties of Heterogeneous Materials*, Elsevier, Amsterdam.

[13] Ortiz, M. and S. Suresh, (1993), Statistical Properties of Residual Stresses and Intergranular Fracture in Ceramic Materials, *J. Appl. Mech.*, 60, 77.

[14] Reuss, A.Z., (1929), Berechnung der Fliebgreneze von Mischkristallen auf Grund der Plastizitatsbedingung fur Einkristalle, *Z. Angew. Math. Mech.*, 9, 49.

[15] Sinha, N.K., (1978), Rheology of Columnar-Grained Ice, *Exp. Mech.*, 18, 464.

[16] Sinha, N.K., (1989a). Elasticity of Natural Types of Polycrystalline Ice, *Cold Reg. Sci. Technol.*, 17, 127.

[17] Sinha, N.K., (1989b), Experiments on Anisotropic and Rate-Sensitive Strain Ratio and Modulus of Columnar- Grained Ice, *J. Offshore Mech. Arc. Eng.*, 111, 354.

[18] Voigt, W., (1910), *Lehrbuch Der Krystallphysik*, Feubner., Berlin.

Chapter 4

THICKNESS EFFECT ON THE TRANSVERSE SHEAR MODULUS OF ICE PLATES

ABSTRACT

The effects of ice plate thickness on the transverse shear modulus is investigated in this chapter. An unit cell model containing a polycrystal aggregate is set up and the resulting boundary value problem is solved by the finite element method. The loading rate is assumed to be fast enough so that the polycrystal response is linear. Results show that the homogenized shear modulus can increase approximately five times as the plate thickness increases from 0.05 to 1.2 m. The increase is linear with thickness when the grain boundary shear stiffness is low, becoming non linear at higher boundary stiffnesses; when there is no grain boundary deformation the homogenized shear modulus is constant, *i.e.* independent of plate thickness. The thickness effect is due to grain boundary deformation and grain coarsening with plate depth. Temperature effects, which are accounted for by changing the grain boundary shear stiffness, significantly influence the homogenized transverse shear modulus.

4.1 INTRODUCTION

This chapter addresses the question: can a homogenized elastic property such as the transverse shear modulus, be dependent on ice plate thickness? The shear modulus is required in the solution of boundary value problems involving out of plate plane behavior. The macroscopic shear modulus of the plate is a result of homogenization of the response of individual grains.

In the present study, attention is focused on columnar grained $S2$ ice as classified by Michel and Ramseier (1971). In $S2$ ice the crystal $c-axes$ are randomly oriented in the horizontal x_1-x_2 plane– see Fig. 4-1. This type of ice occurs on lakes, rivers with slow currents and in the arctic. Depending on the rate of loading, and on temperature, polycrystalline ice behavior can be ductile or brittle. Here, the loading rate is assumed to be fast enough so that the polycrystal behaves linearly. The maximum (failure) stresses in this regime occur at small strains ($< 1\%$).

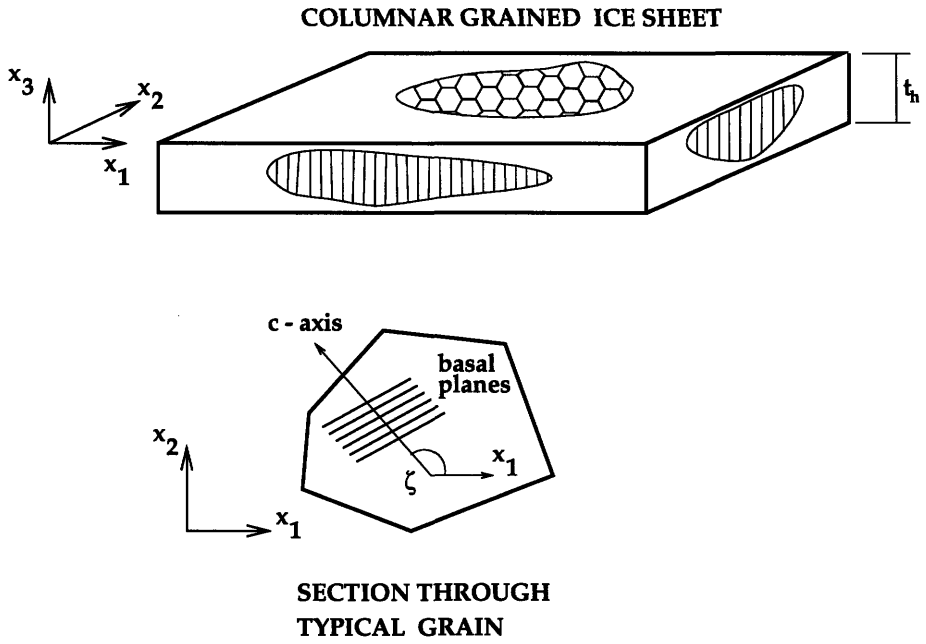

Figure 4-1: (a) Schematic of a columnar grained ice plate. (b) Horizontal section through a typical grain.

The crystallographic axes, and hence the elastic properties of neighboring grains are seldom aligned in the same direction. The homogenized elastic moduli have been calculated by Nanthikesan and Shyam Sunder (1994), among others (this reference cites other work), using the averaging methods of Voigt (1910) and Reuss (1929). The Voigt and Reuss methods (V-R) give the upper and lower bounds on the elastic moduli (Hill (1952)). Nanthikesan and Shyam Sunder (1994) show that the V-R limits for the transverse shear modulus are 3.219 and 3.206 MPa. The difference between the bounds is only 0.4%. Thus, as these authors note, either bounds or an average can be used as the homogenized transverse shear modulus.

The assumption in calculating the V-R homogenized shear modulus is that there is no grain boundary deformation. Recent experimental observations made by Nickolayev and Schulson (1995) show that grain boundary slip can occur even at high strain rates in polycrystalline ice. Further, theoretical work of Elvin and Shyam Sunder (1996) attribute microcracking at fast loading rates to grain boundary deformation. In this paper, grain boundary deformation is considered when calculating the homogenized transverse shear modulus. The amount of grain boundary deformation is controlled by grain boundary shear stiffness.

Finite element simulations of shear loading of polycrystalline unit cells, containing ice plates of various thickness, are conducted in this chapter. The modeling of grain geometry, grain boundary shear stiffness, and the grain elastic properties are described in Sections 4.2.1– 4.2.3. The unit cell and the finite element model for the ensemble is set up in Section 4.2.4. The methods of homogenizing the transverse shear modulus are presented in Section 4.2.5. The results from the simulations of the effects of: (1) thickness, (2) grain coarsening, and (3) grain boundary stiffness, on the homogenized transverse shear modulus are presented and discussed in Section 4.3. This chapter is concluded with notes on several important implications of the simulation results.

4.2 The Unit Cell Model

The behavior of a polycrystal ensemble can be studied by considering a sufficiently large sample so that edge effects are negligible. This typically requires a computationally prohibitive number of grains. An alternative approach is to assume that the microstructure can be subdivided into repetitive cells. One such unit cell is subjected to boundary conditions which ensure compatability with identical neighboring cells. Thus edge effects present in a finite sample are removed in an unit cell model. The unit cell, together with the computational model used in the subsequent numerical simulations are presented in this section after first describing the grain, and grain boundary properties.

4.2.1 Modeling The Grain Geometry

The grain geometry in the columnar zone has been studied by Weeks and co-workers, among others, by taking horizontal sections [1] at various depths in sea ice sheets. Three independent data sets have been compiled by Weeks and Ackley (1986), and show that the average grain size, $d(x_3)$, increases linearly with depth, x_3, as:

$$d(x_3) = d_0 + 0.033\ |x_3| \tag{4.1}$$

where d_0 is the average grain size at the top of the columnar zone, and the grain size in the average is defined as $d_i = \sqrt{g_{max}\ g_{min}}$, where g_{max} is the maximum grain dimension in the horizontal plane, and g_{min} is the grain dimension perpendicular to g_{max}. Weeks and Hamilton (1962) have shown that there is a large spread in $g_{max} : g_{min}$ ratios and that a linear regression fit of the data gives $g_{max} : g_{min} = 2 : 1$. The empirical Eq. (4.1) is based on data collected in the range $0 < x_3 < -600\ mm$; at greater depths, there is not a sufficient number of grains in the horizontal sections. It is interesting to note that the grain coarsening effect in ice sheets is comparable to that observed in metals (Weeks and Ackley (1986)).

The grain coarsening expressed by Eq. (4.1) can be seen in vertical thin sections. For example, Gow and Ueda (1989) show thin fresh water ice plates of the order of $t_h \approx 10cm$ with several grains through the thickness. Thicker plates contain more grains through the thickness and require

[1] The horizontal plane is the $x_1 - x_2$ plane, see Fig. 4-1

a collage of vertical sections (*e.g.* see Weeks and Ackley (1986) and Wei *et al.* (1995)). In thick ice plates crystals can be traced for 10 *cm* or more (Gow (1995)). However, systematic studies of the number of grains and grain length versus ice plate thickness have not been conducted (Gow (1995), Meese (1995)).

The grain coarsening occurs both in the x_1 and x_2 directions. Thus a three dimensional boundary value problem should be set up. However, a geometric model of the grain structure in three dimensions does not exist due to difficulty in measurements (Gow (1995)). For this reason, a two dimensional unit cell corresponding to a vertical section through the ice sheet (plane $x_1 - x_3$) is developed. The unit cell is subject to plane strain conditions. The planar assumption is an approximation to the real three dimensional problem. It is believed that the results obtained using the planar model give a quantitative indication of the real behavior.

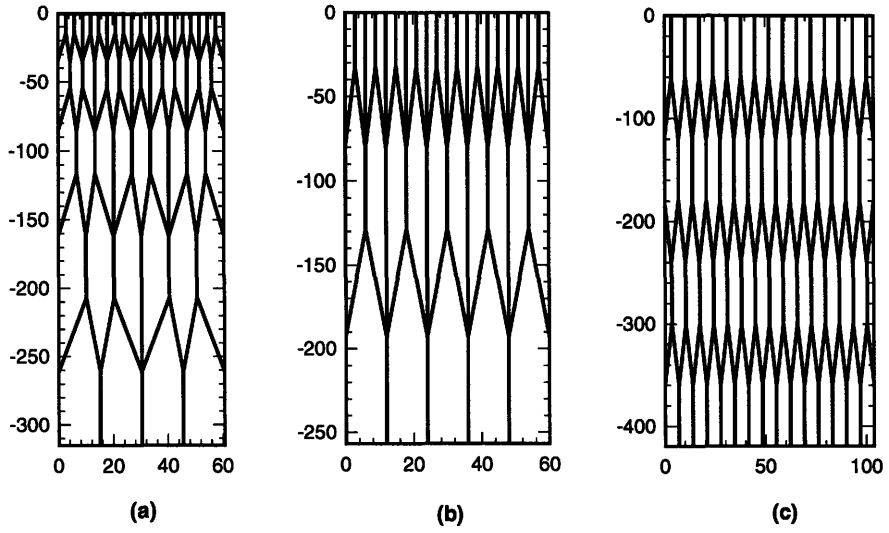

Figure 4-2: Idealized grain geometries with three coarsening factors: (a) $f = 1.5$; (b) $f = 2$; and (c) $f = 1$.

The grain geometry in the vertical section (plane $x_1 - x_3$) is modeled by idealizing the grains as modified hexagons, see Fig. 4-2a- c. It is assumed that the vertical section is taken so that all the grains in Fig. 4-2 show their maximum horizontal dimensions, g_{max}. In reality, a vertical section will produce a range of horizontal grain dimensions. The number of grains in each row decreases with depth by a constant coarsening factor, f. Three coarsening factors are considered: (a) $f = 1.5$, Fig. 4-2a; (b) $f = 2$, Fig. 4-2b; and (c) $f = 1$, Fig. 4-2c. The last case represents constant grain d throughout the plate– a fictitious case included for comparison. In the last case a constant grain length of 120 *mm* is assumed.

Since no data is available on grain lengths, this information is obtained by fitting the idealized grain geometry to the horizontal grain data, Eq. (4.1). The grain size d is computed based on $g_{min} = \frac{1}{2} g_{max}$ (consistent with Weeks and Hamilton (1962)) and g_{max} appears in the vertical

section– see Fig. 4-2. The resulting fit for $f = 1.5$ and $f = 2$, together with Eq. (4.1) are plotted in Fig. 4-3a and b, respectively. Equation (4.1) is extrapolated beyond $600mm$ by the dotted line. Notice that due to the grain idealization the grain d increases in jumps and not continuously as observed. As the grain d increase so does the grain length.

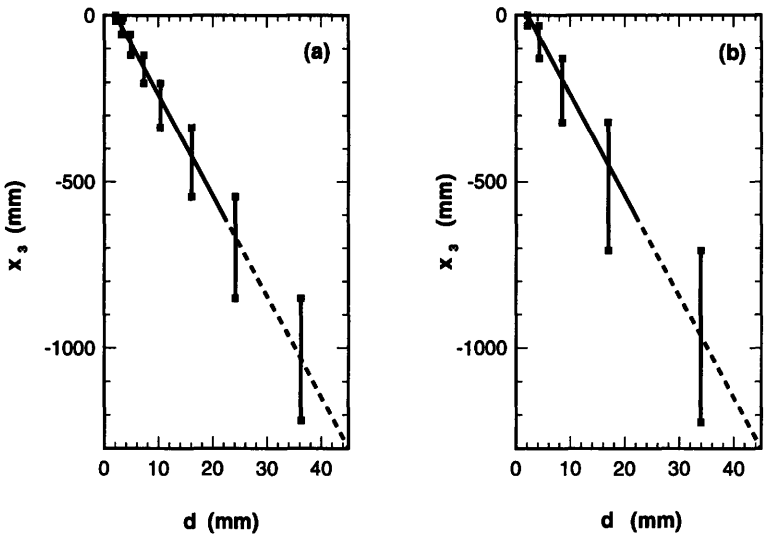

Figure 4-3: Grain size versus depth: experimental curve and fitted idealized numerical geometry. The numerical geometry has coarsening factors: (a) $f = 1.5$; and (b) $f = 2$.

An ice sheet of thickness $t_h = 1200mm$ requires eight grains when $f = 1.5$ and only five grains when $f = 2$. The rate of increase in d in the latter case is too fast (d doubles with each row) hence requiring too few grains through in the ice plate thickness. The $f = 1.5$ case is believed to be more realistic and forms the base case in this study. In reality f might be even lower.

The vertices in the regular geometry, *i.e.* the base case Fig. 4-2a, are also shifted to random locations within an area defined by: $0.2d$ in x_1 direction, and $0.7d$ in x_3 directions. This area is centered on the vertex being shifted. The size of this area is chosen to prevent (i) possible overlap of neighboring vertices, and (ii) over distorting the grains. Figure 4-4 shows an example of the random geometry generated.

4.2.2 Grain Boundary Deformation

The crystal orientation of a grain changes to its neighbor's within a finite grain boundary zone. This zone is highly disordered when compared with the material inside the grain, and hence is expected to be more compliant. The behavior of the grain boundary zone is not well understood presently. However, there are indications that grain boundary deformation does occur even at high strain rates where the polycrystal behaves linearly (see the references and arguments presented in Chapter 2 and the recent paper by Nickolayev and Schulson (1995)).

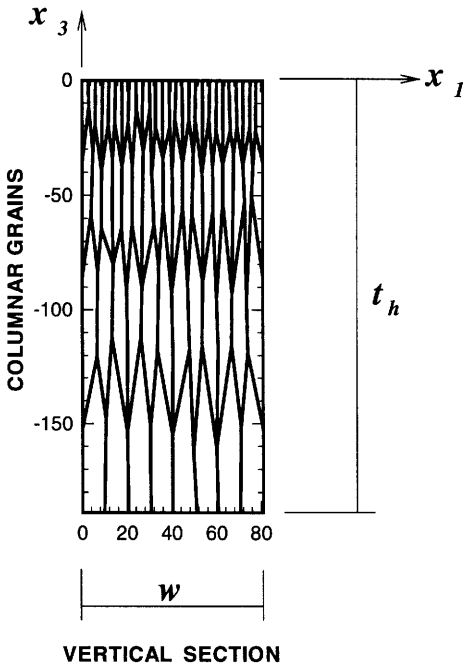

Figure 4-4: Ice plate with four grains of random geometry through the thickness.

Temperature, salinity, and porosity are expected to effect the grain boundary stiffness. At steady state, the temperature distribution within a floating ice sheet is expected to be linear, with the minimum temperature $T = T^*$ at the air- ice interface, and the melting temperature at the ice- water interface. The salinity profiles show some variability throughout the depth of the ice plate (see Weeks and Ackley (1986) for examples) but can be considered approximately constant.

The grain boundary thickness also effects the grain boundary stiffness. Chatterjee and Jellinek (1971) have developed an expression for the grain boundary thickness which is a function of both temperature and salinity. These authors predict the grain boundary to be of the order of microns. The dimensions of the grains, on the other hand, are of the order of millimeters. Hence, in this study, the grain boundaries are considered to have no thickness and an infinite normal stiffness, *i.e.* the grain boundary is rigid in the normal direction. In the tangential direction, however, the grain boundaries are assumed to have a finite shear stiffness. Thus, two points having the same coordinate but lying on either side of the grain boundary can transmit all the stresses normal to the grain boundary, but can transfer only a portion of the shear stress along the grain boundary.

Following the temperature distribution, the grain boundary shear stiffness, $s(x_3)$ is also assumed linear:

$$s(x_3) = s^* \left(1 + \frac{x_3}{t_h}\right) \tag{4.2}$$

where s^* is the maximum shear stiffness at the top of the ice sheet. Equation (4.2) assumes that at the ice- water interface the shear stiffness $s(-t_h) = 0$. In reality, at this interface it is expected that there is some (small) shear stiffness. Unfortunately, since the grain boundary shear modulus has not been measured, the shear stiffness, s^* is unknown. In this work, the effect of grain boundary

stiffness is investigated by considering a range of s^* values.

The shear stiffness distribution in Eq. (4.2) constitutes the base case. For comparison, a constant distribution, $s(x_3) = s^*$ is also investigated.

For convenience, a parameter χ called the fraction of shear stress transfered is introduced:

$$\chi = \frac{\bar{T}_3(s^*)}{\bar{T}_3(s = \infty)} \tag{4.3}$$

where $\bar{T}_3(s^*)$ is the average shear traction which causes an unit shear strain on the macroscopic/ polycrystal level, and is defined in Section 4.2.5. Note that the denominator corresponds to no grain boundary deformation. The fraction of shear stress transfer ranges from $\chi = 0-$ no shear stress transfered across the boundary, to $\chi = 1-$ no grain boundary deformation. In calculating χ, thin plates with only a single grain and an uniform distribution of $s(x_3)$ through the thickness are considered. The polycrystal contains a sufficient number of grains (at least 50) in the horizontal direction so that the grain orientations are smeared and have little effect on χ. It must be noted that although χ is independent of the plate thickness (single grain) and the number of grains considered[2], χ is dependent on grain size, d. For this reason, in calculating χ, the grain size is chosen the same size as in the top row of grains in thick (multi grain) plates.

4.2.3 Grain Elastic Properties

Polycrystalline $S2$ ice is transversely isotropic with the horizontal $x_1 - x_2$ plane being the plane of isotropy. The individual grains are also transversely isotropic, the basal plane being the plane of isotropy. The grain's orientation in space can be specified by the $c-axis$ (see Fig. 4-1). In $S2$ ice the $c-axes$ can be idealized as all lying in the horizontal $x_1 - x_2$ plane, but randomly oriented in this plane. Thus, by specifying ζ, the angle between the global x_1 and the $c-axes$, Fig. 4-1, the grain's orientation is specified. In reality, the $c-axes$ do not all lie perfectly on the horizontal plane; this is especially true in the top portion of the sheet. The randomness of ζ, provided a large enough sample of grains is considered, is what results in the isotropic polycrystalline behavior in the horizontal plane.

The individual grain's elasticity tensor in the global axes system, $\mathbf{C}_G$ is in general anisotropic; the components are given by the standard fourth rank tensor rotation:

$$C_{G\ ijkl} = Q_{im}Q_{jn}Q_{kr}Q_{ls}\ C_{g\ mnrs} \tag{4.4}$$

where $\mathbf{Q}$ are the direction cosines and C_g is the grain's elasticity tensor with $\zeta = 0$. The dynamic stiffness of a fresh water ice single crystal is given in Chapter 1, Eq. (1.1). The temperature dependence of the crystal elastic properties are given in Eq. (1.2). Note that between $0°C$ and $-20°C$ the variations in the elastic moduli of a single crystal are negligible.

[2]Provided these numbers are large enough so that the polycrystal is homogenized.

In sea ice brine collects in bubbles, or brine pockets, dispersed in a matrix of relatively fresh water ice. The effect of brine pockets on the elastic moduli of the grain can be estimated using, for example, the self consistent method (*e.g.* see Nemat-Nasser and Hori (1993)). The salinity of first year sea ice is of the order of 5 ppt (Weeks and Ackley (1986)). Thus the volume fraction of brine pockets is very small. The effect of brine pockets on the elastic properties of the ice crystal is expected to be small and is ignored.

The unit cell is subject to plane strain conditions with the normal strain components $\epsilon_2 = 0$. In forming the planar elastic stiffness tensor, all the components associated with x_2 in Eq. (4.4) are removed.

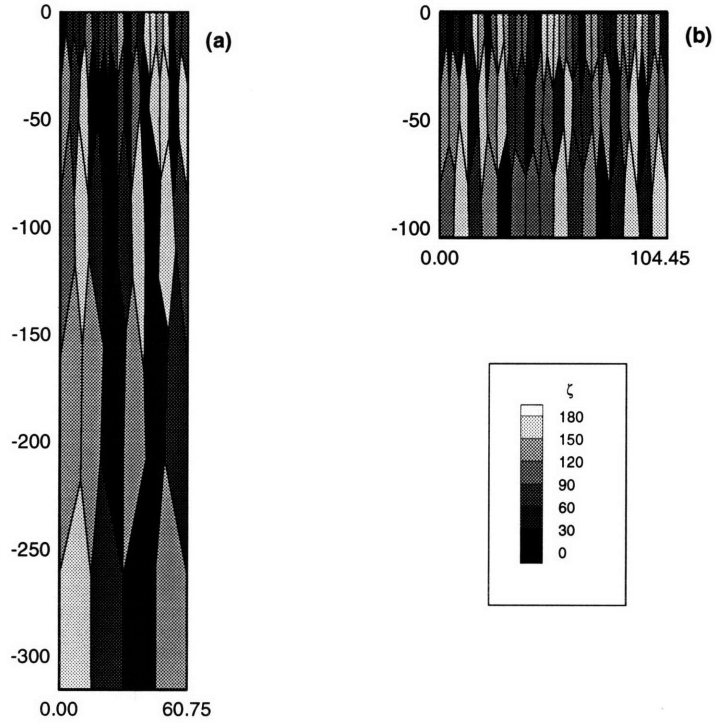

Figure 4-5: Distribution of grain orientations for two plates of thickness: (a) $t_h = 314mm$; and (b) $t_h = 104mm$.

In the numerical simulations, each grain is assigned a random orientations in the range $0° \leq \zeta \leq 180°$. Figure 4-5 shows two typical ice plates, one having three grains and the other five grains through the thickness; spatial distributions of ζ are shown.

4.2.4 Computational Model

Unit Cell

An unit cell model is used to study the transverse behavior of ice sheets of various thickness, t_h. As mentioned above, the unit cell eliminates the edge effects on $x_1 = 0$ and $x_1 = w$ (see Fig. 4-4). This allows to consider fewer grains in the x_1 direction than would be required if no

provisions were made for the boundaries. The size of the unit cell is specified by setting the number of grains in any one row. The number of grains in all other rows can then be determined from the geometric coarsening factor, f.

There has to be a sufficient number of grains within the unit cell to ensure homogeneous behavior. If all the grains were to have the same shape and the same orientation, *i.e.* same elastic properties, and there was little grain boundary deformation, then only a few grains would be required in the unit cell. However, due to randomness a convergence study of the size of the unit cell was conducted. In this study, the unit cell size was doubled in the x_1 direction until the band of homogenized shear moduli converged. Both regular and random geometries, as well as random ζ and all grains having $\zeta = 0$ were considered. Based on the study, the following cell sizes are used in the simulations: plates with two, three and four grains through the thickness have 32, 16, and 8 grains in the bottom row of the plate, respectively. Thicker plates all have four grains in the bottom row. These unit cell sizes are for the base case, $f = 1.5$. The unit cell for the case $f = 2$ all have five grains in the bottom rows (see Fig. 4-2b). The unit cells with grains of constant size through the thickness, $f = 1$, all have 15 grains in each row (see Fig. 4-2c).

The unit cell edges, $x_1 = 0$ and $x_1 = w$ are treated as follows. Coordinates of the grain triple points, located on $x_1 = 0$ and $x_1 = w$ are not randomized, and hence have the same x_3 coordinate– a requirement for the repetitive nature of the unit cell. To maintain compatability between neighboring cells, the deflection in the x_1 direction, u_1, must match:

$$u_1(x_1 = 0, x_3) = u_1(x_1 = w, x_3) \tag{4.5}$$

The deflection in the x_3 direction on the edges $x_1 = 0$ and $x_1 = w$ at depth x_3 depend on the shear stiffness of the grain boundary $s(x_3)$. Both grain boundaries at $x_1 = 0$ and $x_1 = w$ are assigned shear stiffness. These stiffnesses are in series when considering the junction between neighboring cells. Thus to maintain the overall boundary shear stiffness at $s(x_3)$, the grain boundary shear stiffness on $x_1 = 0$ and $x_1 = w$ has to be $2s(x_3)$.

Finite Element Model

The finite element method is used to solve for the stresses, strains and displacements in the heterogeneous grain assembly. Each grain is discretized into six quadratic isoparametric plane strain elements– two six node and four eight node elements. A typical discretization of the unit cell is shown in Fig. 4-6; also a discretized grain is shown separately. This discretization is applied to the cases $f = 1.5$ and $f = 2$. When $f = 1$, the width to length aspect ratio of the grains is larger, and the grains are discretized into nine quadratic elements. The elastic properties of each element is assigned according to the grain orientation, ζ. The grain stiffness is rotated into the global axes system using Eq. (4.4).

Two points lying on the grain boundary but belonging to different grains are constrained so that:

$$u_n^+ = u_n^- \tag{4.6}$$

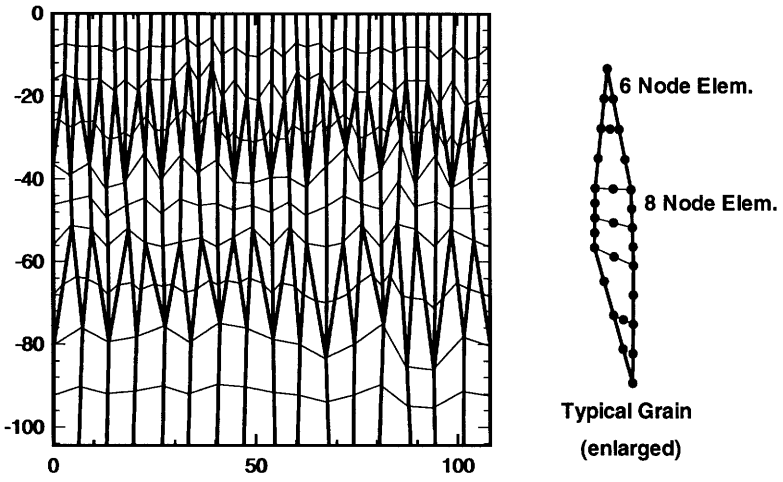

Figure 4-6: Typical discretization of the unit cell with quadratic elements. The discretization of a typical grain is also shown.

where u_n are the displacements in the direction normal to the grain boundary; the + and − refer to the two points on the grain boundary. This constraint between the node is enforced by the penalty method. Along the grain boundary, the two points belonging to the two grains are connected by a spring. The stiffness of the spring, s_k, is determined by lumping the grain boundary shear stiffness as follows:

$$s_k(x_3) = \int_l s(x_3)\ t\ \mathrm{d}x_t \tag{4.7}$$

where t is the thickness of the unit cell (set to $t = 1$), the integration is performed along the grain boundary x_t, over the tributary length, l, associated with the two nodes. The shear spring is oriented along the grain boundary.

To prevent rigid body modes, no displacements in the x_1 direction of the cell corners $(x_1; x_3) = (0; 0)$ and $(0; -t_h)$ are allowed.

The adequacy of the mesh is checked by comparing results from the mesh described above and a mesh consisting of three elements per grain– two six node and one eight node elements. The mesh convergence for all ice sheet thicknesses was checked, but only for the base case, $f = 1.5$. A number of s^* values was also considered. The homogenized transverse shear modulus, G, from the two meshes was compared. Results show that the *maximum* difference in G between the two meshes is only 2.5%. Thus the mesh with six elements per grain is acceptable.

4.2.5 METHOD OF HOMOGENIZATION

The homogenized transverse shear modulus, G, of the ice sheet can be obtained in two ways. In both methods G is defined as:

$$G = \frac{\bar{\Sigma}_3}{\gamma} \tag{4.8}$$

where $\bar{\Sigma}_3$ is the average shear stress and γ is the average engineering shear strain. In the first method, $\bar{\Sigma}_3$ is applied via tractions, and γ measured; in the second method, displacements and hence γ are applied and the required tractions measured.

The first method is more general and consists of three steps. First, tangential tractions of magnitude, Σ_3 are applied all along the top and bottom of the plate:

$$\begin{aligned} T_1(x_1, x_3 = 0) &= \Sigma_3 \\ T_1(x_1, x_3 = -t_h) &= -\Sigma_3 \end{aligned} \tag{4.9}$$

Also prescribed displacements of magnitude v^I are applied along the remaining boundaries:

$$\begin{aligned} u_3(x_1 = 0, x_3) &= -v^I \\ u_3(x_1 = w, x_3) &= v^I \end{aligned} \tag{4.10}$$

The unit cell boundary value problem is then solved by the finite element method and the average tangential tractions, $\bar{T}_3^I$ on sides $x_1 = 0$ and w are computed [3]:

$$\bar{T}_3^I = \frac{1}{t_h} \int_0^{t_h} T_3(x_1 = w, x_3) \mathrm{d}x_3 = \frac{\sum R_3(x_1 = w)}{t_h\, t} \tag{4.11}$$

where $T_3(x_1 = w, x_3)$ is the distribution of tangential tractions on edge $x_1 = w$, R_3 are the nodal reactions in direction x_3 and are summed over all the boundary $x_1 = w$.

The first step is then repeated but with prescribed displacements of magnitude v^{II}. The resulting average traction is $\bar{T}_3^{II}$.

Now, since this is a linear elastic problem, the solution from the first two steps can be scaled so that the magnitude of the average traction on edges $x_1 = 0$, and w match the top and bottom tractions, *i.e.* $\bar{T}_3 = \Sigma_3$. This sets up a pure shear condition on the unit cell. The displacement components, u_i, within the unit cell, corresponding to Σ_3 tangential tractions, are scaled from the two solutions:

$$u_i = u_i^I + (u_i^{II} - u_i^I)\, \frac{\Sigma_3 - \bar{T}_3^I}{\bar{T}_3^{II} - \bar{T}_3^I} \tag{4.12}$$

where u_i^I and u_i^{II} are the displacement solutions corresponding to the applied v^I and v^{II}, respectively. A line is then fit to the top surface of the ice plate using linear least squares. The slope of this line is the average shear strain γ corresponding to the applied shear tractions, Σ_3.

[3] From equilibrium the tractions on the two sides are equal and opposite in sign.

The second method is applicable only to unit cells with regular geometries. It consists of applying displacements to the boundaries of the cell:

$$\begin{aligned} u_3(x_1 = 0, x_3) &= -v \\ u_3(x_1 = w, x_3) &= v \\ u_1(x_1, x_3 = 0) &= 0 \\ u_1(x_1, x_3 = -t_h) &= 0 \end{aligned} \tag{4.13}$$

Thus $\gamma \approx 2v/w$ and $\Sigma_3 = \bar{T}_3$ is determined from Eq. (4.11). Note that this method predicts higher G than the first method when the geometry is random (non regular). In general, the grain facets do not form right angles with the top and bottom surfaces of the sheet. This, together with the u_1 boundary conditions in Eq. (4.13) lock the grain boundaries on the top and bottom surfaces, preventing any grain boundary deformation, and resulting in too high a G.

The advantage of the second homogenization method is that the problem has to be solved only once, as opposed to two times in the first method. The maximum difference in G calculated by the two methods for regular grain geometries is only 2%; the difference is maximum when the grain boundary is very flexible. Thus for computational efficiency, the second homogenization method is used when possible in the base case.

The homogenization methods were tested by setting $s(x_3) = \infty$, *i.e.* no grain boundary deformation, and assigning all grains the same isotropic elastic material properties. The computed homogenized G matched the isotropic material parameter input.

4.3 Results and Discussion of Numerical Simulations

This section presents and discusses the results from simulations of loading polycrystal ice plates of various thicknesses in shear. The effects of (i) plate thickness, (ii) grain coarsening, and (iii) grain boundary stiffness, on the transverse shear modulus are studied. Six different grain boundary stiffnesses are considered. These stiffnesses correspond to fractions of shear stress transfer of: $\chi = 0.08$, 0.31, 0.47, 0.9, and 1. Ice plate thickness ranges from 0.05 to $1.2m$. A minimum of two grains are considered through the plate thickness. The maximum grain dimension, g_{max}, at the top surface of the ice sheet in the cases $f = 1.5$ (Fig. 4-2a) and $f = 2$ (Fig. 4-2b) is taken as $3mm$. For the constant grain size case, $f = 1$, (Fig. 4-2c), the grains' maximum horizontal dimension is set to $g_{max} = 8mm$.

When the effect of (i) random grain geometry and (ii) random grain orientations, ζ, are studied, at least 30 different simulations are performed for each plate thickness. A new random parameter distribution for each simulation is obtained by choosing different initial seeds for the random number generator. The results are presented using error bars; the error bars show the bands formed by considering all the data, and the curves are plotted through the data averages.

4.3.1 Effect of Thickness on the Transverse Shear Modulus

The effect of ice plate thickness on the transverse shear modulus, G, is studied first by considering a regular hexagonal geometry for the base case, $f = 1.5$, and then randomizing the grain shapes. Figure 4-7 shows the results of G versus plate thickness, t_h for various grain boundary stiffnesses; the error bands show the effect of grain anisotropy. From this figure it is evident that the transverse shear modulus is strongly influenced by the thickness. For lower χ, G increase approximately 5 times as t_h increases from 0.05 to $1.2m$, and the increase is approximately linear. As the grain boundary stiffness increases, the effect of thickness becomes non linear. and the amount G grows with t_h decreases. For very high grain boundary stiffnesses, *i.e.* as $\chi \rightarrow 1$, the shear modulus becomes independent of thickness.

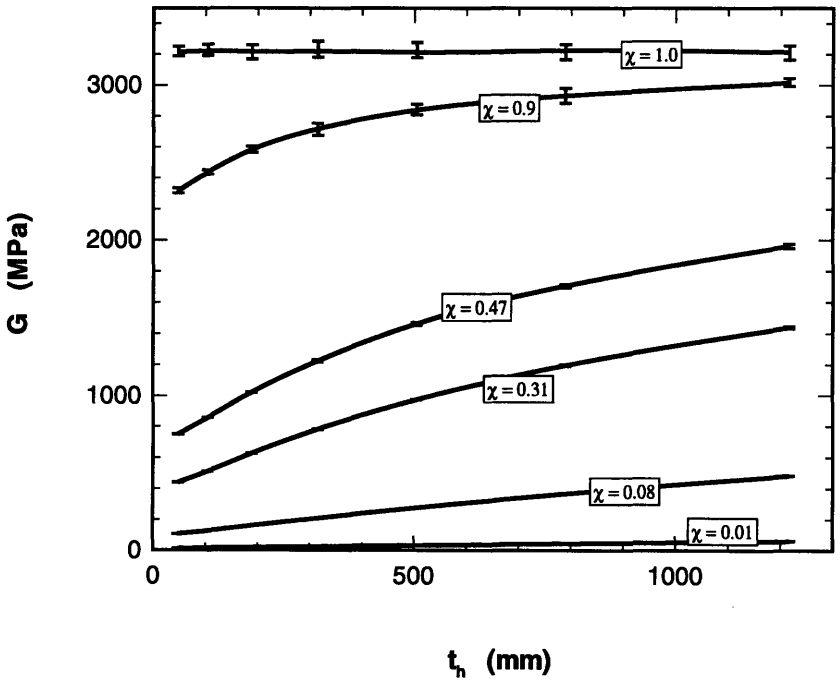

Figure 4-7: Variation of transverse shear modulus with plate thickness and fraction of shear stress transfered; regular grain geometry.

Nanthikesan and Shyam Sunder (1994) calculated the Voigt and Reuss upper and lower bounds on the transverse shear modulus. There was no grain boundary deformation ($\chi = 1$) in their model. They found G lies between 3.206 and $3.219GPa$. Their method assumed that there are an infinite number of grains and hence grain orientations, ζ. Figure 4-7 shows that when there is no grain boundary deformation, $\chi = 1$, the average $G = 3.218GPa$. The computed average shear modulus is within to the tight bounds calculated by Nanthikesan and Shyam Sunder (1994). It is important to note that the shear stiffness distribution $s(x_3)$ is linear (Eq. (4.2)) in Fig. 4-7. However, when $\chi = 1$, $s^* = \infty$, and there is no grain boundary deformation throughout the

plate.[4] This is confirmed below when a constant grain boundary stiffness $s(x_3) = s^*$ is considered.

The bands which are caused by considering random grain orientations within the horizontal plane, ζ, are shown in Fig. 4-7. For the lower fractions of shear stress transfer, χ, the bands are as narrow as the width of the curves. In general the effect of grain anisotropy is small; the maximum band width is only 3% of the corresponding average G. Grain anisotropy has its maximum effect when there is no grain boundary deformation. Theses results agree with the observations made in the previous chapter on the elastic properties of polycrystalline ice in the horizontal plane.

Two facts point to a sufficient numbers of grains within the unit cells. First, when $\chi = 1$ the bands due to grain anisotropy are narrow. Second, G is approximately constant for all plate thicknesses.

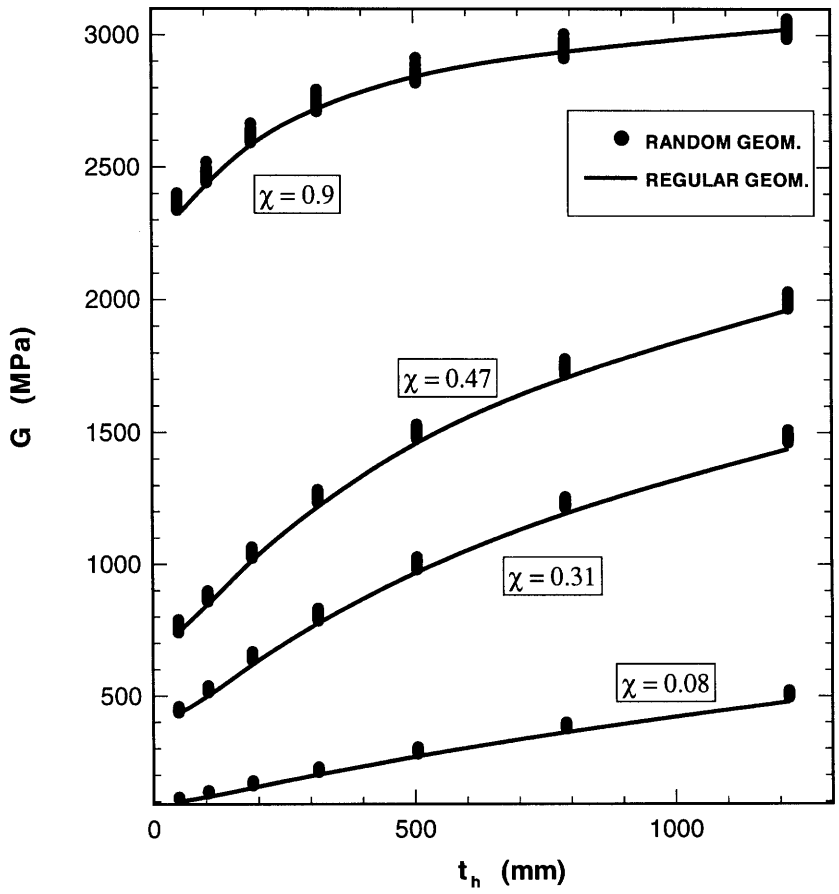

Figure 4-8: Variation of transverse shear modulus with plate thickness; random grain geometry.

The results of G versus thickness when the grain shapes and orientations are random are presented in Fig. 4-8. The average values of G from the regular grain geometries of Fig. 4-7 are plotted for comparison. Randomizing the grain geometry causes extra interlock between the grains. Thus the regular geometry curves provide the lower bound for G estimates when there is grain boundary

[4]Numerically, an infinitly stiff grain boundary is modeled by the penalty method.

deformation (low χ). Note that as G increases so the effect of the grain shape diminishes; at high enough G the bands produced by grain anisotropy and by random grain geometry and anisotropy are of the same thickness (also in agreement with the previous chapter). In Fig. 4-8 the maximum increase in G is 4.8 times. The bands formed by random grain shapes can be as high as 6% of the corresponding average value. The effect is greatest for thin plates and when χ is low. Since the results from random and regular geometries are comparable, in all subsequent simulations, the unit cells are made up of grains of regular geometry.

4.3.2 Effect of Grain Coarsening on the Shear Modulus

The effect of grain coarsening on the transverse shear modulus G is studied by considering three grain geometries: Fig. 4-2a, b, and c, corresponding to coarsening factors $f = 1.5$, 2, and 1. The results from the simulations of these three cases are shown in Fig. 4-9a, b, and c.

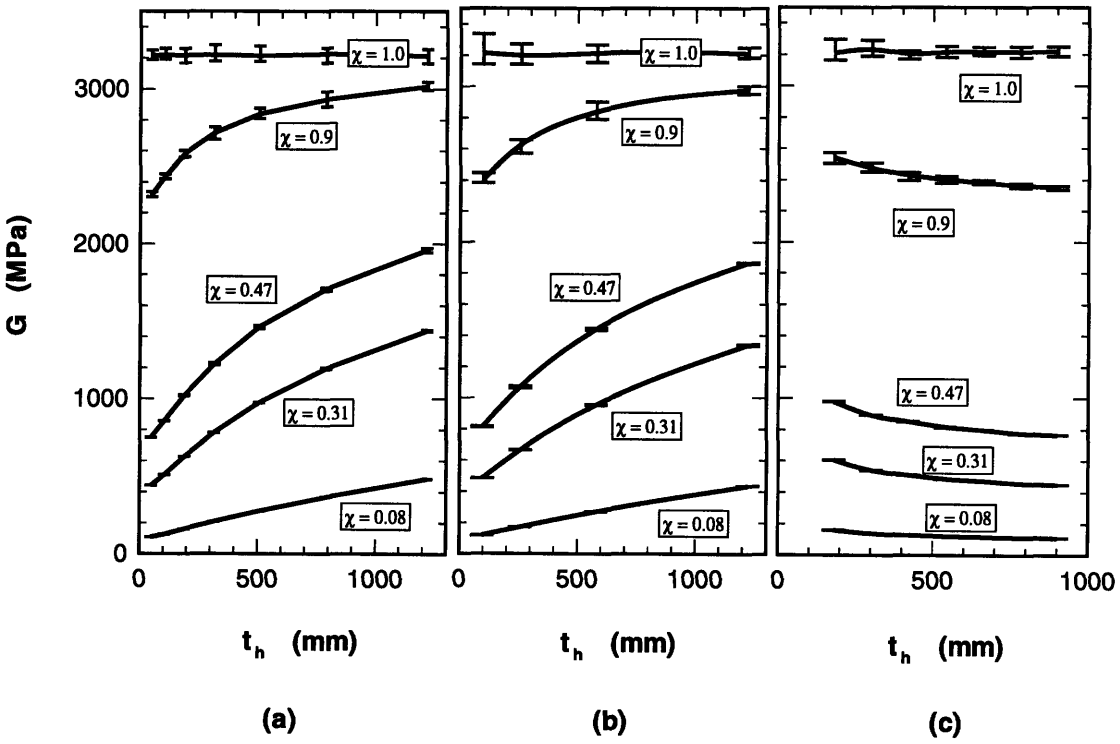

Figure 4-9: Variation of transverse shear modulus with plate thickness for three different grain coarsening factors: (a) $f = 1.5$; (b) $f = 2$; and (c) $f = 1$.

The rapid grain coarsening case, $f = 2$, and the base case, $f = 1.5$, Fig. 4-9a and b, show similar increases in the transverse G with plate thickness. The rates of increase for the same χ are also similar. The effect of random grain orientations on the bands of G for $f = 1.5$ and 2 are also comparable. The relatively wide elastic anisotropy bands for the thinner plates for the case $f = 2$ when $\chi = 1$ (Fig. 4-9b), indicates that there might be too few grains in this case.

When there is no grain coarsening, $f = 1$ Fig. 4-9c, and all the grains in the ice plate have the same width, an interesting behavior is observed. As the ice plate increases in thickness, the homogenized shear modulus G *decreases* when $\chi < 1$. The decrease is not great: Fig. 4-9c shows a maximum decrease of 45% as the plate t_h increases from 180 to $900mm$. The maximum percentage decrease occurs for the lowest χ. This decrease is in marked contrast to the increase in G for $f > 1$ cases. As noted above, the $f = 1$ is a fictitious case; it is included to underline the fact that grain coarsening (observed in reality) is required to have an increasing G with plate thickness.

4.3.3 Effect of Grain Boundary Stiffness on the Shear Modulus

So far only a linear distribution of grain boundary stiffness has been considered (the base case). The variation of G with thickness and a constant grain boundary stiffness, $s(x_3) = s^*$, is plotted in Fig. 4-10. The characteristic increase in G with t_h is seen. Since the grain boundaries are stiffer here for $x_3 < 0$ than in the base case, the G corresponding to a particular χ and t_h is greater than in the base case (Fig. 4-7). The amount by which the two cases differ diminishes with increasing χ. As the grain boundary stiffens, so the elastic properties of the grain become the dominant contribution to the homogenized G. When the grain boundary stiffness is constant through the thickness and there is no grain boundary deformation ($\chi = 1$), the average G is independent of thickness and is equal to $3.216GPa$; the same value as in the base case.

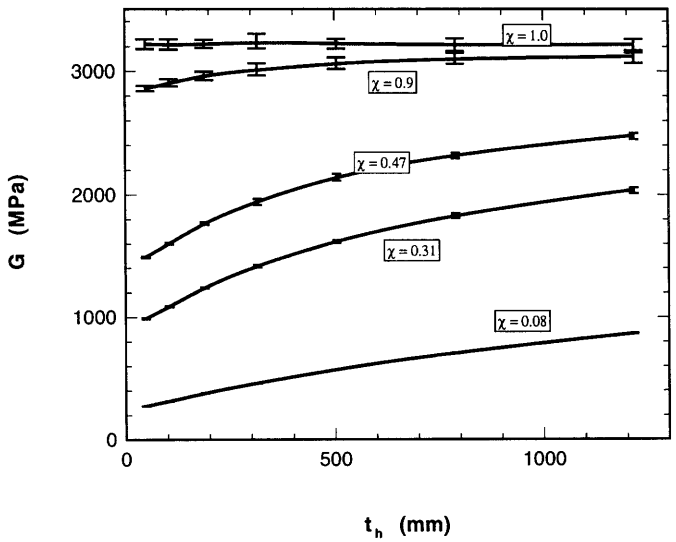

Figure 4-10: Variation of transverse shear modulus with plate thickness and a constant grain boundary shear stiffness, $s(x_3) = s^*$.

The grain boundary stiffness is expected to be influenced significantly by temperature. If the temperature at the air- ice interface changes, then so does s^*; lower temperatures correspond to higher s^*. The variation of the transverse shear modulus G with s^* is shown in Fig. 4-11 keeping

the plate thickness constant. Three thicknesses are considered: the plates have 3, 5 and 7 grains through the thickness. A linear variation in $s(x_3)$ through the ice sheet is assumed. Unfortunately, the relationship between $s(x_3)$ and temperature is not known, and the horizontal axis of Fig. 4-11 cannot be related to the air temperature quantitatively. Note that temperature effects on G all come from the grain boundary $s(x_3)$ since the grain's elastic properties are only mildly effected by temperature (see the empirical Eq. (1.2) in Chapter 1).

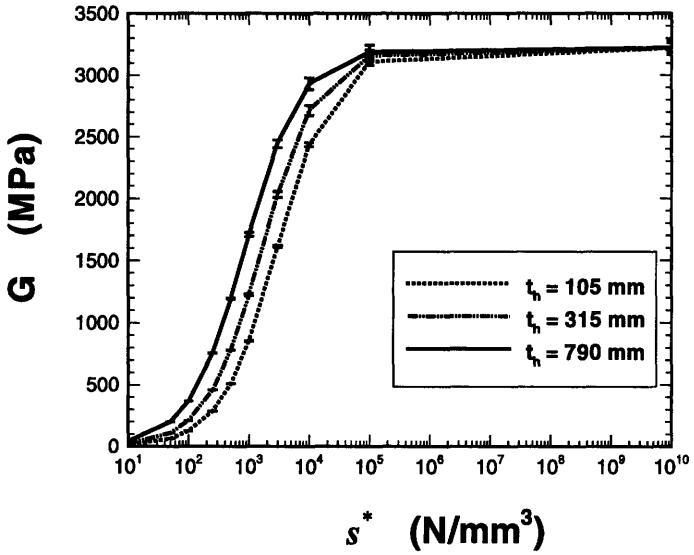

Figure 4-11: Variation of transverse shear modulus with grain boundary shear stiffness parameter s^* for plates of different thickness.

Figure 4-11 shows that G has a large range of values. For ambient temperatures close to the melting point, s^* is expected to be very low and hence G is low. The floating plate will deform predominantly in shear. In the limiting case of free grain boundary sliding ($\chi = 0$) and if grain interlock is ignored, $G = 0$. As the air temperature falls, s^* increases and the homogenized G increases rapidly. The shear modulus starts to asymptote as $\chi = 1$ is approached. Thus for low enough temperatures, irrespective of plate thickness, a floating ice sheet will deform predominantly in bending. These results are consistent with observations referenced in Kerr (1976)[5]: ice plates at low temperatures deflect in bending; at high temperatures the ice plates deflect in shear.

4.4 Conclusion

This chapter examines the effect of ice plate thickness and grain boundary stiffness on the transverse shear modulus. Results show that when the stiffness of the grain boundaries is low, the homogenized shear modulus can increase approximately five times as the plate thickness increases from 0.05 to $1.2m$. As the fraction of shear stress transfered across the grain boundary increases

[5]Kerr (1976) references deal thick plates, *i.e.* with plates with multiple grains through the thickness

so too does the shear modulus. When the grain boundaries transfer all the shear stresses, *i.e.* no grain boundary deformation, the macroscopic shear modulus is independent of thickness.

Simulations show that if there is no grain coarsening, *i.e.* constant grain size throughout the plate thickness, the macroscopic shear modulus decreases. Since grain coarsening is observed in reality, the transverse shear modulus of the plate is expected to increase with thickness. Further, increasing the shear stiffness of the grain boundary, as expected to occur with falling ambient temperature, results in rapid increasing of the transverse shear modulus G, until an asymptote is reached. The asymptote corresponds to $G = 3.22GPa$ and to no grain boundary deformation.

These results have several important implications for the behavior of floating ice plates. First, thin plates are more prone to shear deformation. At high temperatures, and/ or high salinity or porosity, shear deformation in plates of all thicknesses cannot be ignored. In the past, the horizontal Young's modulus of thin model ice plates has been calculated based on bending deformation only. This resulted in unrealisticly low Young's moduli (see Timco (1981) for discussion). Including shear deformation and bending deformation, increases the in-plane Young's modulus significantly– for details see the next chapter. Second, any macroscopic fracture calculations of ice plates has to consider not only bending energy but also shear energy. In the past only fracture due to flexure was considered.

REFERENCES

[1] Chatterjee, A.K. and Jellinek, H.H.G. , (1971), Calculation of Grain Boundary Thickness in Polycrystalline Ice of Low Salinity, *Journal of Glaciology*, Vol. 10, pp. 293- 297.

[2] Elvin, A.A., Shyam Sunder, S., (1995), Microcracking Due To Grain Boundary Sliding in Polycrystalline Ice Under Uniaxial Compression, *Acta Mettalurgica et Materialia*, In Press.

[3] Gow, A.J., and Ueda, H.T., (1989), Structure and Temperature Dependence of the Flexural Properties of Laboratory Freshwater Ice Sheets, *Cold Regions Science and Technology*, Vol. 16, pp. 249- 269.

[4] Gow, A.J., (1995), *Personal Communication.*

[5] Hill, R., (1952), The Elastic Behavior of a Crystalline Aggregate, *Proc. Phys. Soc.*, A 65, 349.

[6] Kerr, A.D., (1976), The Bearing Capacity of Floating Ice Plates Subjected to Static or Quasi-Static Loads, *Journal of Glaciology*, Vol. 17, p. 229- 268.

[7] Meese, D., A., (1995), *Personal Communication.*

[8] Michel, B., and Ramseier, R. O., (1971), Classification of River and Lake Ice, *Canadian Geotechnical Journal*, Vol. 8, pp. 36-45.

[9] Nanthikesan, S., and Shyam Sunder, S. (1994). Anisotropic Elasticity of Polycrystalline Ice I_h, *Cold Regions Science and Technology*, Vol. 22, pp. 149- 169.

[10] Nemat-Nasser, S. and Hori,M., (1993), *Micromechanics: Overall Properties of Heterogeneous Materials*, Elsevier, Amsterdam.

[11] Nickolayev, O.Y., and Schulson, E.M., (1995), Grain Boundary Sliding and Across-Columnar Cracking in Columnar Ice, *Philosophical Magazine Letters*, In Press.

[12] Reuss, A.Z., (1929), Berechnung der Fliebgreneze von Mischkristallen auf Grund der Plastizitatsbedingung fur Einkristalle, *Z. Angew. Math. Mech.*, 9, 49.

[13] Timco, G.W., (1981), On the Test Methods for Model Ice, *Cold Regions Science and Technology*, Vol. 4, pp. 269- 274.

[14] Voigt, W., (1910), *Lehrbuch Der Krystallphysik*, Feubner., Berlin.

[15] Weeks, W.F., and Hamilton, W.L., (1962). Petrographic Characteristics of Young Sea Ice, Point Barrow, Alaska, *The American Mineralogist*, Vol. 47, pp. 945-961.

[16] Weeks, W.F., and Ackley, S.F., (1986), The Growth, Structure, and Properties of Sea Ice, *Geophysics of Sea Ice*, ed. N. Untersteiner, pp. 9-146.

[17] Wei, Y., Johnston, M., and Dempsey, J.P., (1995), A Grain Multiplication Mechanism for the Formation of Transition Zones in First Year Sea Ice, *Cold Regions Science and Technology*, Vol. 23, pp.367- 375.

Chapter 5

EFFECT OF TRANSVERSE SHEAR DEFORMATION ON ELASTIC BEHAVIOR OF ICE PLATES

ABSTRACT

The elastic deflection of an ice sheet due to bending and shear deformation is considered. The in- plane Young's modulus and the transverse shear modulus are calculated by non- linear least squares fit of plate deflection data. Results show that thin ice plates and plates close to their melting temperature behave predominantly in shear; thick, cold plates deform in bending. The Young's modulus of thin model ice sheets, estimated using the bending and shear theory, is more than an order of magnitude greater than calculated previously, and hence is more realistic.

5.1 INTRODUCTION

Ice plates loaded by static loads but for short duration exhibit elastic behavior. Previously, the plate was assumed to deform either in bending or in shear. The bending assumption is based on ice plate deflection observations of Bernshteyn (1929), while the purely shear behavior is based on the field observations of Zubov (1945). These two behaviors result in different governing differential equations and hence require different elastic moduli. Kerr (1976) concluded that ice plates close to their melting temperature exhibit shear behavior, while colder plates deform predominantly in bending.

In the previous chapter it has been shown that the homogenized transverse shear modulus can increase significantly not only with temperature, but with the thickness of the ice plate as well. The increase in the shear modulus is due to two factors: (i) grain boundary deformation, and (ii) grain coarsening typically observed through the thickness of the plate. The variation in the shear modulus implies that thin ice plates are more susceptible to shear deformation than thick plates. Thin ice plates are defined as having a few grains through their thickness.

An *in situ* method for determining the average elasticity moduli of a floating ice plate first requires the measurement of deflections due to a prescribed transverse load. The average elastic moduli are then calculated by fitting the load- deflection data with analytical deflection solutions of an elastic plate resting on an elastic foundation. If the plate is assumed to deform in bending, then an average in- plane Young's modulus is calculated. An average transverse shear modulus is obtained if the solution to the shear equation is used. The Young's modulus of floating ice plates has been calculated in this way by Bernshteyn (1929), Timco (1981), Sodhi *et al.* (1982), Kerr and Haynes (1988) among many others. The transverse shear modulus has been obtained by Shmatkov (1968) and Tinawi and Gagnon (1984).

Timco (1981), commenting on the Young's modulus calculated for thin floating model urea ice sheets using the method described above, expressed two important concerns. Namely: (i) the Young's modulus can be more than an order of magnitude smaller than $1.3GPa$– a lower limit for the dynamic Young's modulus he postulates; and (ii) the Young's modulus from deflection data far away from the loading is higher than the modulus obtained by fitting deflections at the loading.

The aim in this chapter is to account for both bending and shear deformation in the deflection of floating ice plates. It will be shown that by incorporating shear behavior, an answer is provided to the concerns raised by Timco (1981).

The organization of this chapter is as follows. The governing differential equations used in the past for bending and shear plates resting on an elastic foundation are presented in Section 5.2. The solution for a point load is also given in this section. The deflection due to bending and shear deformation is presented in Section 5.3. The method of obtaining both the Young's modulus and transverse shear modulus using least squares fit is described in Section 5.4. The two elastic moduli are then obtained for a number of thin and thick ice plates in 5.4.1 and 5.4.2. When considering thin plates, both an analytic treatment and the finite element method are used.

5.2 Deformation of a Floating Ice Plate– Historical Bacground

A floating ice plate responding to short duration transverse loads has been modeled as an elastic plate resting on an elastic foundation. Two independent plate behaviors have been considered; namely, the plate was assumed to deform either in bending or in shear. The average Young's modulus appears in the bending plate equations, while the shear plate equations contain an average transverse shear modulus. This section presents the governing differential equations associated with

these two assumed behaviors and discusses the resulting solutions. In what follows the loading configuration is such that the problem is axisymmetric and hence polar coordinates are used; see Fig. 5-1. Unless otherwise noted, the floating ice sheet is assumed to be of infinite extent and subject to a point load.

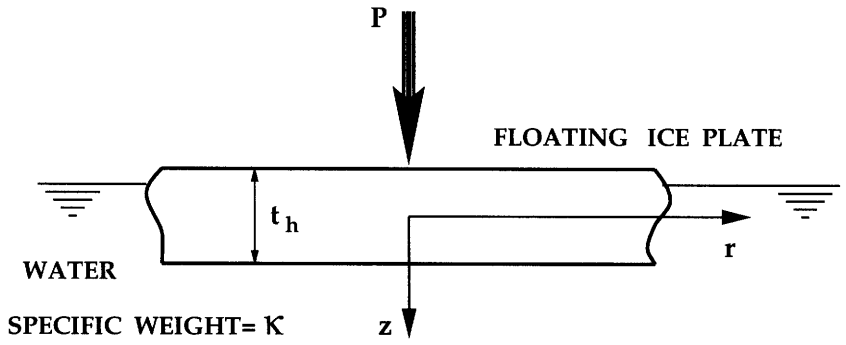

Figure 5-1: Schematic of floating ice plate.

5.2.1 Deformation Due To Bending Stresses

The deflected shape of a loaded ice sheet was measured by Bernshteyn (1929). This data showed that the plate deformed primarily in bending. Since then the classical Kirchoff bending plate theory has been applied extensively to the deformation of floating ice sheets of various thicknesses (see *e.g.* Wyman (1950), Kerr (1976), Sodhi *et al.* (1982), Kerr and Haynes (1988), among many others). In the classical bending theory, besides the assumption of small deformations, there is another assumption of plane cross sections normal to the undeformed neutral surface remaining plane and normal to the deformed neutral surface. The latter condition is satisfied if the plate thickness is small compared with the characteristic length. For an isotropic material the resulting governing differential equation of a bending plate resting on an elastic foundation is (see Timoshenko and Woinowsky-Krieger (1959) for derivation and historical references):

$$D\,\nabla^4 w + \kappa w = q \tag{5.1}$$

where w is the transverse (or vertical) deflection. ∇^4 is the biharmonic operator, q is the transverse distributed load, and κ is the foundation stiffness. For the ice plate the foundation stiffness is due to buoyancy and hence κ is equal to the specific weight of water. The flexural rigidity, D, is given by:

$$D = \frac{E t_h^3}{12(1-\nu^2)} \tag{5.2}$$

where E is the average in-plane Young's modulus, t_h is the ice plate thickness, and ν is the in-plane Poisson ratio.

In general the Young's modulus can vary through the thickness of the ice plate. for this reason, the ice sheet was modeled as a layered bending plate by Selvadurai (1984) with each layer

having its own isotropic E; this reference considered two distributions of E with depth. Kerr and Palmer (1972), on the other hand, have shown that Eq. (5.1) is still applicable even if E varies with depth (and hence the neutral surface is not at $t_h/2$) provided an appropriately averaged flexural rigidity is used instead of D in Eq. (5.2).

For example, if a floating bending plate is subject to a point load, P, at $r = 0$, the boundary conditions on Eq. (5.1) are:

$$\begin{aligned} w = \frac{dw}{dr} = M = Q = 0 \qquad &\text{at} \qquad r = \infty \\ Q = \lim_{r \to 0} \left(\frac{P}{2\pi r} \right), \frac{dw}{dr} = 0 \qquad &\text{at} \qquad r = 0 \end{aligned} \tag{5.3}$$

where Q is the shear force/unit length and M is the bending moment/unit length. The solution to Eq. (5.1) with the boundary conditions in Eq. (5.3) is (Timoshenko and Woinowsky- Krieger (1959), Wyman (1950)):

$$w(r) = \frac{-P\lambda^2}{2\pi D} \operatorname{Kei}_0 \left(\frac{r}{\lambda} \right) \tag{5.4}$$

where $\operatorname{Kei}_0(x) = Im(K_0(x \exp^{i\pi/4}))$ and K_0 is the modified Bessel function of the second kind of order 0. The characteristic length λ is defined as:

$$\lambda = \sqrt[4]{\frac{D}{\kappa}} \tag{5.5}$$

Kerr and Haynes (1988) have shown that result obtained form the point load solution is similar to the solution when the loading is distributed uniformly over: (a) circular area, or (b) circumference of a circle (ring load).

5.2.2 Deformation Due To Shear Stresses

Zubov (1945) suggested that ice plates deflect predominantly in shear with negligible bending deformation. The deflection shape measured by Shmatkov (1968) seem to support this suggestion. The assumption that all the deformation is due to shear implies that the transverse shear strain γ_{rz} is:

$$\gamma_{rz} = \frac{dw}{dr} \tag{5.6}$$

The equilibrium condition for the shear plate is:

$$\frac{d}{dr}(Qr) = -\kappa w r + qr \tag{5.7}$$

where Q is the shear force per unit circumferential length and is defined as:

$$Q = \int_0^h \tau_{rz} dz \tag{5.8}$$

where τ_{rz} is the transverse shear stress. If the elastic constitutive law $\tau_{rz} = G\gamma_{rz}$, where G is the average transverse shear modulus of the plate, is used in Eq. (5.8), with the assumption Eq. (5.6), and the result is substituted into Eq. (5.7), then the governing differential equation for a shear plate on an elastic foundation is obtained:

$$\frac{d^2w}{dr^2} + \frac{1}{r}\frac{dw}{dr} + \frac{1}{Gt_h}\kappa w = q \quad \text{or} \quad Gt_h \nabla^2 w + \kappa w = q \tag{5.9}$$

The example of a point load, P at $r = 0$ acting on a shear plate is considered now. This problem has the same boundary conditions as in Eq. (5.3), except for the specification on M. The solution of Eq. (5.9) gives:

$$w(r) = \frac{P}{2\pi G t_h} \, \mathrm{K}_0\left(\sqrt{\frac{\kappa}{Gt_h}}\, r\right) \tag{5.10}$$

Note that Eq. (5.10) is non linear in G. Using an appropriate shear modulus G, Shmatkov (1968) showed that Eq. (5.10) fits the measured deflected shape of a floating ice plate close to the melting temperature.

5.3 Deformation Due To Bending And Shear Stresses

The experimental evidence described above, suggests that ice plates have two regimes of short duration deformation. At temperatures close to the melting point the ice plate deforms in shear; at lower temperatures, the plate behaves predominantly in bending. Besides this thermal influence on the ice plate, the simulations conducted in the previous chapter also indicate that the transverse shear modulus can increase with plate thickness. Figure 5-2 shows the variation of the average

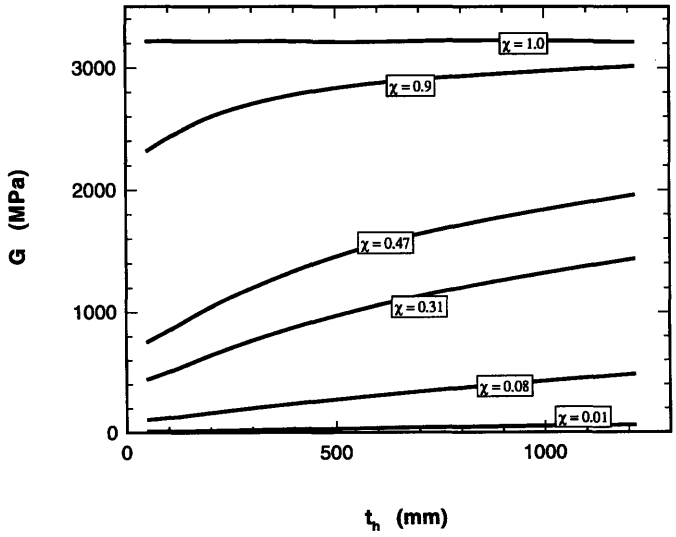

Figure 5-2: Variation of homogenized transverse shear modulus with plate thickness and with fraction of shear stress transfered across the grain boundary.

homogenized transverse shear modulus with thickness and with the fraction of shear stress transfer across the grain boundary, χ. The fraction of shear transfer can vary from $\chi = 1$ where there is no grain boundary deformation to χ close to 0 where there is almost no shear stress transfer across the grain boundaries. χ is believed to be related to temperature, with lower temperatures corresponding to higher χ. Figure 5-2 indicates that thinner plates, and plates at higher temperatures have lower G than thicker plates and plates at lower temperatures. Thus thin plates and plates at high temperatures will deform primarily in shear, while thick and cold ice plates will deform in bending. It is postulated that ice plates in between these two limiting conditions deflect due to bending and due to shear.

Plates that exhibit both bending and shear deformations are usually referred to as thick plates. Reissner's plate theory can be used to describe thick plate behavior. Following the derivation of Frederick (1956) and Naghdi and Rowley (1953) of Reissner's thick plates on elastic foundations, the governing differential equation is:

$$D\,\nabla^4 w + \frac{D}{Gt_h}\nabla^2(q - \kappa w) + \kappa w = q \tag{5.11}$$

In Eq. (5.11), the shear deformation is not due to the thickness of the ice plate as in the standard Reissner plate theory, but due to the reduced transverse shear modulus, G. This reduction in G is due to grain boundary deformation and due to grain coarsening (see previous chapter). In general the ice plate is not isotropic, and hence the standard relationship between G and E (and hence between G and D) does not hold; thus

$$G \neq \frac{E}{2(1+\nu)} \tag{5.12}$$

Thus Eq. (5.11) holds for all plates which exhibit shear deformation even geometrically thin ones.

Considering once again a floating ice plate subject to a point load, P, at $r = 0$, the boundary conditions on Eq. (5.11) are:

$$\begin{aligned} w = \psi = M = 0 \qquad &\text{at} \qquad r = \infty \\ \psi = 0 \qquad &\text{at} \qquad r = 0 \\ Q = \lim_{r\to 0}\left(\frac{P}{2\pi r}\right) & \end{aligned} \tag{5.13}$$

where ψ is the rotation of a line initially normal to the neutral surface and is given by:

$$\psi = \frac{dw}{dr} - \frac{Q}{Gt_h} \tag{5.14}$$

Defining two parameters, α and β:

$$\begin{aligned} cos(\alpha) &= \frac{\sqrt{D\kappa}}{2Gt_h} \\ \beta^2 &= \frac{\sqrt{D\kappa}}{2Gt_h} + \sqrt{\frac{D\kappa}{4(Gt_h)^2} - 1} \end{aligned} \tag{5.15}$$

the solution to Eq. (5.11) with the boundary conditions in Eq. (5.13) is:

If $\frac{\sqrt{D\kappa}}{2Gt_h} \leq 1$:

$$w(r) = \frac{P}{2\pi}\left[\frac{1}{Gt_h}\frac{\sqrt{D\kappa}}{\sqrt{4(Gt_h)^2 - D\kappa}} - \frac{\lambda^2}{D}\frac{2Gt_h}{\sqrt{4(Gt_h)^2 - D\kappa}}\right] Im(K_0\left(\frac{r}{\lambda}e^{i\alpha/2}\right)) + \frac{P}{2\pi Gt_h}\mathrm{Re}(K_0\left(\frac{r}{\lambda}e^{i\alpha/2}\right))$$

If $\frac{\sqrt{D\kappa}}{2Gt_h} > 1$:

$$w(r) = \frac{P}{2\pi}\frac{\beta^2\lambda^2}{1-\beta^4}\left[\left(\frac{1}{D} - \frac{\kappa}{(Gt_h)^2} + \frac{1}{\lambda^2\beta^2}\frac{1}{Gt_h}\right)K_0\left(\frac{r}{\lambda}\beta\right) + \left(-\frac{1}{D} + \frac{\kappa}{(Gt_h)^2} - \frac{\beta^2}{\lambda^2}\frac{1}{Gt_h}\right)K_0\left(\frac{r}{\lambda}\frac{1}{\beta}\right)\right] \tag{5.16}$$

Note that the solution of a shear and bending plate is not a simple superposition of the solutions from a bending plate (Eq. (5.4)) and a shear plate (Eq. (5.10)). This is due to the shear and bending plate resting on an elastic foundation being structurally indeterminate.

When the transverse shear modulus is high, *i.e.* $(Gt_h)^2 \gg D\kappa$, expected in thicker plates at lower temperatures, the solution in Eq. (5.16) tends to the bending plate solution, Eq. (5.4). At the other limit when $(Gt_h)^2 \ll D\kappa$, *i.e.* when G is very low, Eq. (5.16) tends to the shear plate solution, Eq. (5.10). It is possible that by varying the ice plate temperature and/ or thickness, G can change so much (see Fig. 5-2) that the dominant plate behavior goes from shear only, to shear and bending, to bending only.

5.4 Elastic Moduli From Transverse Data

The static elastic moduli of floating ice plates have been determined from deflection measurements due to applied transverse loads. The loading was applied over a sufficiently short duration to ensure linear elastic behavior of the plate. The plate was assumed to behave either in bending or in shear. The elastic modulus was calculated from the measured data and the appropriate elastic solution. If a bending plate was assumed, then the average in- plane Young's modulus was calculated using Eq. (5.4). If a shear plate was assumed then the average transverse shear modulus was calculated using Eq. (5.10).

Here the ice plate is assumed to have both shear and bending deformation. Hence both the in-plane E and the transverse G of the plate can be determined. The moduli E and G are chosen so that the solution to Eq. (5.16) best fits the measured load- deflection data. The optimum E, G pair is chosen by the method of least squares. The sum of the square of the error e^2 between the analytical deflected shape $w(r)$, given by the solution of Eq. (5.11), and the measured deflection at distance r_i, $w^M(r_i)$ is set up:

$$e^2 = \sum_{i=1}^{N}(w(r_i) - w^M(r_i))^2 \tag{5.17}$$

where the summation is carried over the N measured points. The error is then minimized by:

$$\nabla e^2 = \mathbf{0} \qquad or \qquad \left[\frac{\partial e^2}{\partial E} \quad \frac{\partial e^2}{\partial G}\right]^T = \mathbf{0} \tag{5.18}$$

In general Eq. (5.18) results in two non linear simultaneous equations in E and G. These equations are solved by Newton- Raphson iteration.

In the remainder of this section, the average elastic moduli of thin and thick plates are calculated from transverse load and deflection data. The term "thin plate" refers to a plate with only a few grains through the thickness of the ice sheet. As noted above, depending on the temperature, both thin and thick plates can exhibit shear deformation.

5.4.1 Thin Plates

The calculation of the Young's modulus and the transverse shear modulus requires deflection measurements at several points on the ice sheet at different distances form the load. Such data was measured by Tinawi and Gagnon (1984) and by Sodhi *et al.* (1982). The moduli of the plates tested in these references are calculated here.

Simply Supported Circular Plate Loaded By Ring Load

Tinawi and Gagnon (1984) tested thin circular plates of columnar grained $S2$ sea ice resting only on a ring support (no elastic foundation $\kappa = 0$) and loaded by a ring load. These authors tested several plates at temperatures ranging from $-5°C$ to $-30°C$. Only the loading which was applied in less than 100 seconds is considered here. The solution of a plate deforming in bending and shear, simply supported at $r = L/2$ and subject to a ring load ($r = b/2$) of total magnitude P is (Timoshenko and Woinowsky-Krieger (1959)):

$$w(r) = \frac{Pb}{8D}\left[(r^2+\frac{b^2}{4})\ln\left(\frac{2r}{L}\right)+\left(\frac{L^2}{4}-r^2\right)\frac{L^2(3+\nu)+b^2(\nu-1)}{2L^2(1+\nu)}\right]- \frac{Pb}{2Gt_h}\ln\left(\frac{2r}{L}\right) \quad if \quad r \geq b/2$$

$$w(r) = \frac{Pb}{8D}\left[(r^2+\frac{b^2}{4})\ln\left(\frac{b}{L}\right)+\left(L^2-b^2\right)\frac{L^2(3+\nu)-4r^2(1-\nu)}{8L^2(1+\nu)}\right]- \frac{Pb}{2Gt_h}\ln\left(\frac{b}{L}\right) \quad if \quad r < b/2 \tag{5.19}$$

Note that these equations are linear in $1/E$ and $1/G$. Hence the best fit of the data is obtained by *linear* least squares. The moduli are calculated by substituting Eq. (5.19) into Eq. (5.17) and minimizing the error with Eq. (5.18). A Poisson ratio of $\nu = 0.33$ is assumed.

The results for two plates at $-5°C$ and $-10°C$ are summarized in Table 5.1. The corresponding best fit deflected shapes together with the data of Tinawi and Gagnon (1984) are plotted in Fig. 5-3. The contribution of bending (first term in Eq. (5.19)) and shear (second term in Eq. (5.19)) deflections to the total deflection are also plotted. As the temperature drops, the average Young's modulus of the plate remains approximately constant (falling only by 9%) but the shear modulus increases 3.6 times. The increase in G is expected to be due to the stiffening of the grain boundary.

$T\ (°C)$	$P\ (N)$	$T_h\ (mm)$	$E\ (GPa)$	$G\ (MPa)$	Coeff. of Correlation
-5	4577	107	3.9	4.6	0.976
-10	5239	98	3.56	16.6	0.989

Table 5.1: Elastic moduli fit to the data of Tinawi and Gagnon (1984)

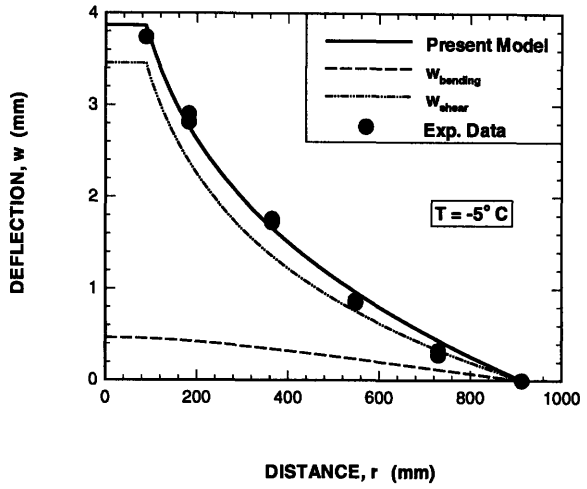

(a)

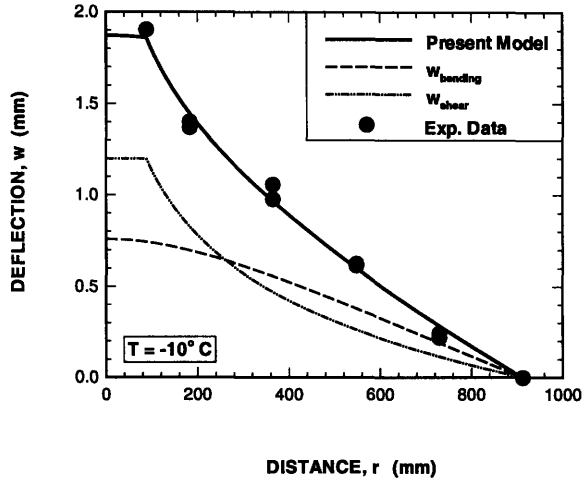

(b)

Figure 5-3: Fit of thin ice plate deflection data of Tinawi and Gagnon (1984) at: (a) $-5°C$; (b) $-10°C$. The bending and shear contributions are shown.

The contribution of shear deformation to the overall deformation falls from 90 to 65% [1] as the

[1]The point under the ring load is considered.

temperature goes from $-5°C$ to $-10°C$. Thus even though E remains approximately constant the contribution of bending deformation becomes more important with falling temperature.

The Young's modulus was measured by Gold and Traetteberg (1974) as a function of time by conducting uniaxial compression tests, albeit for fresh water, columnar grained ice. At 100 seconds, and at $-10°C$, E is of the order of $6GPa$. Thus the calculated E from transverse loading data, Table 5.1 is in an acceptable range.

Figure 5-3 shows that the bending and shear deformation curves fit the data well and the coefficients of correlation (Table 5.1) are high. For comparison, the data is fit by assuming only

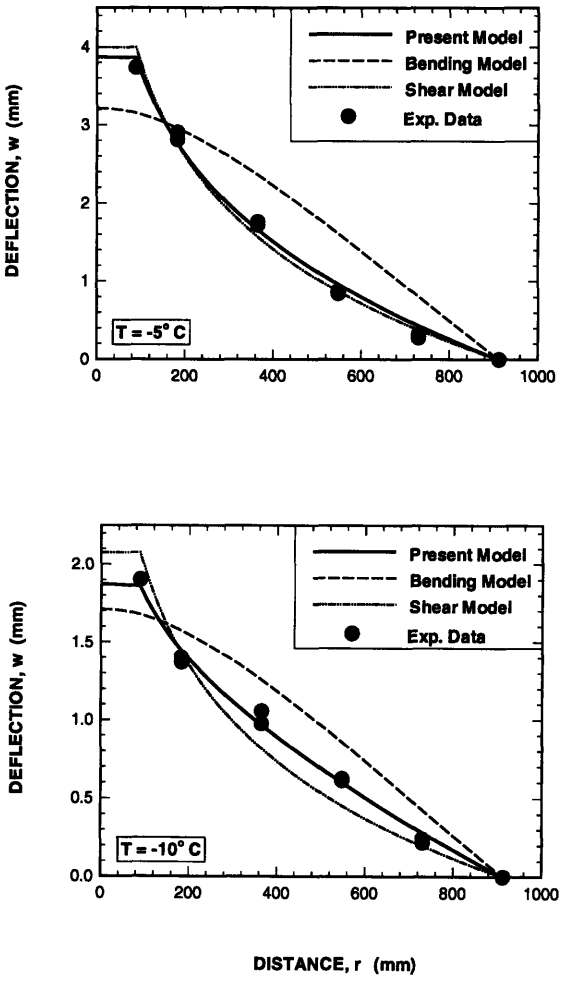

Figure 5-4: Fit of deflection data of Tinawi and Gagnon (1984) by (i) bending and shear model; (ii) bending only model; and (iii) shear only model, at: (a) $-5°C$; (b) $-10°C$.

bending and only shear deformation, see Fig. 5-4. The resulting moduli are: at $T = -5°C$, $E = 0.563GPa$, $G = 4MPa$; at $T = -10°C$, $E = 1.58GPa$, $G = 9.6MPa$. Notice now both E and G are temperature dependent. The Young's moduli are low. Further, the bending only

deformation curves do not resemble the shape of the data at all.

Floating Infinite Ice Plate

The second case that is considered is that of a thin floating model urea ice sheet. Assuming only bending deformation, Kerr and Haynes (1988) calculated the average $E = 43.7\ MPa$ for a model urea ice sheet they tested earlier. As already mentioned, Timco (1981) raises two concerns. First, this reference argues that the lower limit on E of urea ice should be $1.3\ GPa$; the E obtained using the bending deformation Eq. (5.4) is more than an order of magnitude smaller than this lower bound. Second, deflection data (i) well away from the loading, and (ii) at the loading point result in two different moduli E. These two issues might be resolved if the deformation is assumed to be caused by bending and shear, Eq. (5.16), and not just bending. This hypothesis is studied using the limited data of Sodhi *et al.* (1982).

Sodhi *et al.* (1982) performed two experiments on a floating, $46mm$ thick, model ice sheet, at an air temperature of $-12°C$. The deflection at only three points away from the point load was monitored as the load increased. The deflections at $P = 40N$ are considered. These deflections are used when calculating the average error defined as:

$$\bar{e} = \sum_{i=1}^{N} \frac{|w(r_i) - w_i^M(r_i)|}{N} \tag{5.20}$$

where $w(r_i)$ is the analytic deflection due to bending and shear, calculated at r_i from Eq. (5.16).

The average error is plotted in Fig. 5-5 for various (E, G) combinations. Although the data fit is nearly perfect (coefficient of correlation ≈ 1.0) corresponding to the moduli which minimize $\bar{e}$, bear in mind that the fit is based only on three points. If more data points are included, the minimum $\bar{e}$ might be associated with a different set of moduli. Also, the load– deflection curves are not perfectly linear, perhaps due to some relaxation. Further, the small initial seating–in deflection was not processed out of the data. Thus the moduli corresponding to the minimum $\bar{e}$ are not reliable. Instead of defining a single moduli pair based on the available data, the true moduli should be found in a region of $\bar{e}$; say $\bar{e} < 0.15mm$. Note that w^M are of the order of a millimeter. The shaded region in Fig. 5-5 corresponds to $\bar{e} < 0.15mm$. This region reveals an important result. There are two branches to fit the data: (1) low G and high E corresponding to predominantly shear deformation, and (2) high G and low E corresponding to bending deformation. Previously only the latter branch was used in estimating the Young's modulus of model ice sheets. It must be emphasized that more data are required, especially close to the loading point, in order to obtain more reliable moduli based on the minimum error. Since this data is not available, the data from Sodhi *et al.* (1982) second experiment must be used.

In their second experiment, Sodhi *et al.* (1982) measured the evolution of deflection at the point of loading. This data cannot be simply combined with the the data from their first experiment since the loading was different. The elastic moduli that fit the data from the second experiment are obtained with the aid of the finite element method. The thin ice sheet is idealized as having

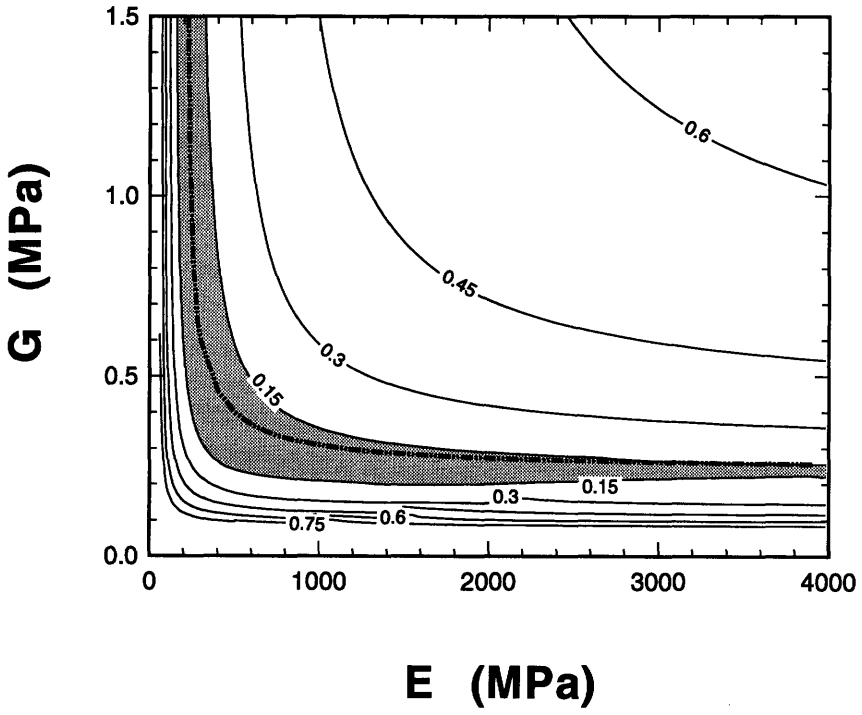

Figure 5-5: Contour plot of the average error, $\bar{e}$, for various combinations of E, G, for the data of Sodhi *et al.* (1982).

one grain through the thickness. Each grain is discretized into four eight node isoparametric, axisymmetric elements. Grain boundary deformation along the boundary is allowed; no grain boundary deformation normal to the boundary is permitted. The grain boundary shear stiffness is modeled by linear springs (see the previous chapter for details). A schematic representation of two adjacent grains is shown in Fig. 5-6. A constant shear stiffness through the ice thickness is assumed. The springs on the grain boundary are all assumed to have a constant stiffness, s_k.

The grain size is taken as $d = 5mm$. The plate is loaded by a ring load at a distance $r = 45mm$ by a total load $P = 22.24N$. The buoyancy is modeled by an elastic foundation of stiffness $\kappa = 9800N/m^3$. In the finite element analyses, the plate has a finite radius of $3m$, or 600 grains. The radius was proved to be sufficiently large by considering a plate of 500 grains. The deflection under the ring load varied by $< 0.4\%$ between the two cases.

The elastic moduli, E, G of the ice sheet are chosen so that the displacement under the load predicted by the finite element method are approximately equal to the deflection reported in Sodhi *et al.* (1982). In order to match the results from the first experiment as well, E, G have to be chosen from the shaded region in Fig. 5-5. The search on E, G is further limited to the local minima in the average error, represented by the chain line in Fig. 5-5.

The grains are assumed isotropic with Young's modulus E and Poisson ratio $\nu = 0.33$. The

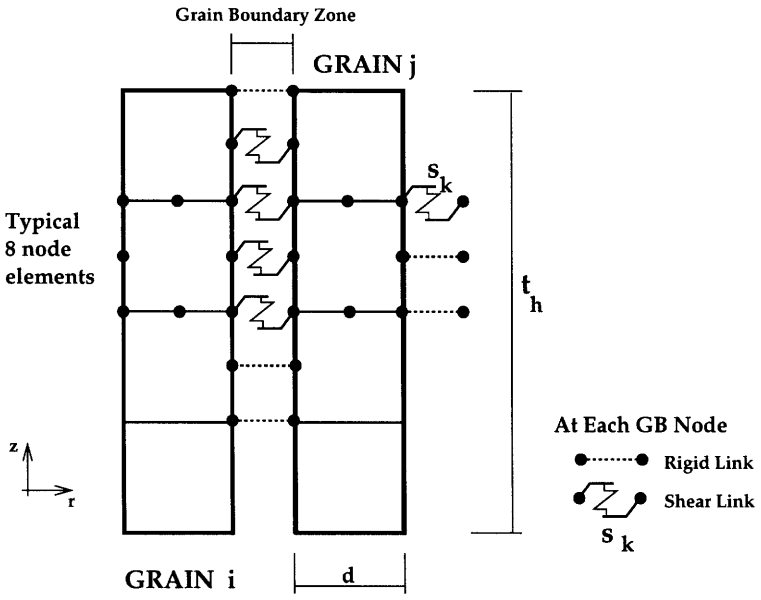

Figure 5-6: Two adjacent grains in a thin ice plate, showing finite element discretization and grain boundary zone treatment.

bending behavior is controlled by the grain's E. The transverse shear modulus, G, is controlled by the stiffness of the grain boundaries. The relationship between G, which is a smeared continuum property used in the analytical expressions, and the discrete shear spring stiffness, s_k, for an axisymmetric problem can be shown to be:

$$s_k = \frac{2\pi r t_h}{nd} G \tag{5.21}$$

where at a given distance r there are n springs (and hence n nodes) on the grain boundary.

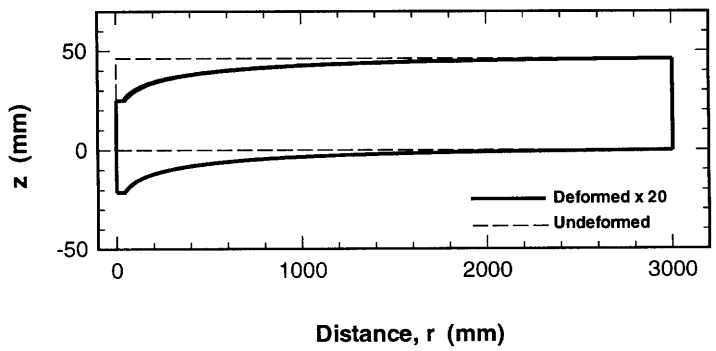

Fig. 5-7(a)

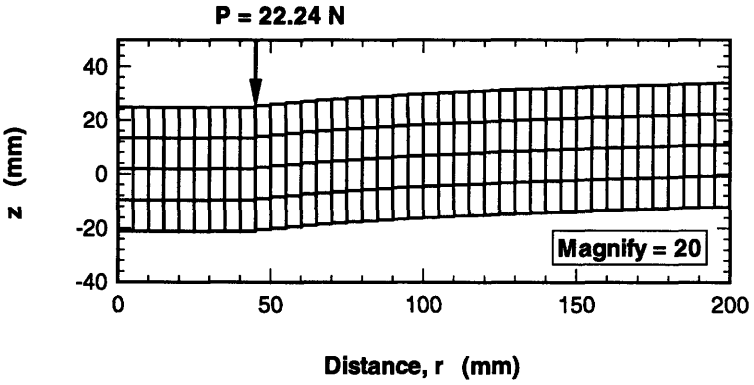

Fig. 5-7(b)

Figure 5-7: (a) Outline of deflected shape of floating plate subject to ring load; (b) Detail of deformed shape showing discretization. Deflected shape is magnified 20 times.

This method results in: $E = 3.2GPa$ and $G = 0.26MPa$. The magnified deflected shape of the ice plate is shown in Fig. 5-7. The deflection under the ring load is: $1.06mm$ as calculated, and $1.1mm$ as measured by Sodhi *et al.* (1982). The calculated moduli correspond to the shear branch of the solution. Note that the Young's modulus is well above the lower limit postulated by Timco (1981).

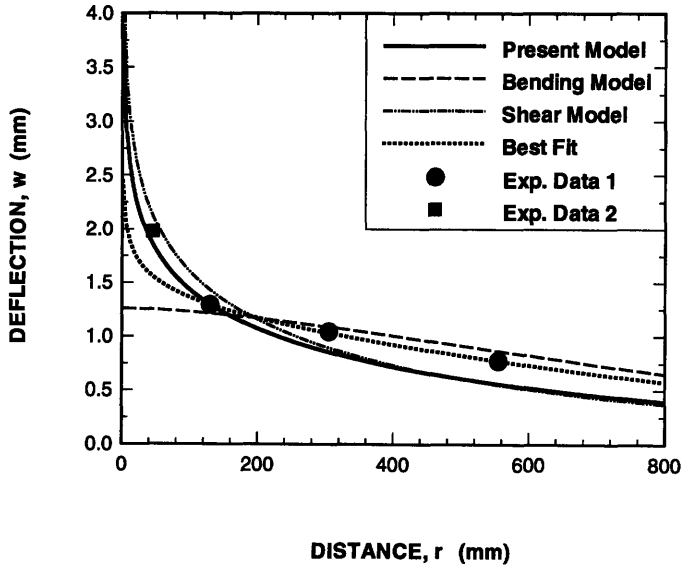

Figure 5-8: Deflected shapes of floating ice plates. Both data sets of Sodhi *et al.* (1982) are also plotted.

Both data sets of Sodhi *et al.* (1982) are plotted in Fig. 5-8 together with analytical best fit

curves. The data from the second experiment is scaled to $P = 40N$ so that the deflections are comparable with the first set. The four curves are based on: (a) bending deformation only; (b) shear deformation only; (c) bending and shear deformation (best fit); and (d) bending and shear deformation with $E = 3.2GPa$ and $G = 0.26MPa$ (present model). The first three cases are fit to the first experimental set ignoring deflection at the loading point.[2] Figure 5-8 shows that all the curves fit the outlying data points relatively well. However, the shear deformation only curve, and curve labeled "present model" fit the data at the loading point as well. The bending only curve confirms the observations in Timco (1981): the required $E = 177\ MPa$, which is significantly less than the lower limit; a lower E is required if the bending only curve is fit to the deflection under the load.

5.4.2 Thick Plates

The elastic moduli of two thick floating ice plates are calculated assuming the plate deforms in bending and in shear. The deflection of the first plate was measured by Bernshteyn (1929). The experimental data gathered by Shmatkov (1968) is considered for the second plate.

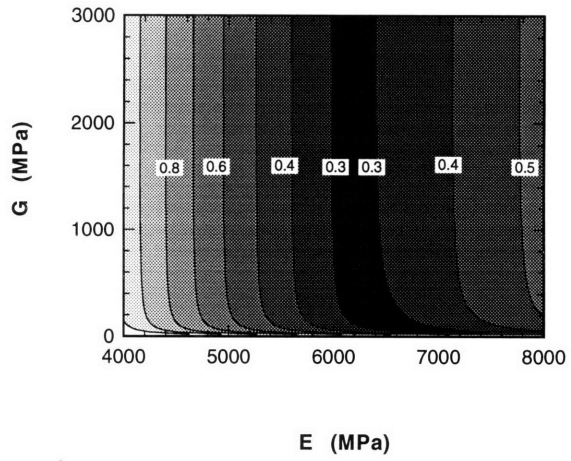

Figure 5-9: Contour plot of average error, $\bar{e}$, corresponding to data of Bernshteyn (1929), showing the bending solution branch.

Bernshteyn (1929) experimented on a fresh water ice plate $0.94m$ thick and loaded by $P = 0.235MN$ for a short duration; the air temperature was between $-15°C$ and $-7°C$. The map of

[2]Note, both data sets cannot be used simultaneously when performing the fit since the experiments had different loading conditions.

the average error, $\bar{e}$, calculated from Eq. (5.20), the analytical Eq. (5.16) and Bernshteyn's data, is plotted in Fig. 5-9. The minimum average error is, $\bar{e} = 0.26mm$ corresponding to moduli $E = 6.61GPa$ and $G = 90MPa$. Considering average errors which are 15% bigger than the minimum average error, produces a band of possible E, G pairs. The band (*i.e.* $\bar{e} < 0.3$) is shown in Fig. 5-9. This band stretches over a wide range of G values, but it is narrow in the E direction. The band in E is approximately 7% of the average E value. Thus only the bending branch of the solution exists. Figure 5-9 indicates that while an accurate value for the in plane Young's modulus can be obtained from the data, an estimate of the transverse shear modulus is impossible.

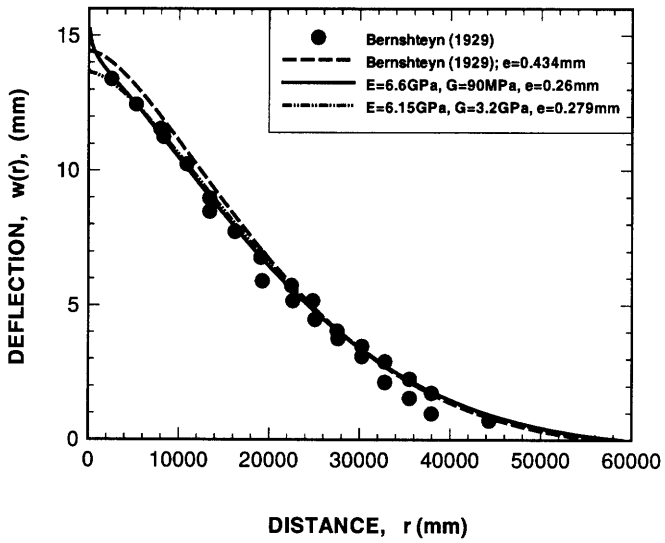

Figure 5-10: Deflected shapes and data points of a thick ice place tested by Bernshteyn (1929).

The above conclusion is emphasized in Fig. 5-10 which plots the plate's deflected shape together with the data of Bernshteyn (1929). Three sets of moduli are considered: (1) $E = 5.47GPa$ fitted by Bernshteyn assuming only bending behavior, the resulting $\bar{e} = 0.43mm$; (2) $E = 6.61GPa$ $G = 90MPa$ which corresponds to minimum error of $\bar{e} = 0.26mm$; and (2) $E = 6.15GPa$ and $G = 3.2GPa$, the corresponding $\bar{e} = 0.28mm$. Note that all three curves are almost identical, differing only close to the point of loading. The latter two curves are particularly close, and differing only slightly in the errors they produce, even though their shear moduli vary by more than an order of magnitude.

A more accurate estimate of G can be obtained by measuring the deflections close to the loading. Now however, care has to be taken to model the loading more accurately, *i.e.* the finite width of the loading has to be accounted for.

Shmatkov (1968) conducted tests on a floating fresh water ice sheet, $0.5m$ thick, and close to the

melting temperature. This reference reports that the plate deformed predominantly in shear with a transverse shear modulus of $G = 1.47MPa$. In obtaining this value, Shmatkov assumed a shear plate and used Eq. (5.10). The corresponding average error is $\bar{e} = 1.1mm$. This error is larger then in the previous example since there is more scatter in the data. Assuming both bending and shear deformation, Eq. (5.16), the resulting average error map is plotted in Fig. 5-11. Note that only realistic value for the Young's modulus are considered, *i.e.* $E < 10GPa$. Figure 5-11 shows that the plate behavior corresponds to the shear branch of the solution. A wide band of possible E, G combinations forms only in the E direction. The minimum average error corresponding to realistic moduli is $\bar{e} = 1.30mm$. This minimum corresponds to $E = 10GPa$ and $G = 2.11MPa$.

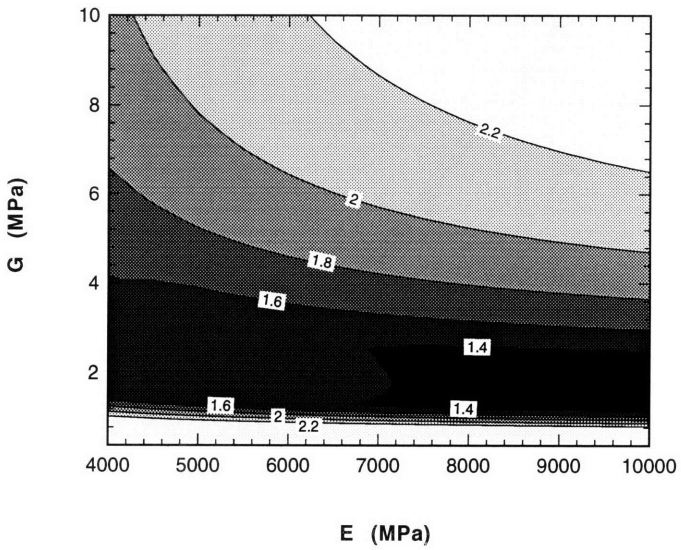

Figure 5-11: Contour plot of average error, $\bar{e}$, corresponding to data of Shmatkov (1968), showing the shear solution branch.

The fit of Eq. (5.16) together with data and fit of Shmatkov (1968) are plotted in Fig. 5-12. To demonstrate that the solution is dominated by shear, *i.e.* relatively independent of E, two moduli combinations are considered: (1) $E = 10GPa$ $G = 2.11MPa$ resulting in $\bar{e} = 1.30mm$; and (2) $E = 7GPa$ $G = 1.31MPa$ resulting in $\bar{e} = 1.39mm$. Note that the errors are approximately the same. While the first curve emphasizes the data further away from the loading, the second curve fits the deflections closer to the loading better. The curve of Shmatkov (1968) lies in between these two curves. All three curves fit the data acceptably well.

5.5 Conclusion

This chapter examines the effect of including both shear and bending deformations in the behavior of elastic ice plates. In most cases a floating ice sheet subject to a point load is considered.

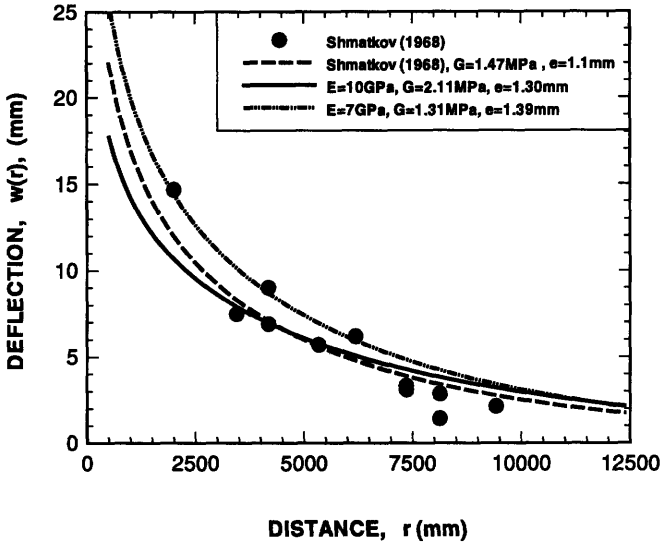

Figure 5-12: Fit deflected shapes and data points of a thick ice place tested by Shmatkov (1968).

The in- plane Young's modulus, E and the transverse shear modulus, G, are obtained by fitting an analytical expression for the deflection to experimental data. The data is fit using least squares. Both plates containing a few grains through the thickness, or thin plates, and thick plates are examined.

Results show that both thin and thick plates can exhibit shear behavior. The observation made by Kerr (1976) that ice plates near the melting temperature deform in shear, while plates at lower temperatures deform in bending, is confirmed and extended. Thin ice sheets can also deform in shear, even at low temperatures, *e.g.* Sodhi *et al.* (1982) tested a $46mm$ thick model ice sheet at $-12°C$. This result is in agreement with the theoretical observation of the previous chapter: thin ice sheets can show appreciably more shear deformation than thick ice sheets at the same temperature. This behavior of thin model ice sheets in bending and *in shear* provides an answer to two concerns raised by Timco (1981). Namely: (i) why the in- plane Young's modulus of thin model ice sheets is so low? and (ii) why a higher Young's modulus is obtained when fitting deflection data points further away from the loading? To emphasize the point: previously, the Young's modulus was calculated assuming only bending behavior, while the model ice plates might deform predominantly in shear.

The work presented here shows the importance of accounting for both the bending and shear deformations. The contributions of each type of deformation influences the overall deflection, or in the inverse problem the calculated elastic moduli. Further, the amount of energy stored in bending and in shear is important when conducting fracture analyses. To the authors knowledge, previous fracture analyses of ice plates have ignored shear strain energy.

Further work is required in modeling the loading more accurately. Here point loading was assumed. More comprehensive data on deflections close to, and further away from the loading are

urgently needed. This will allow for more accurate predictions of the moduli, *i.e.* the range of possible E, G pairs will decrease. An investigation into discerning time dependent behavior from elastic response, especially close to the melting point, is also required.

REFERENCES

[1] Bernshteyn, S., (1929), Railroad Ice Crossing, [In Russian], *Trudy Nauchnovo- Technicheskogo Komiteta Narodnogo Komissariata Putei Soobshcheniya*, Vol. 84, pp. 36- 82.

[2] Frederick, D., (1956), On Some Problems in Bending of Thick Circular Plates on an Elastic Foundation, *Journal of Applied Mechanics*, Vol. 78, pp. 195- 200.

[3] Gold, L.W. and Traetteberg, A. , (1974), Young's Modulus of Ice and Ice Engineering Problems, *Proc., 2nd Symp. on Application of Solid Mechanics*, Dep. Mech. Eng., McMaster Univ., Hamilton, pp. 1- 15.

[4] Kerr, A.D., (1976), The Bearing Capacity of Floating Ice Plates Subjected to Static or Quasi-Static Loads, *Journal of Glaciology*, Vol. 17, p. 229- 268.

[5] Kerr, A.D., and Palmer, W.T., (1972), The Deformation and Stresses in Floating Ice Plates, *Acta Mechanica*, Vol. 15, pp. 143- 149.

[6] Kerr, A.D. and Haynes, F.D., (1988), On The Determination of The Average Young's Modulus For a Floating Ice Cover, *Cold Regions Science and Technology*, Vol. 15, p. 39- 43.

[7] Naghdi, P.M., and Rowley, J.C., (1953), On The Bending of Axially Symmetric Plates on Elastic Foundations, *Proceedings of the First Midwestern Conference on Solid Mechanics*, University of Illinois, pp. 119- 123.

[8] Selvadurai, A.P.S., (1984), Flexure of a Non- Homogeneous Floating Ice Plate, *IAHR Symposium*, Hamburg, Vol. I, pp. 123-136.

[9] Shmatkov, V.A., (1968), The Deformation Characteristics of the Ice Cover of Lake Baykal During the Spring Period, [In Russian], *Trudy Gosudartstvennogo Gidrologicheskogo Instituta*, Vol. 159, pp. 29- 33.

[10] Sodhi, D.S., Kato, K., Haynes, F.D., and Hirayama, K., (1982), Determining The Characteristic Length of Model Ice Sheet, *Cold Regions Science and Technology*, Vol. 6, p. 99- 104.

[11] Timco, G.W., (1981), On the Test Methods for Model Ice, *Cold Regions Science and Technology*, Vol. 4, pp. 269- 274.

[12] Tinawi, R., and Gagnon, L., (1984), Behavior of Sea Ice Plates Under Long Term Loading, *IAHR Symposium*, Hamburg, Vol. I, pp. 103-112.

[13] Timoshenko, S., and Woinowsky- Krieger, S., (1959), *Theory of Plates and Shells*, 2nd Edition, McGraw-Hill, New York.

[14] Wyman, M., (1950), Deflection of an Infinite Plate, *Canadian Journal of Research*, Sec. A, Vol 28, p. 293- 302.

[15] Zubov, N.N., (1945), *Arctic Ice*, [In Russian], Moscow, Izdael'stvo Glavsevmorputi.

Chapter 6

CONCLUSION

6.1 Salient Results

This thesis has investigated several aspects of polycrystalline ice behavior. In particular the following questions have been addressed: (1) the cause of microcrack nucleation and growth at high compressive strain- rates; (2) the number of grains required to homogenize polycrystalline ice; (3) thickness effect on the elastic transverse shear modulus of ice plates; and (4) the effect of including both shear and bending deformation on the deflection of floating thin and thick ice plates. The salient results from each of these topics are summarized below.

The Cause of Microcracking

The mechanism of grain elastic anisotropy which was thought to be the cause of microcrack precursors in compression has been shown to be too weak in polycrystalline ice. The stresses required for microcrack nucleation and growth are unrealisticly high and the longest possible microcracks are too short. If grain boundary sliding is allowed, much more realistic stresses and crack lengths are obtained. When the grain boundary sliding mechanism operates, a defect originating at the triple point grows stably, reaches a critical length and then propagates unstably to the neighboring triple point. The stress causing microcrack growth is found to be inversely proportional to the square root of the grain size. As observed experimentally, planar confinement increases the microcracking stress until for confinement ratios greater than 0.2, facet length microcracks are impossible. Facet length microcracks can only form in a 25° range to either side of the loading axis. These results from simulations have been observed experimentally.

Number of Grains in Representative Area Element

At least 230 grains are required to homogenize the elastic properties of polycrystalline ice. Samples containing fewer grains show more scatter in the homogenized elastic properties and the results

are contaminated by edge effects. The grain's elastic anisotropy is most important when no grain boundary sliding is allowed; grain shape is more significant when grain boundary sliding is permitted. The stress components at the grain centers approximately follow the Gaussian distribution. The average computed homogenized Young's modulus and Poisson ratio at $-16°C$ are: 9.58 GPa and 0.33- with no grain boundary sliding; 7.83 GPa and 0.45- with free grain boundary sliding. These results place a lower bound on the size of (1) the experimental samples; (2) the numerical "computation box" in micromechanical studies; and (3) the finite element size in macroscopic, homogenized continuum models.

Thickness Effect on Ice Plate Shear Modulus

Ice plates contain only a few grains through their thickness. The homogenized shear modulus can increase five times as the plate thickness increases from 0.05 to 1.2 m. When the grain boundary shear stiffness is low, the increase is linear with thickness. At higher stiffnesses the increase in shear modulus versus plate thickness is non linear. When there is no grain boundary deformation the homogenized shear modulus is constant, *i.e.* independent of plate thickness. The thickness effect is due to grain boundary deformation, and grain coarsening with plate depth. Temperature effects, which are accounted for by changing the grain boundary shear stiffness, significantly influence the homogenized transverse shear modulus. A reduced shear modulus implies that shear deformation is important in ice plate deformation. Shear deformation is expected to be more pronounced at higher temperatures and thinner plates.

Shear and Bending Deformation in Ice Plates

The results of modeling both the shear and bending deformation show that thin ice plates and plates close to their melting temperature behave predominantly in shear; thick, cold plates deform in bending. The bending and shear deformation equations reduce to the plate bending limit and the shear plate limit; previously these two limiting cases were considered separately. The Young's modulus of thin model ice sheets, estimated using the bending and shear theory fit to transverse data, is more than an order of magnitude greater than calculated previously. The new Young's moduli are more realistic.

6.2 Future Work

Future research based on the work presented in this thesis can be split into the following three scales: (1) micromechanical modeling– multiple grain scale; (2) 1- 100 meter scale; and (3) 10 kilometer of floe cluster scale. The applicability of this thesis, the extensions required and the type of problems to be considered on these three scales are outlined briefly.

Multiple Grain Scale

The grains have been assumed to behave elasticly in this thesis. This assumption can be relaxed by modeling the grains as viscoplastic. Parameters such as basal plane orientation and grain size and shape should be considered. The aim is to capture the behavior of polycrystalline aggregates based on an assembly of single grains. The difficulty here is that polycrystalline ice exhibits softening behavior in the ductile to brittle transition regime. As mentioned in the Introduction, this regime is of interest since maximum stresses occur here. The behavior is complicated further by intense microcracking activity in the region of maximum stresses.

Work on estimating the evolution of the elastic compliance of polycrystalline ice with microcracking has been done by Wu and Shyam Sunder (1992) and Elvin and Shyam Sunder (1994a, b). The results in these references strongly suggest that under compressive loading, microcracking alone cannot cause softening in polycrystalline ice. The question arises now: What causes softening in polycrystalline ice? The hypothesis that microcracks enhance creep to such an extent that the polycrystal softens can be investigated quantitatively with the unit cell model presented in Chapter 2. Work by the present author in collaboration with D. Choi and J. Connor on this question is currently on the way.

By including a realistic fracture criterion, and tracking the nucleation and coalescence of individual microcracks, failure of polycrystalline ice specimens can be simulated. The numerical polycrystalline samples presented in Chapter 3 would be used. This problem is not easy, since an easy fracture criterion, and one that provides acceptable results when only a course finite element mesh is used, is currently not available. The problem is further complicated by the microcracks kinking, coalescing and intersecting. As a first approximation, a strength criterion might be useful. These simulations can be used to study the effect of confining ratios on axial splitting, shear faulting and complete granulation. Size effects, and scaling laws, at least on the multiple grain scale, can be investigated by considering numerical specimens of various sizes.

The philosophy of an even more ambitious plan, one that couples the multiple grain scale with the engineering scale (1- 100 meters) has been discussed in Connor *et al.* (1995). This plan models the process zone ahead of an advancing macrocrack on the engineering scale, using a micromechanical model for the ice grain structure. The micromechanical "computational box" is shifted ahead of the advancing macrocrack tip. Such simulations, if ever conducted, will for the first time be able to model several failure modes that occur on the macro scale. This model will be truly micromechanically based.

1- 100 Meter Scale

Most problems of engineering interest occur at this scale. As shown in Chapter 4, due to grain boundary deformation, the transverse shear modulus of the ice plate can be significantly reduced. Thus the behavior of the ice plate can be influenced and even dominated by shear deformation. Chapter 5 has already shown one application in calculating more realistic Young's moduli for ice plates. The significance of shear deformation, however, goes much further.

Future analyses of fracture of ice plates loaded transversely, should consider strain energy due to transverse shear deformation. Examples of engineering problems of this nature are: ice plate penetration, fracture of ice plates against sloping structures, "flexural" failure of ice plates. In the past, only bending plates and hence only bending energies were considered. The results should be re-examined accounting for shear deformation. For example, Bazant and Li (1994, 1995) considered the vertical penetration fracture of floating ice plates. These references made an implicit assumption that the ice plates acted only in bending. Scaling laws with thickness were derived. The question now arises: are these scaling laws valid if a the scaling of the shear modulus shown in this thesis is taken into account?

During ice plate indentation, in plane cracks– spalling and cleavage cracks, form. These have been analyzed by Wierzbicki (1985) assuming bending deformation only. Once again, shear deformation energy has to be considered in these types of analyses.

Buckling analyses of floating ice plates (*e.g.* Wierzbicki (1985)) also have to consider shear deformation instead of just bending.

Floe Cluster Scale

The model developed in Chapter 3 for a polycrystalline aggregate can be extended to the floe cluster scale (10 kilometer scale). Instead of viewing each Voronoi polygon as a grain, it is viewed as a floe. Of course, the homogenized material properties of the floe have to be input. Also the grain boundary deformation has to be modeled. Special attention has to be given to the boundary conditions. Some work along these lines has already been done by Hopkins (1993) using dynamic particle simulations. The new model can be used to study stresses in the ice floes, formation of ice ridges and large areas of open water. Some researchers believe that such open water areas in the arctic effect global climatic conditions. In light of the above, it is suggested that careful consideration be given to possible large deformations in the floes, and the modeling of local failure within the floes.

REFERENCES

[1] Bazant, Z.P., (1992), Large-scale Thermal Bending Fracture of Sea Ice Plates, *Journal of Geophysical Research*, Vol. 97(C11), pp. 17739- 17751

[2] Bazant, Z.P., and Li, Y.N., (1994), Penetration Fracture of Sea Ice Plate: Simplified Analysis and Size Effect, *Journal of Engineering Mechanics*, Vol. 120, pp. 1304- 1321.

[3] Bazant, Z.P., and Li, Y.N., (1995), Penetration Fracture of Sea Ice Plate, *International Journal of Solids and Structures*, Vol. 32, pp. 303- 313.

[4] Connor, J.J., Shyam Sunder, S., Elvin, A.A., Choi, D., Kim, J., (1995), Physically Based Constitutive Modeling of Ice, *Proceedings of the Sea Ice Mechanics and Arctic Modeling Workshop*, April 25- 28 1995, Anchorage, Alaska, Organized by Northwest Research Associates, Inc., Bellevue, WA.

[5] Elvin, A.A., Shyam Sunder, S., (1994a), Compliance of Polycrystalline Ice With Evolving Microcrack Population, *Proceedings of the Europe-US Workshop on Fracture of Quasibrittle Materials: Experiments, Theory and Computation*, Prague, September 21- 23, 1994, p.473-478.

[6] Elvin, A.A., Shyam Sunder, S. (1994b), Micromechanical Damage Model For Polycrystalline Ice– Elastic Anisotropy Mechanism, *Unpublished*

[7] Hopkins, M., (1993), A Mesoscale Simulation of the Arctic Ice Pack, *Ice Mechanics, '93*, ed. J.Dempsey, Z.Bazant, Y.Rajapakse, and S.Sunder, pp. 85-96.

[8] Wu, M.S., and Shyam Sunder, S., (1992), Elastic Anisotropy and Micro- damage Processes in Polycrystalline Ice. Part II: Numerical Simulations, *International Journal of Fracture*, Vol. 55, pp. 375- 396.

[9] Wierzbicki, T., (1985), Spalling and Buckling of Ice Sheets, *Proceedings of the ASCE Arctic '85 Conference*, ed. F.Bennet, and J.Machemehl, pp. 953- 961.